Field-effect polymer gating of low-dimensionality carbon-based materials

Original
Field-effect polymer gating of low-dimensionality carbon-based materials / Sharda, Kanudha. - (2015).

Publisher:
Politecnico di Torino

Published
DOI:10.6092/polito/porto/2590157

POLITECNICO DI TORINO

SCUOLA DI DOTTORATO
Dottorato in Fisica – XXVII ciclo

Tesi di Dottorato

Field-effect polymer gating of low-dimensionality carbon-based materials

Kanudha Sharda

Tutore
Prof. Renato S. Gonnelli

Coordinatore del corso di dottorato
Prof. Arianna Montorsi

Anno accademico 2012-2014

Summary

With close to ten publications a day and an unprecedented financial support from the European Commission as well as large-scale initiative in the Americas and Asia, graphene is one of the hottest topics in condensed matter physics. The interest for low dimensional Carbon-based materials, in particular graphene, was revitalized in the mid 2000's by the measurement of its exceptional electronic properties and the realization that this single sheet of graphite is attractive for electronic applications. Many other nano-structures are derived from graphene with different order of dimensionality like graphite, carbon nanotubes [1, 2], fullerenes [3, 4] (3D, 1D, 0D respectively) exhibiting exceptional electronic properties and equally large variety of physical properties. This opens up large scope of studies and applications in (opto)electronics, spintronics, sensors, catalysts, in chemistry and biology and as structural material. Studies in graphene also raised fundamental research related to other 2D materials like topological insulators, and their generalization to different classes of 2D exfoliable compounds.

In this rapidly developing field, ten years after the pioneer publications in graphene, new concepts have emerged, on both experimental and theoretical sides. It is this motivation that led me to present a comprehensive and coherent scientific study in the field of graphene and few other carbon based compounds.

However, from its invention to commercialization there is a long way to go. Also, before graphene could overtake the conventional silicon technology, fundamental studies of its properties are required. Indeed after the tenth anniversary of

its discovery it is evident that graphene has been one of the most studied materials of the past decade. It has a short history but has attracted huge scientific interest and as a result there has been abundant advances in technological applications. Its scope is gradually dispersing to advanced technological fields such as photonics, high frequency electronics, sensitive gas sensors, transparent electrodes for flat panel displays, supercapacitors. Since it possess exceptional electrical, mechanical and thermal properties, exciting theoretical predictions such as possible occurrence of superconductivity are expected to form the next milestone in its development.

For a rapid technological growth it is of utmost importance to realize graphene devices that are able to tune their transport properties by means of the application of an electric field. In the recent years an extensive research study has been initiated to exploit the fundamental level in a wide variety of Carbon materials. This Ph.D. thesis focuses on the modification of the transport properties of low-dimensional carbon-based materials by tuning their surface charge carrier density (up to values of induced charge exceeding 6×10^{14} carriers cm^{-2}) via electrochemical gating with an innovative polymer electrolyte solution (PES). The study is made mainly on few layer graphene (FLG) systems produced by micro-mechanical exfoliation and on single layer graphene (SLG) synthesized by chemical vapor deposition (CVD) growth method. The technique has also been applied to highly oriented pyrolytic graphite (HOPG) to study how the properties are controlled by simply changing the way of source current injection. Attempts to modulate the superconducting critical temperature of the Graphite Intercalated Compounds (GICs) like CaC_6 are also reported.

Chapter 1 briefly describes the basic properties of the different subjects under study. It includes the theoretical background of the electronic and transport properties of ideal SLG. An overview of the methods used to produce graphene, for example, the mechanical exfoliation and CVD along with the role of substrate and the defects associated is reported. Apart from these discussions the band structures of FLG are introduced. The main aim of this chapter is to explain how graphene and its derivatives distinguishes from conventional materials.

In Chapter 2, the basic principle of the formation of the dynamic electric double layer (EDL) via electrochemical gating is described. A novel PES is used for this purpose which is able to produce huge electric fields at the interface with the sample. It becomes possible to induce high surface charge densities up to more than 10^{14} charges cm^{-2}. An overview of the state of the art of this specialized technique applied successfully to a variety of materials is reported. In particular results on metals and low dimensional carbon based materials are summarized. The main results of the mentioned previous work shows that electrochemical gating is a much more efficient way as compared to the standard dielectric gating in order to modify properties of materials in an elegant way.

In the next Chapters, we have described the details of our implementation of the EDL gating technique. Full description of the device fabrication and its particular design is given here including the production and deposition of the polymer. In these devices we were able to perform transport measurements by the standard four-wire technique down to 2.7 K. However, even at the highest induced charge density we were not able to observe any desired phase transition. Instead, a continuous enhancement (or progressive induction) of the metallic behavior and a low-temperature logarithmic upturn of the resistance, strongly dependent on the induced charge has been observed. Since Kondo-effect and electron-electron interaction (EEI) contributions can be ruled out on the basis of Raman measurements and of the magnetic-field dependence of the resistance, this peculiar low-temperature behavior has been analyzed and explained in terms of weak localization (WL) due to localized defects at the sample surface. However, the induced surface charge was determined by a suitable modification of a classic method of electrochemistry called the double-step chronocoulometry. Since the application of this technique is quite new for this purpose, we made a validation check by comparing it with standard Hall effect measurements. This powerful technique is described in Chapter 3 while the results are included in Chapter 4 & 5. Other measurements were done in order to study the effect of the electrochemical gating technique, that track the changes in properties of a material, for example the popular Dirac curves and Raman measurements. Then few warnings, limitations and drawbacks are listed because electrochemical gating technique is very complex and one needs to be careful about certain aspects before applying its use on different materials in order to obtain precise results.

In Chapter 4 & 5, results of recently performed electrochemical gating experiments in FLG devices (mainly three-, four-, and five-layers) and SLG at Politecnico di Torino, Istitito Nazionale di Ricerca Metrologica, INRIM (Torino, Italy) and the University of Cambridge (Cambridge, United Kingdom) are discussed. We have included our various results of electrochemical gating on highly oriented pyrolytic graphite (HOPG) here. In addition, an attempt to modulate the superconducting critical temperature of exfoliated CaC_6 has been performed, even if the extreme sensitivity to air of this material required a special technique for the preparation of field effect devices (FEDs) in a dry glove box.

Acknowledgements

There are many people whose contributions made my Ph.D. studies and stay at Torino a memorable and fruitful journey and I don't think I can thank them enough. I suppose I shall begin from the beginning...

First and foremost, I would like to express my deepest sense of appreciation to my supervisors Prof. Renato Gonnelli and Dr. Dario Daghero for their valuable advice, suggestions, guidance, patience and constructive critics throughout the completion of work of this thesis. Without their constant encouragement and support, this work would not have been accomplished. It is a privilege to thank Dr. Matteo Bruna and Prof. Andrea C. Ferrari at Cambridge Graphene Center and University of Cambridge, UK, for their generous support and collaboration in device fabrication.

I would like to thank Giovanni Alberto C. Ummarino, Mauro Tortello and Corrado de Bertoli for their constant support, discussions and collaborations. I also extend my gratitude to our Ph.D. school coordinator Prof. Arianna Montorsi, for her guidance and keeping me well informed throughout the tenure of three years. I want to thank Jijeesh R. Nair and Claudio Gerbaldi for the innovative polymer electrolyte whenever i needed it. I specially thank Sara Galasso (at Politecnico di Torino (PoliTO)), Emmanuelle Cappelluti and Valentina Brosco (at Istituto dei Sistemi Complessi (ISC) and Consiglio Nazionale delle Ricerche (CNR), Rome) for their support in ab-initio DFT and tight binding calculations. I acknowledge the helpful scientific discussions with Francesco Laviano and the support from Laura Gozzellino during the magnetic field measurements.

Words are not enough to acknowledge all my colleagues at PoliTO and INRIM who ensured that I was constantly engaged and entertained along the way. My sincerest thanks are extended to all my colleagues in our department: Alessandro Sola, Erik Piatti, Francesca Balestra, Riccardo Introzzi and Paola Pecchio for their collaboration as well as support in day-to-day life. I would like to also thank Prof. Felice Iazzi for his guidance and it has been a pleasure to work with him.

I would like to immensely thank Erasmus Mundus fellowship program, who extended financial support and PoliTO for providing me the resources for the three years tenure of my Ph.D. studies.

Finally, a very special note of appreciation to all my supportive and understanding family members, especially my parents and my brother who have always supported me strongly with all their love, encouragement and appreciation. A big thanks to my husband Shrikant who always motivate me to move ahead in life no matter what because we get better everyday as we move on!

Contents

II Results and Discussions 107

Part I

Literature and Experimental Techniques

Chapter 1

Introduction

Before we start the detailed analysis of the electric field effect on low dimensionality carbon based materials, it would be worthwhile to review the basic properties of these materials. In this chapter a theoretical background of the basic properties of single- and few-layer graphenes is presented. We mainly consider the electronic properties including calculation of band-structure, peculiar transport properties that lead to a particular kind of Quantum Hall Effect (QHE) observed at higher magnetic fields. The background of QHE discussed will include analysis of the classical Hall effect to the quantum treatment of the motion of an electron in a strong magnetic field. In the case of Klein tunneling, confinement and the integer QHE, the Dirac electrons behave in unusual ways. Also the variation of electronic properties of graphene stacks with stacking order and number of layers is addressed. The role of the substrate and the associated disorder is another important issue reported here. In addition, a brief introduction on how it can be exfoliated in a thermodynamically stable form from graphite and grown by CVD on metals like copper is given.

1.1 Basic properties of single layer graphene

Carbon is one of the most fundamental substance and is found abundantly in nature. It is the distinguishing property of catenation that occurs readily in carbon due to which it is able to form chemical bonds in many different directions. Indeed, its external orbitals can combine to *hybridize* allowing formation of chemical bonds in different directions.

A single carbon atom has six electrons and its ground state configuration is $1s^2\,2s^2\,2p_x^1\,2p_y^1$. Depending on the type of bond formed there are sp, sp^2 and sp^3 hybridizations. These forms that carbon can assume are called allotropes and are very well known from quite a long time such as graphite and diamond. Due to the small energy gap between the $2s$ and $2p$ orbitals, an electron can be promoted from the $2s$ to the empty $2p$ to give four unpaired electrons. At this level it is convenient for the electronic orbitals to mix together to form *hybrid* orbitals that allow many different types of chemical bonds. In sp^2 hybridization there is a mix between one s orbital and two p orbitals to form three hybrid orbitals that arrange themselves at 120° to each other in a plane, in order to be as far apart as possible. The remaining p orbital remains perpendicular to them.

The three sp^2 orbitals form strong σ bonds resulting in the formation of the hexagonal structure that characterizes graphene but these bonds do not contribute to conductivity. This arrangement of carbon atoms as a honeycomb lattice made out of hexagons is shown in Figure 1.1. These hexagons depict as if they are composed of benzene rings stripped out from their hydrogen atoms. The distance between the carbon atoms in a σ bond is 1.42 Å and it is this bond that is responsible for the robustness of the lattice structure while the p orbital which is perpendicular to the planar structure can bind covalently with neighboring carbon atoms leading to a π bond formation. This remaining orbital called the $2p_z$ orbital can form π bonds by delocalization of electrons over the entire molecule and are responsible for the peculiar electronic properties of graphene (as shown in Figure 1.2).

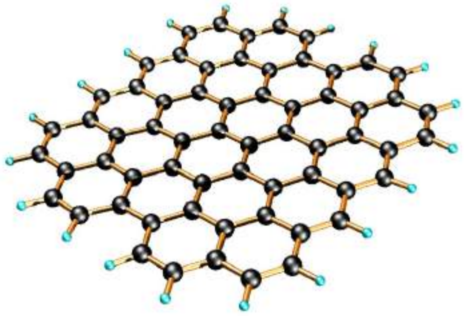

Figure 1.1. Honeycomb lattice structure of an idealized SLG. It can be seen as the starting base of all the allotropes of carbon.

Graphene presents an unprecedented and unusual combination of properties: thinnest material, high electronic mobility, optical transparency, mechanical resistance and flexibility, impermeable membrane, potential for functionalization and interface with biology. Because of its unusual structural and electronic flexibility graphene can be tailored chemically and/or structurally in many different ways.

Actually graphene layers are stacked one on top of the other and are linked to each other by weakly coupled van der Waals forces in graphite. Even with the benefit of hindsight, no body ever expected graphene to exist in the free state and hence no experimental tool existed to isolate the one atom thick flake among the

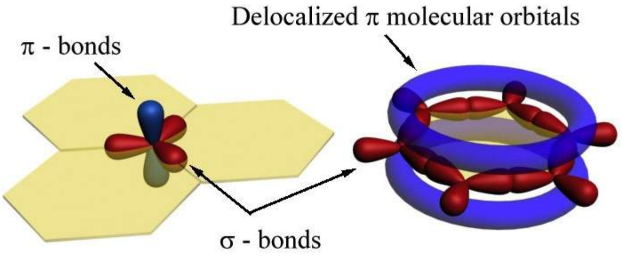

Figure 1.2. Left: sp^2 hybridized Carbon atoms form sigma bonds using three electrons and sharing one electron in a perpendicular $2p_z$ orbital, Right: delocalization of π electrons in the form of an aromatic ring is shown.

debris of graphite until its isolation. It was reported for the first time in 2004 [5] when it was eventually spotted due to the subtle optical effect it creates when placed over a SiO_2 substrate under an ordinary optical microscope.

Moreover, the electrons can be controlled by application of external electric and magnetic fields or by altering sample geometry and/or topology. In fact in this Ph.D. thesis it will be shown how the electrons can be controlled by generation of very high electric field at the interface and by applying external magnetic fields.

1.1.1 Electronic properties

Graphene is considered as the building block of all the sp^2 hybridized forms of carbon. In fact, most of the electronic properties were known long before its experimental discovery [6]. The existence of thermodynamically stable 2D form of graphene sheet was argued and it was believed that it should not exist in nature based on Mermin theorem. The theorem says that a pure 2D system is thermodynamically unstable at finite temperatures because the root mean square thermal fluctuations of atomic positions are comparable to the inter-atomic distances. Until this surprisingly appeared in the mid 2000's [5, 7] when Andre Geim and Kostya Novoselov at the University of Manchester were able to isolate it successfully. They isolated and characterized a single layer from graphite by micro-mechanical exfoliation which eventually led them to win a Nobel prize in Physics in 2010. However, the discovery of graphene does not violate the Mermin theorem because the finite size sheets of graphene ($\approx 100\ \mu\text{m}^2$) becomes intrinsically stable.

Electronic band structure of graphene :

Graphene consists of a 2D honeycomb lattice of carbon atoms and it is a *bipartite* lattice. As shown in Figure 1.3, the crystal structure can be considered

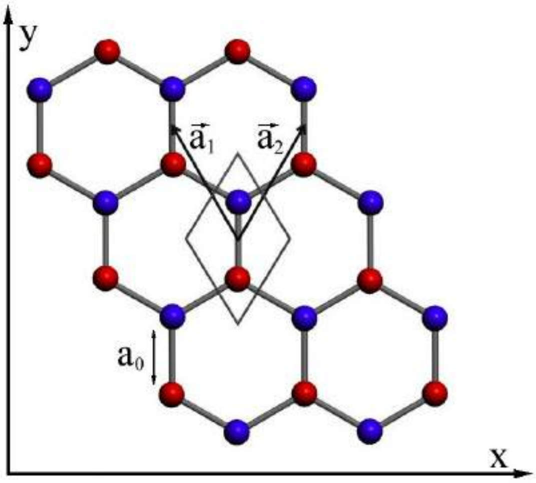

Figure 1.3. The crystal structure of graphene which can be considered as made of two sub-lattices (red and blue). The black rhombus indicates the unit cell and $\vec{a}_1$ and $\vec{a}_2$ represent the lattice's unit vectors.

as made of two sub-lattices (red and blue). The black rhombus indicates the unit cell and $\vec{a}_1$ and $\vec{a}_2$ represent the lattice's unit vectors.

The two unit vectors, $\vec{a}_1$ and $\vec{a}_2$, of the primitive unit cell are described in following equations 1.1 and 1.2:

$$\vec{a}_1 = \frac{a_0}{2}(-\sqrt{3},3) \tag{1.1}$$

$$\vec{a}_2 = \frac{a_0}{2}(\sqrt{3},3) \tag{1.2}$$

where $a_0 \approx 0.142$ nm is the distance between carbon atoms, which is the average of the length of single (C–C) and double (C=C) bonds.

In Figure 1.4 the first Brillouin zone of graphene is shown, including the high symmetry points in momentum space: $\Gamma = (0,0)$, $M = (0, \frac{2\pi}{3a_0})$, $K = (-\frac{2\pi}{3\sqrt{3}a_0}, \frac{2\pi}{3a_0})$ and $K' = (\frac{2\pi}{3\sqrt{3}a_0}, \frac{2\pi}{3a_0})$. Since the unitary cell has two atoms, it contains two π-electrons whose wave functions overlap. As a consequence, the wave function ϕ of the unit cell can be written as a superposition of each atomic wave function ϕ_1 and ϕ_2.

$$\phi(\vec{r}) = c_1\phi_1(\vec{r}) + c_2\phi_2(\vec{r}) = \sum_n c_n\phi_n \tag{1.3}$$

Since the crystal has a periodic structure, we can make the following ansatz for

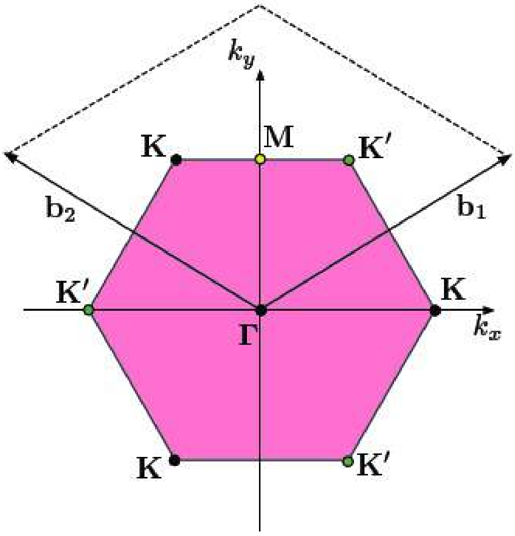

Figure 1.4. The first Brillouin zone of graphene.

the wave function:

$$\psi(\vec{k}) = \sum_{\vec{R}\in G} e^{(i\vec{k}\cdot\vec{R})}\phi(\vec{r}-\vec{R}) \tag{1.4}$$

where G denotes the set of lattice vectors.

In the framework of the tight-binding approximation only the nearest-neighbor atoms can be considered and due to the Bloch theorem the wave function of the blue or red atoms are equal except for the phase factor $e^{i\phi}$, we can write:

$$\psi(\vec{k}) = c_1\phi_1 + c_2\phi_2 e^{-i\vec{k}\vec{a}_1} + c_2\phi_2 e^{-i\vec{k}\vec{a}_2} + c_2\phi_2 + c_1\phi_1 e^{i\vec{k}\vec{a}_1} + c_1\phi_1 e^{i\vec{k}\vec{a}_2} \tag{1.5}$$

The Schrödinger equation for ψ is:

$$H\,|\Psi\rangle = E\,|\Psi\rangle \tag{1.6}$$

Now, if we insert the equation 1.5 in 1.6, and project the equation on the two atomic states, we obtain:

$$\langle\phi_1\,|\,H\,|\,\Psi\rangle = E\,\langle\phi_1\,|\,\Psi\rangle \tag{1.7}$$

$$\langle\phi_2\,|\,H\,|\,\Psi\rangle = E\,\langle\phi_2\,|\,\Psi\rangle \tag{1.8}$$

In order to simplify the problem we define:

$$\alpha = \langle\phi_i\,|\,H\,|\,\phi_i\rangle \tag{1.9}$$

$$\beta = \langle \phi_i \,|\, H \,|\, \phi_j \rangle \tag{1.10}$$

where α is the self-energy and β is the hopping energy between nearest-neighbor sites.

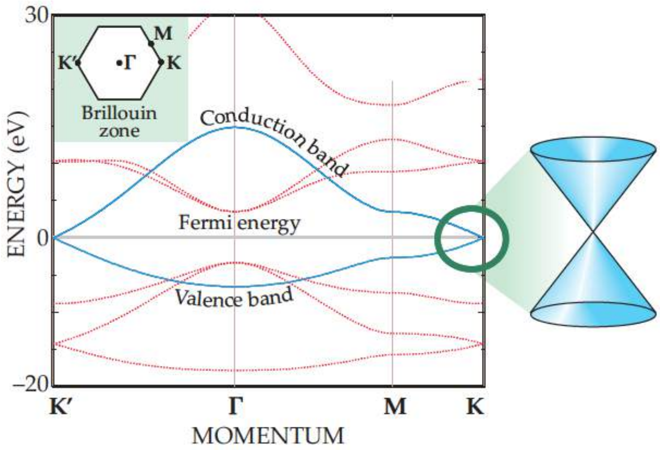

Figure 1.5. The π and π^* bands (blue) decoupled from σ and σ^* bands (red). The π and π^* bands form conical valleys that touch at two of the high-symmetry points, conventionally labeled K and K', in the Brillouin-zone.[8]

Having considered this, the components of equations 1.7 and 1.8 become:

$$\langle \phi_1 \,|\, H \,|\, \Psi \rangle = c_1\alpha + c_2\beta(1 + e^{-i\vec{k}\vec{a}_1} + e^{-i\vec{k}\vec{a}_2}) \tag{1.11}$$

$$\langle \phi_2 \,|\, H \,|\, \Psi \rangle = c_2\alpha + c_1\beta(1 + e^{i\vec{k}\vec{a}_1} + e^{i\vec{k}\vec{a}_2}) \tag{1.12}$$

$$E \,\langle \phi_1 | \Psi \rangle = Ec_1 \tag{1.13}$$

$$E \,\langle \phi_2 | \Psi \rangle = Ec_2 \tag{1.14}$$

Thus the equations can be rewritten as:

$$\begin{pmatrix} \alpha - E & \beta(1 + e^{-i\vec{k}\vec{a}_1} + e^{-i\vec{k}\vec{a}_2}) \\ \beta(1 + e^{i\vec{k}\vec{a}_1} + e^{i\vec{k}\vec{a}_2}) & \alpha - E \end{pmatrix} \begin{pmatrix} c_1 \\ c_2 \end{pmatrix} = 0 \tag{1.15}$$

This system has a non-trivial solution only if:

$$\begin{vmatrix} \alpha - E & \beta(1 + e^{-i\vec{k}\vec{a}_1} + e^{-i\vec{k}\vec{a}_2}) \\ \beta(1 + e^{i\vec{k}\vec{a}_1} + e^{i\vec{k}\vec{a}_2}) & \alpha - E \end{vmatrix} = 0 \tag{1.16}$$

and when solved for the energy E gives the expression of the electronic band-structure for the first Brillouin zone:

$$E = \alpha \pm \beta\sqrt{3 + 2\cos\vec{k}\vec{a}_1 + 2\cos\vec{k}\vec{a}_2 + 2\cos\vec{k}(\vec{a}_1 - \vec{a}_2)} \tag{1.17}$$

where we can arbitrarily set $\alpha = 0$ and $\beta = \gamma_0 \approx 2.8$ eV. Equation 1.17 is commonly expressed explicitly as:

$$E(x, y) = \pm\gamma_0 \sqrt{1 + 2\cos(\frac{\sqrt{3}ak_y}{2})\cos(\frac{ak_x}{2}) + 4\cos^2(\frac{ak_x}{2})} \tag{1.18}$$

where a is the lattice constant ($a = \sqrt{3}a_0$).
From this expression we can distinguish two bands: the π band at $E < 0$ and the π^* at $E > 0$, as represented in Figure 1.5 and 1.6. The reciprocal lattice vectors of this Bravais lattice are:

$$\vec{b}_1 = \frac{2\pi}{3a_0}(-\sqrt{3},1) \tag{1.19}$$

$$\vec{b}_2 = \frac{2\pi}{3a_0}(\sqrt{3},1) \tag{1.20}$$

The bands touch each other at the high symmetry K points, found at the corners of the first Brillouin-zone. Although there are six of these points, only two of them are independent: the K and the K' points form independent valleys in the momentum space.
The π and π^* bands (blue) are decoupled from the σ and σ^* bands (red) because of inversion symmetry and are closer to the Fermi energy because they participate less in bonding (Figure 1.5). The Fermi energy separates occupied and empty states. In a neutral graphene sheet, this is the energy where valence and conduction bands meet (zero energy above, often referred to as the neutrality point). The bands form conical valleys that touch at two of the high-symmetry points, conventionally labeled K and K', in the Brillouin-zone (Figure 1.6). Near these

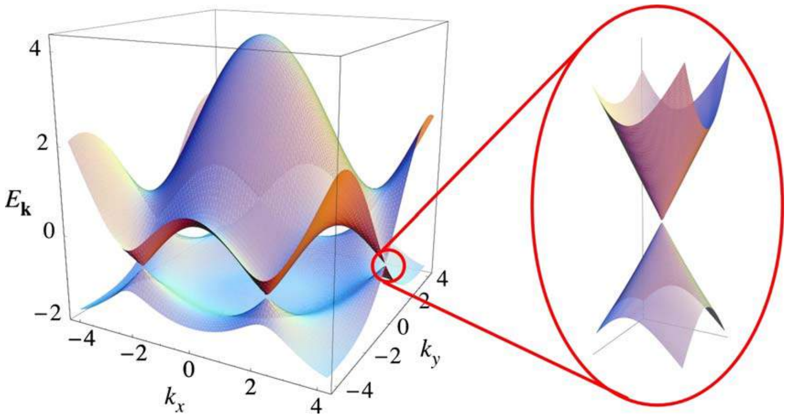

Figure 1.6. The band-structure of graphene in the first Brillouin zone. The inset shows the region around the K-point. The Fermi energy,E_F lies exactly between the conduction and valence band for undoped graphene.[9]

points the energy varies linearly with the magnitude of momentum measured from the Brillouin-zone corners. In general if we have N unit cells, considering spin degeneracy, each band contains $2N$ states. In graphene every unit cell has two electrons, therefore the valence band results completely filled and the conduction band empty with the Fermi energy lying exactly at the points where the two bands touch each other [8, 9].
Due to this particular band-structure, with the density of states vanishing at the K and K' points, graphene is usually defined as zero-gap semiconductor.

Low energy properties

The electronic states close to the Fermi level determine the electronic transport properties of materials. Since for undoped graphene the Fermi energy lies exactly at the K-points, it is possible to describe the low energy transport by expanding the wave functions around $\vec{K}$.
The electronic states in both valleys are not coupled, therefore we can write an effective Hamiltonian for each valley and study it singularly. We consider $\vec{k} = \vec{K} + \vec{\kappa}$ and $\vec{k} = \vec{K}' + \vec{\kappa}$ with $|\vec{\kappa}| \ll |\vec{K}|, |\vec{K}'|$, then equation 1.15 close to $\vec{K}$ can be approximated as:

$$\begin{bmatrix} E(\vec{\kappa}) & \frac{3\gamma_0 a_0}{2}(\kappa_x + i\kappa_y) \\ \frac{3\gamma_0 a_0}{2}(\kappa_x - i\kappa_y) & E(\vec{\kappa}) \end{bmatrix} \begin{bmatrix} c_1 \\ c_2 \end{bmatrix} = 0 \tag{1.21}$$

which operates on a two-component wave function in order to evaluate the contribution of both sublattices.
As usual the dispersion is obtained by setting the determinant to zero:

$$E(\vec{\kappa}) = \pm(\frac{3\gamma_0 a_0}{2})|\vec{\kappa}| \tag{1.22}$$

From this, since the velocity of a wave packet is given by $\vec{v} = \hbar^{-1}\partial E/\partial\vec{\kappa}$, we can write the Fermi velocity:

$$v_F = \frac{3\gamma_0 a_0}{2\hbar} \tag{1.23}$$

which is independent by the direction hence, close to the K points, the band-structure of graphene is a cone.
Since the parameters involved are known ($\gamma_0 \approx 2.8$ eV and $a_0 = 1.42$ Å), we have $v_F \approx 10^6$ m/s and we can rewrite equation 1.22 in a much simpler way:

$$E(\vec{\kappa}) = \pm v_F|\vec{\kappa}| \tag{1.24}$$

An interesting property of graphene can be found by inspecting the electronic wave functions. The effective Hamiltonians give rise to two-component wave functions

for each valley:
for K

$$\psi_{\pm K}(\vec{\kappa}) = \frac{1}{\sqrt{2}} \begin{pmatrix} e^{-i\theta_{\vec{\kappa}}/2} \\ \pm e^{i\theta_{\vec{\kappa}}/2} \end{pmatrix} \tag{1.25}$$

and for K'

$$\psi_{\pm K'}(\vec{\kappa}) = \frac{1}{\sqrt{2}} \begin{pmatrix} e^{i\theta_{\vec{\kappa}}/2} \\ \pm e^{-i\theta_{\vec{\kappa}}/2} \end{pmatrix} \tag{1.26}$$

where $\theta_{\vec{\kappa}} = tan^{-1}(\kappa_x/\kappa_y)$ is the angle of the wave vector $\vec{\kappa}$ in momentum space and ± refers to the energies following equation 1.24.
The wave functions have two components with spinor-like properties and are therefore called pseudo-spinors. From this it derives that, a rotation of $\theta_{\vec{\kappa}} = 2\pi$ around a K point leads to a π phase shift of the wave function.
It takes two turns to come back to the initial state. This π phase shift is in general known as a Berry's phase. Moreover, the low-energy Hamiltonian can be rewritten as:

$$H_{\vec{\kappa}} = \hbar v_F \sigma \cdot \vec{\kappa} = -i\hbar v_F \sigma \cdot \Delta \tag{1.27}$$

where $\sigma = \sigma_x \hat{x} + \sigma_y \hat{y}$ with σ_x and σ_y being the Pauli matrices.
In quantum mechanics, the helicity operator is given by: $\hat{h} = \frac{1}{2}\sigma\frac{\vec{\kappa}}{|\vec{\kappa}|}$ and is the projection of the pseudo spin along the momentum direction. With $H_{\vec{\kappa}} |\psi_\pm\rangle = E_{\vec{\kappa}} |\psi_\pm\rangle$ and $E_{\vec{\kappa}} = \pm\hbar_F|\vec{\kappa}|$, we obtain: $\sigma\frac{\vec{\kappa}}{|\vec{\kappa}|} = \pm 1$. As a consequence, at the K-point, the pseudo-spin is parallel to the momentum for positive energies and anti-parallel for negative energies.
This fact has important consequences for the electric conduction in graphene since, the conservation of this pseudo-spin lead to a suppression of scattering mechanisms. Another important observation is that the effective Hamiltonian of graphene is equivalent to the Dirac equation in the mass-less case [9]. This means that the low-energy charge carriers in graphene behave as mass-less chiral spin 1/2 relativistic particles, also called $Dirac\ fermions$. The only differences are that in graphene the speed of light is replaced by the Fermi velocity, which is $v_F \approx c/300$, and the real spin is replaced by the pseudo-spin.
Graphene is the first material in which such particular carriers have been observed and this makes it extremely interesting from the point of view of fundamental research. [10]

Density of states

The density of states of a graphene single-layer, as derived from equation 1.17 is shown in Figure 1.7 as a function of the next-nearest-neighbor hopping parameter γ_1. For both $\gamma_1 = 0$ and $\gamma_1 \neq 0$, the semi-metallic behavior is evident [5, 11], but in the latter case the symmetry between electrons and holes is lost. In the

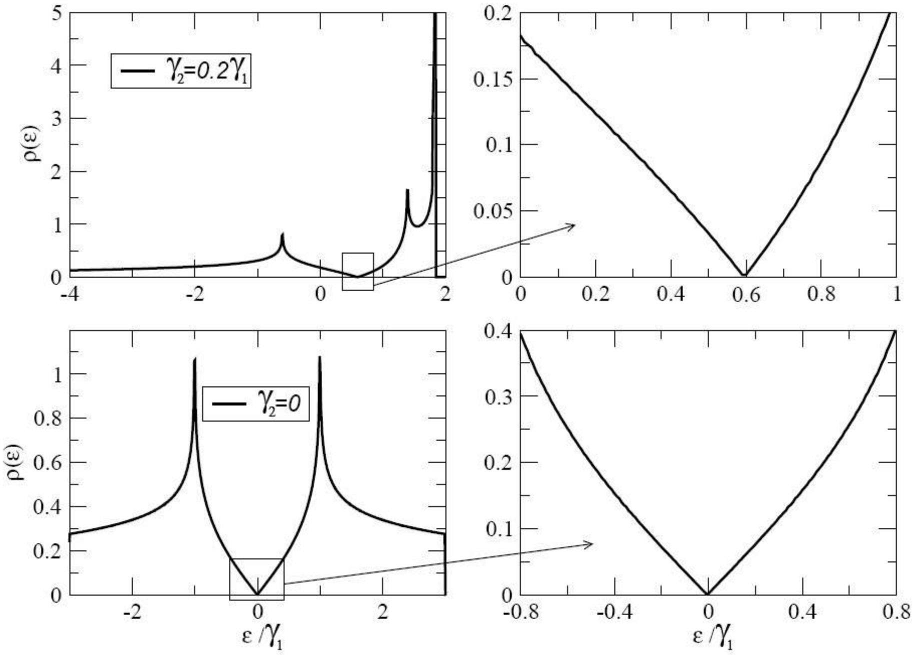

Figure 1.7. Density of states as a function of energy for graphene single-layer plotted in units of nearest-neighbor hopping energy γ_0. It is possible to see the linear behavior $\rho(E) \propto |E|$ and the symmetry breaking between electrons and holes, if non negligible γ_1 is considered. Right: zoom of the K points. (edited from [9])

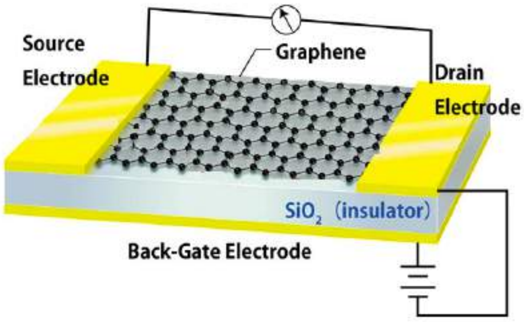

Figure 1.8. Schematic of a field-effect device fabricated with a graphene flake deposited on Si/SiO_2. The substrate is an important part of the device since the $n^{++}Si$ layer is used as a back-gate electrode, with the SiO_2 layer being the gate dielectric.

low energy regime it is possible to write the following expression for the density of states:

$$\rho(E) = \frac{2A_c}{\pi}\frac{|E|}{v_F^2} \tag{1.28}$$

where A_c is the area of the unit cell in real space, given by: $A_c = 3\sqrt{3}a^2/2$.

1.1.2 Transport properties

Electronic transport in single – layer graphene

The transport properties of graphene have been extensively studied by fabricating field-effect devices in a configuration as shown in Figure 1.8. Graphene's quality can be assessed by the pronounced ambipolar effect such that charge carriers can be tuned continuously between electrons and holes. It is possible to continuously modulate the density of charge carriers by polarizing the SLG sheet with respect to the gate electrode, thereby moving the Fermi level through the Dirac cones.

In Figure 1.9 the material resistivity as a function of back-gate voltage is shown; these kind of curves are popularly known as Dirac curves.

The concentrations n can be as high as 10^{13} cm^{-2} and their mobilities μ can exceed 15,000 cm^{2}V^{-1}s^{-1} under ambient conditions. Moreover, the observed mobilities weakly depend on temperature T, which means that μ at 300 K is still limited by impurity scattering, and therefore can be improved significantly, even up to $\approx$ 100,000 cm^{2}V^{-1}s^{-1}.

At $n > 10^{12}$ cm^{-2}, μ remains high in both electrically and chemically doped devices, although ballistic transport is observed on the sub-micrometer scale, up to ≈ 0.3 μm at 300 K.

Transport in graphene under magnetic field

The standard Hall effect measurements are able to extract important information about the type and concentration of charge carriers present in the material as a function of gate voltage. Transport properties of graphene can be studied by fabricating FEDs with the configuration sketched in Figure 1.10. Hall effect measurements allows to get important information on the type and the concentration of charge carriers in the material as a function of the back-gate voltage.

The Hall resistance is linear with respect to V_G on which depends the charge carrier concentration:

$$\frac{1}{R_H} = ne = \alpha V_G \tag{1.29}$$

Positive (negative) V_G induces electrons (hole) in concentrations $n = \alpha V_G$. Estimating the charges induced by the back gate in a field-effect device fabricated

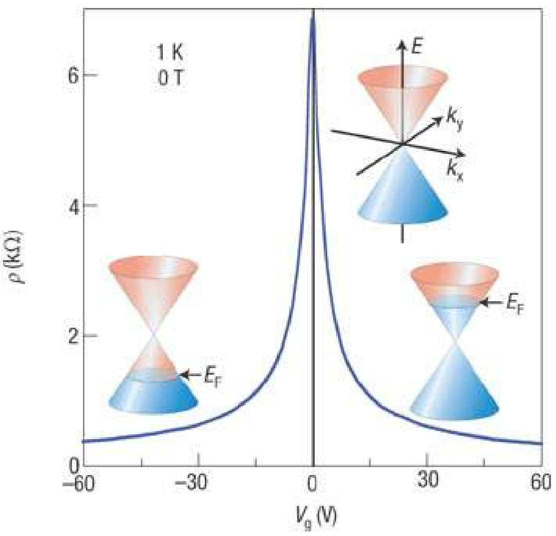

Figure 1.9. Ambipolar electric field-effect in single-layer graphene. The insets show its conical low-energy spectrum $E(k)$, indicating changes in the position of the Fermi energy, E_F with changing gate voltage V_G. Positive (negative) V_G induce electrons (holes) in concentrations $n = \alpha V_G$ for field-effect devices shown in Figure 1.8 with 300 nm SiO_2 layer used as a dielectric.[12]

with a graphene flake deposited on Si/SiO_2 theoretically gives the value of the coefficient α:

$$\alpha_{th} = \frac{n}{V_G}\frac{\epsilon_0\epsilon}{te} \cong 7.2 \times 10^{10}\ cm^{-2}V^{-1} \tag{1.30}$$

which is readily comparable to experimental value:

$$\alpha_{exp} \cong 7.3 \times 10^{10}\ cm^{-2}V^{-1} \tag{1.31}$$

This indicates that major part of the induced charge carriers participate in conduction. Charge trapping at the graphene/SiO_2 interface is negligible, which testifies the high crystallographic quality of the material.
Such quality gets evident also while evaluating the Hall mobility μ of the induced charges.

$$\mu = \frac{\sigma}{ne} \tag{1.32}$$

For very good samples μ can be as high as 10^6 $\mathrm{cm^2V^{-1}s^{-1}}$. [13]

Cyclotron Mass

The energy dispersion relationship of electrons in graphene resembles the energy of ultra relativistic particles in the quantum mechanical regime [13, 14]. These

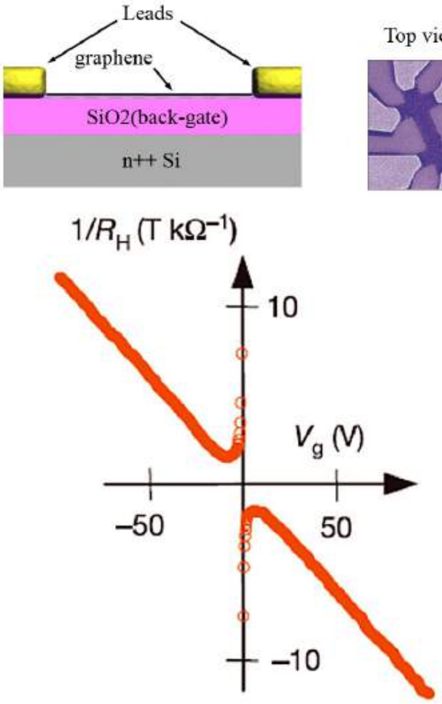

Figure 1.10. In the upper part, side and top view of a graphene device is shown. In the graph below, the behavior of the classical Hall resistance as a function of the back-gate voltage.(adapted from [13])

mass-less Dirac fermion particles are characterized by cyclotron mass that depends on the electronic density as its square root. The cyclotron mass is defined in a semiclassical approximation as:

$$m^* = \frac{1}{2\pi}[\frac{\partial A(E)}{\partial E}]_{E=E_F} \tag{1.33}$$

where $A(E)$ is the area, in the momentum space, defined by the particle's orbit, and is given by:

$$A(E) = \pi\frac{E^2}{v_F^2} \tag{1.34}$$

By putting together equations 1.33 and 1.34, we obtain:

$$m^* = \frac{E_F}{v_F^2} = \frac{k_F}{v_F} \tag{1.35}$$

The density of states n depends on the Fermi momentum: $k_F^2 = \pi n$
Thus we have,

$$m^* = \frac{\sqrt{\pi}}{v_F}\sqrt{n} \tag{1.36}$$

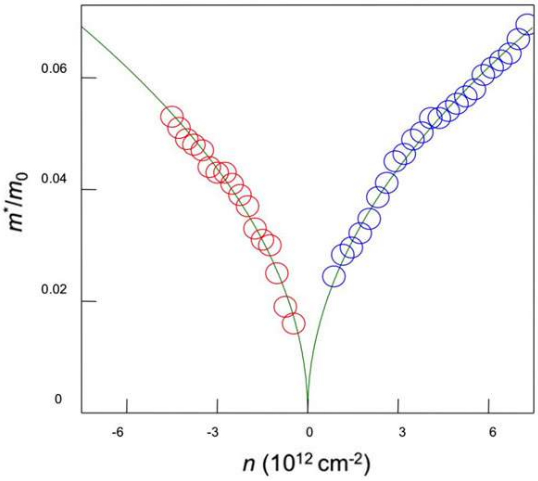

Figure 1.11. Plot of the cyclotron mass of charge carriers in single-layer graphene as a function of their concentration n. Experimental values have been derived by the analysis of temperature dependence of the Shubnikov de Haas oscillations as a function of temperature, while the solid line represents the fit based on equation 1.38 with v_F as free parameter. m_0 is the free electron mass. (edited from [9])

with the spin and valley degenerations being already considered.

In Figure 1.11 it is possible to see how equation 1.36 can easily fit the experimental data, giving also the possibility to verify that $v_F \approx 10^6$ m/s and consequently $\gamma_0 \approx 2.8$ eV. The experimental observation of the square root dependence of the cyclotron mass on the carrier concentration is the proof of the presence of a linear dispersion relation and thus of massless Dirac fermions in single-layer graphene [13, 14, 15]. Indeed, the common parabolic dispersion relation leads to constant cyclotron mass [16].

Quantum Hall effect in graphene

Since graphene is a two-dimensional material, therefore it is expected to observe the quantum Hall effect (QHE) in this material. However in single-layer graphene the quantization of the Hall conductivity develops in a very particular way. The Hall plateau are quantized as:

$$\sigma_{xy} = \pm(N + \frac{1}{2})\frac{ge^2}{h} \tag{1.37}$$

with g=4 being the degeneracy factor, 2 for spin and 2 for valley degeneration (or carrier's chirality).

The origin of such *half integer* QHE lies in the Landau levels spectrum of

chiral massless Dirac fermions which are responsible for electronic conduction in graphene. Therefore, the observation of the half integer QHE became, together with cyclotron frequency, the evidence for the observation of massless Dirac fermions and thus of a graphene single-layer.
In presence of a magnetic field directed along z-direction, we can write the graphene Hamiltonian for the K point, considering the momentum operator $p \rightarrow p - e\vec{A}$ and the Landau gauge $\vec{A} = (0, xB, 0)$, as:

$$\pm v_F \begin{pmatrix} 0 & p_x - ip_y + xeB \\ p_x + ip_y - xeB & 0 \end{pmatrix} \begin{pmatrix} \psi_A(r) \\ \psi_B(r) \end{pmatrix} = E \begin{pmatrix} \psi_A(r) \\ \psi_B(r) \end{pmatrix} \tag{1.38}$$

Solving these equations leads to an energy dispersion equal to:

$$E_N = \pm\sqrt{(2v_F B(N + \frac{1}{2} \pm \frac{1}{2}))} \quad N = 0, \pm 1, \pm 2... \tag{1.39}$$

where N is the Landau level index.

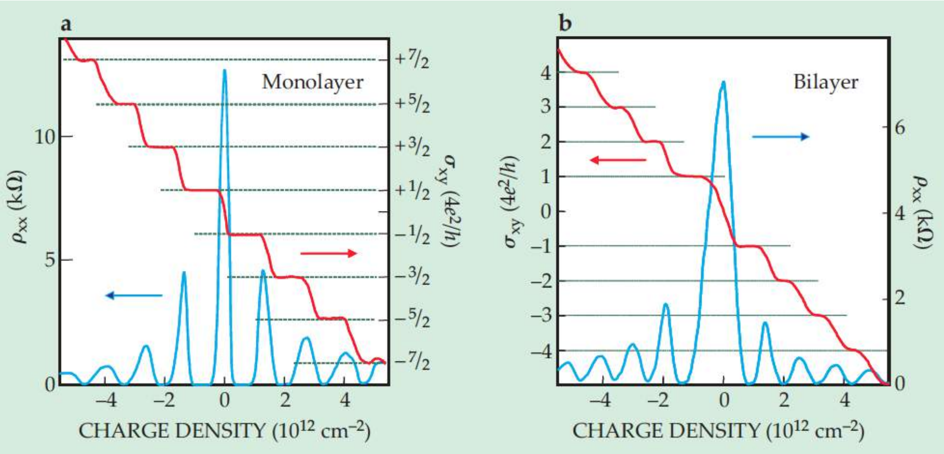

Figure 1.12. Quantum Hall effect in single-layer graphene on left and bilayer graphene on right.[17]

The first ± takes into account the ambipolar nature of graphene and the $\pm 1/2$ factor from the chirality of charge carriers. This last term is important for the development of the peculiar level at zero energy, which results equally shared between electrons and holes of opposite chirality. This level is robust and does not depend on the applied magnetic field.

In Figure 1.12 Quantum Hall effect in graphene as a function of charge-carrier density n is shown. In single-layer graphene the peak in the longitudinal resistivity

ρ_{xx} at $n = 0$ demonstrates that a Landau level occurs at zero energy. The values of the transverse conductivity ρ_{xy} at the surrounding plateaus imply that this level is drawn half from the conduction band and half from the valence band. The QHE proves that charge carriers in single-layer graphene are massless Dirac fermions. In bilayer graphene the double-jump in σ_{xy} at $n = 0$ demonstrates that two Landau levels are pinned at zero energy. This quantization reveals that bilayer graphene is made up of massive and chiral fermions. However, the QHE in graphene was observed even at room temperature. [18, 19, 20]

As stated earlier, the nature of spectrum around the wave numbers K and K' determine the transport properties of graphene. Close to K and K' the dispersion is conical and is given by $E(k) = \pm v_F \hbar k$, with $v_F = 3ta_0/(2\hbar)$, where k is the momentum measured relatively to either K or K'. This spectrum is formally equivalent to that obtained from solving the 2D massless Dirac equation. The Hamiltonian for the electrons in graphene has the form $H_K = v_F \sigma.p$ whereas close to K', the Hamiltonian is $H_{K'} = -H_K$. The operator σ is written in terms of Pauli matrices as $\sigma = (\sigma_x, \sigma_y)$ and is called as the pseudo spin while p is the momentum operator. The density of states $N(E) = K^2 A_c/(2\pi)$, from which the density of states $\rho(E)$ per spin per unit cell is given by $\rho(E) = dN(E)/dE = 2|E|/\pi\sqrt{3}t^2$, and the primitive cell area $A_c = 3\sqrt{3}a_0^2/2 \approx 5.1$ Å^2 [21].

Since $\sigma.p|\psi>= \pm p|\psi>$, then the operator $\hat{h}$ has only two eigenvalues ± 1. The helicity operator $\hat{h}$ has the following physical interpretation: in an energy eigenstate, the pseudo spin is either parallel or antiparallel to the momentum p. As shown in Figure 1.13, at the K valley, electrons have positive helicity, $h = 1$, whereas at the K', the helicity is negative ($Q = K' - K$ represents the transferred momentum when a scattering event between the valleys takes place). In a head-on collision of the electron on a potential barrier, the backscattered electron has to change its momentum from q to $-q$. For such a head-on collision (taken here along the x direction), $\hat{h}$ is a constant of motion, with eigenvalue $+1$, but backscattering would imply a modification of this eigenvalue to -1. This, however, cannot be because $\hat{h}$ is a conserved quantity, then the transmission probability through the barrier, for such type of collision, has to be one. Thus, backscattering is suppressed for intravalley scattering events. On the other hand, electrons in the K and K' valleys have opposite chirality, thus intervalley backscattering can take place if the potential is short range since in this case the eigenvalue of $\hat{h}$ does not change sign [10, 21]. The helicity or chirality of electrons in graphene is responsible for the Klein tunneling effect: the probability of electronic transmission through a potential barrier is equal to 1 for head-on collisions and backscattering is said to be suppressed.

However, chirality is not an exact symmetry of the problem because the spectrum of graphene is not exactly linear at all energies. The deviation from the

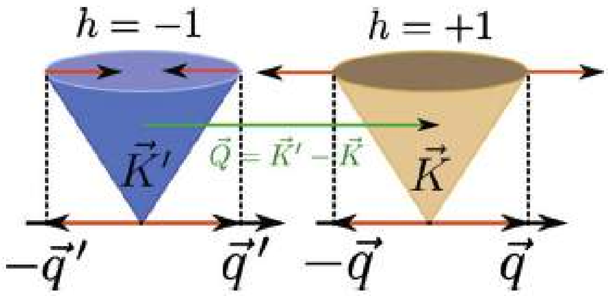

Figure 1.13. Positive helicity $h = +1$ at K valley and negative helicity $h = -1$ at K' with transferred momentum as $Q = K' - K$ during a scattering event between valleys takes place.[21]

perfect massless Dirac behavior is known as trigonal warping.

The intervalley scatterings are originated by some adatoms, adsorbed hydrocarbons, vacancies or edges of the sample. Since the electrons in the two valleys are related by time reversal symmetry, the phases acquired by two electrons, one in the K valley and its time-reversed at K' are equal, allowing constructive interference. Instead intravalley scatterings arise from long-range scattering potentials, such as ripples, dislocations, charged impurities or topological defects. This type of scattering randomizes the phase within a valley suppressing interference effects from the same valley and thus localization effects.

1.1.3 Types of graphene

The starting point of the discovery of graphene came up with the idea that it can be produced through a mechanical exfoliation technique [7]. It became possible to exfoliate graphene by using an adhesive tape and later depositing it on an appropriate substrate. Most common choice is Si/SiO_2 for the deposition of graphene and then it becomes possible to observe it under the microscope and characterize it. However different synthesis and fabrication processes result in graphene with atomic structures like almost perfect and mono-crystalline, as well as defective and polycrystalline. In the latter case, defects can appear in the form of grain boundaries, ripples, wrinkles and point defects within the graphene crystal structure. Other methods developed for the production of graphene include chemical vapor deposition (CVD) of graphene on transition metal foils [22, 23] and epitaxial growth on SiC [24, 25], which are promising as well. For our work we have used the exfoliation technique of graphite and the CVD of graphene on copper foils to prepare field-effect devices. A brief description of both the methods is given here:

1. mechanical exfoliation of highly oriented pyrolytic graphite (HOPG) to obtain single layer and FLG:

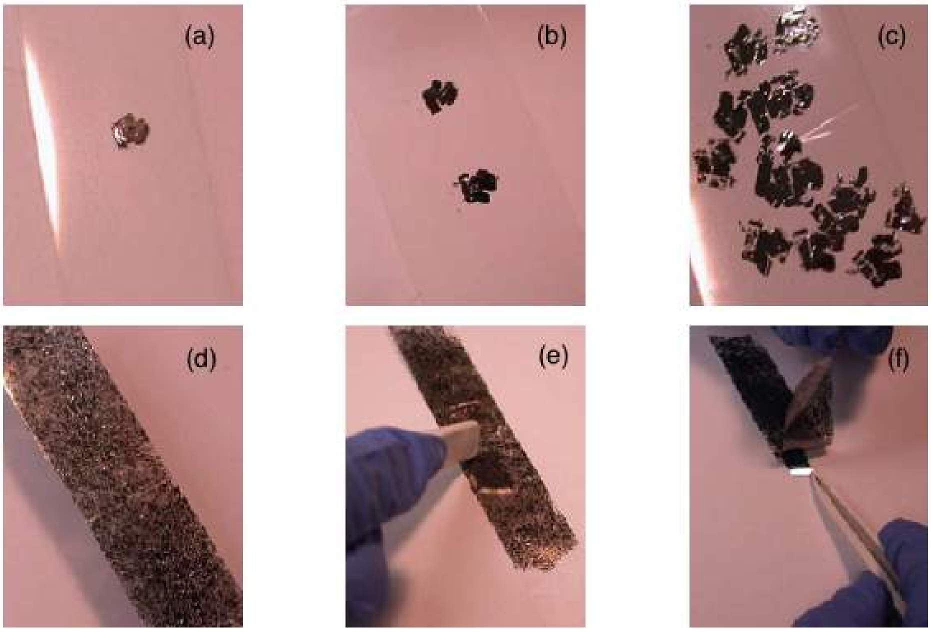

Figure 1.14. Production of graphene by micro-mechanical exfoliation of graphite. (a) With the adhesive part of the tape a thin layer of graphite is extracted from a bulk sample. (b) By folding the tape, the adhesive part is brought in contact with the other side of the graphite layer and the first layer of graphite is split into two. (c) The same procedure is repeated several times in order to distribute the graphite all over the tape. (d) Until a situation shown here is obtained with graphite homogeneously distributed all over the tape. (e) the tape is then put into contact with the Si/SiO_2 substrate and firmly pressed with a thumb or with the back of tweezers. (f) finally, by using tweezers, the tape is gently detached from the substrate, which is now ready for optical inspection.[26]

The starting graphitic material source we used are HOPG, natural graphite flakes and graphite powder. Materials needed for this procedure are: the adhesive tape, small pieces of bulk graphite and the substrate. The exfoliation procedure is shown and described in the series of pictures of Figure 1.14. First of all, the piece of graphite is pressed on the adhesive tape and a thin graphite layer is peeled off the bulk. Then, with repeated exfoliation using the same tape, the graphite layer is thinned and homogeneously distributed on the surface of the tape. Finally the tape is pressed on the substrate and gently rubbed with tweezers or fingers.

When the tape is removed, a procedure must to be carried out carefully in order to avoid damage to the graphene flakes and thin flakes remain deposited on the substrate. Optical inspection and characterization showed that some of this flakes are made of thick graphite, some of them are much thinner and made just of few graphene planes down to monolayers. A few aspects of this procedure must be considered in order to optimize it and improve the quality of the obtained graphene flakes. The development and optimization of graphene production has been one of the most important part of the work carried out at Istitito Nazionale di Ricerca Metrologica (INRIM) earlier and at the University of Cambridge (Cambridge, United Kingdom) later, since the fabrication of graphene devices for polymer gating measurements require large high quality few-layer graphene flakes [27]. Every Si/SiO_2 substrate used for graphene deposition was carefully cleaned in acetone with the help of an ultrasonic bath and rinsed in IPA before being dried with nitrogen.

Another thing to be considered is the tape used for the exfoliation. Despite the fact that most of the tapes available can be used for the purpose, certain tapes have important advantages. Indeed, semiconductor tapes such as the $Nitto\ BT-150E-KL$ can deposit flakes without leaving many glue residuals on the substrate's surface, that can represent a serious issue for the fabrication of devices. On the other hand, tapes with very strong adhesive power such as the common $3M\ scotch$ have proven to be very effective in graphene deposition, with the disadvantage of leaving a lot of glue residuals. With all these materials, groups around the world have demonstrated to be able to produce high quality graphene flakes after the optimization of the exfoliation recipe. In our case we used natural graphite flakes with lateral size of few millimeters with very good results in terms of number and quality of the produced graphene flakes. Once deposited, the graphene flakes needs to be characterized in order to measure the number of graphene layers composing them [27].

2. CVD of single layer graphene on copper foils - graphene growth on copper involves the decomposition of methane gas over a copper substrate typically held around 1000°C. The process is carried out in two steps: precursor pyrolysis to carbon and the formation of the graphitic structure from dissociated carbon atoms. The precursor dissociation should happen only on the substrate surface (heterogeneous reaction) to avoid the precipitation of carbon clusters in the gas phase which then diffuse on synthesized graphene. Although they are all made of carbon, the amorphous structure of these clusters determines that their composite no longer retains the properties of monolayer graphene. Elemental metals, and in particular copper, work as catalysts to lower the energy barrier of the reaction: this is to reduce the needs for extremely high temperature and the temperature dependence for the reaction rates, whose control is critical for grown graphene quality control [28]. Critical parameters to be controlled are pre-annealing gas source type (typically hydrogen) and growth pressure, time, temperature, gas flow rates and cooling rate. A large number of different combinations of the aforementioned parameters are possible, leading to a proportional variety in recipes present in the

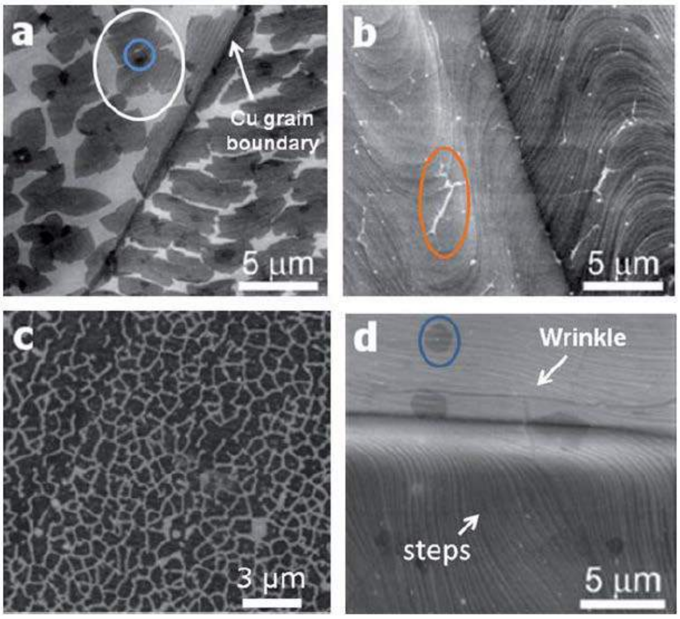

Figure 1.15. SEM images of graphene on Cu for different growth times: (a) 1 min; (b) 2.5 min; (c) 1 min with different pre-treatment conditions for comparison; and (d) 10 min[29]

literature. Most of the depositions are performed on copper foils with thicknesses ranging from 25 to 50 μm [29]. Although the most commonly used deposition temperature is 1000°C, growth at temperatures ranging from $800 - 950$°C have been reported. The CVD of graphene on copper is done under low ($0.67 - 67$ mbar) or atmospheric pressure of methane and hydrogen gas mixtures at various ratios [29]. Among the several steps for CVD growth of graphene on copper, pre-treatment of copper foils is extremely important to obtain large graphene domains. This ensures high-quality graphene deposition thereby ensuring no particle contamination on the copper substrates. Since the bought copper foils are covered by native copper oxide which could reduce catalytic activity, these foils undergo an annealing treatment at 1000°C in an hydrogen atmosphere. In Figure 1.15, the growth of single-layer graphene at different times is shown through scanning electron microscope (SEM) images. In Figure 1.15 (a) graphene flakes of finite size (as indicated by the oval) can be seen; the smaller oval indicates the nucleation site for one of the flakes. As the growth time is increased, the graphene domains progressively increase in size until coalescing (Figure 1.15 (b)) into a continuous layer; this image is taken just before the formation of a continuous layer, as indicated by the presence of discontinuities (highlighted by the corresponding oval). From this image it is clear that the nucleation density and, therefore, the size of the graphene flakes (Figure 1.15 (c)) is critically tuned by the pre-treatment conditions, the partial pressure of CH_4 and the total growth pressure [29]. After the nucleation, growth, and formation of a single monolayer, further exposure to the carbon precursor for up to 60 min does not lead to a deposition of few-layered graphene (Figure 1.15 (d)).

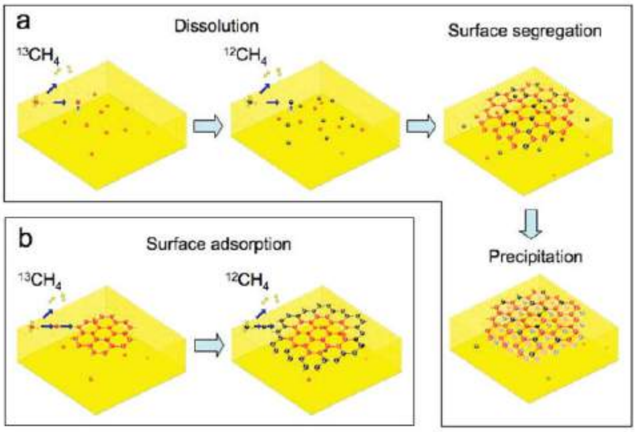

Figure 1.16. Schematic diagrams of the possible distribution of C isotopes in graphene films based on different growth mechanisms for sequential input of C isotopes. (a) Graphene with randomly mixed isotopes such as might occur from surface segregation and/or precipitation. (b) Graphene with separated isotopes that might occur by surface adsorption.[30]

The mechanism for graphene growth on copper is surface related and can be related to the low solubility of carbon in copper, which confines the growth of graphene on the Cu surface and stops it once the entire catalytic surface has been covered. In principle, this self-control mechanism limit the growth to a single layer of graphene. Evidence for this phenomenon has been provided by an elegant set of experiments done by the Ruoff group [30] using isotopic labeling of the methane precursor gas. They utilized a sequenced dosing of $^{12}_{4}$CH and $^{13}_{4}$CH into the growth furnace on copper and measured the distribution of ^{12}CH and ^{13}CH graphene domains (Figure 1.16).

1.1.4 Role of substrate and associated defects

Graphene was eventually spotted due to the subtle optical effect it creates on top of a chosen SiO_2 substrate [6] that allows its observation with an ordinary optical microscope. Therefore, it is important to accurately study the graphene and its substrate interaction to improve device performance especially to enhance parameters like carrier mobility, size homogeneity and low contact resistance. The sources of disorder in graphene are many: among the intrinsic sources are surface ripples and topological defects. Extrinsic disorder can come about in many different forms: adatoms, vacancies, charges on top of graphene or in the substrate, and extended defects such as cracks and edges [9]. Being one atom thick graphene is extremely sensitive to doping effects caused by various molecules adsorbed on its surface. In particular water is present abundantly in atmosphere and is known to induce a strong p-type doping in the material which could limit the device performance in ambient conditions.

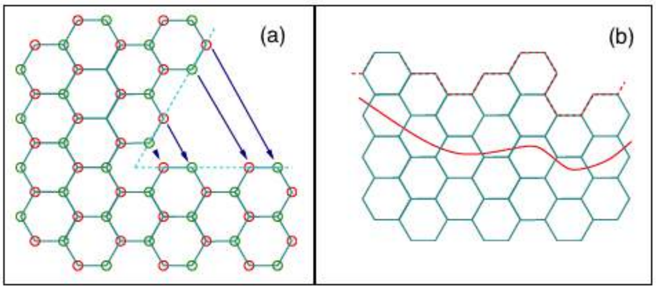

Figure 1.17. (a) Sketch of the boundary conditions associated to a disclination (pentagon) in the honeycomb lattice. (b) a rough graphene surface, the full line gives the boundary beyond which the lattice can be considered undistorted. (edited from [9])

Also graphene grown in different ways may be heavily doped due to the charge transfer from the substrate to the graphene layer with the chemical potential well above the Dirac point. Nevertheless, the presence of a substrate or scaffolds that hold graphene in place can stabilize a certain degree of order in graphene but leaves behind the so-called ripples.

These ripples in its structure (either due to thermal fluctuations or interaction with a substrate, scaffold, and absorbants) occurs because of the modification of the distance and relative angle between the carbon atoms due to the bending of the graphene sheet. This bending has three main effects: the decrease of the distance between carbon atoms, a rotation of the p_Z orbitals and a re-hybridization between and orbitals [31].

However, structural defects of the honeycomb lattice like pentagons, heptagons, and their combinations such as a combination of two pentagon-heptagon pairs are also possible and can lead to scattering (Figure 1.17 (a)). These defects induce long-range deformations, which modify the electron trajectories.

Point defects, similar to impurities and vacancies, can nucleate electronic states in their vicinity. Hence, a concentration of n_i impurities per carbon atom leads to a change in the electronic density of the order of n_i. The corresponding shift in the Fermi energy is $\epsilon_F \simeq v_F\sqrt{n_i}$.

Localized states (edges where number of atoms in two sub-lattices is not compensated) develop at the edges, cracks and voids. In general, a boundary inside the graphene material will exist, as shown in Figure 1.17(b), beyond which sp^2 hybridization is well defined.

1.2 Properties of few layer graphene

As we know, stacking many single layers of graphene produces from FLG to graphite and it is very interesting to study the fundamental Physics of these structures. The simplest of all the structures is a bilayer graphene composed of two single layer graphenes one stacked above the other. It is interesting because it has been shown that a band gap can be opened between the conduction and valence band and can be tuned. Although the interlayer coupling drastically changes the band structure of FLG, its electronic structure is closely related to 3D graphite. Hence this gives FLG a characteristic feature that depend on the number of layers and the stacking order, .

1.2.1 Band structure of bilayer graphene

For bilayer graphene, in the tight binding model, not only the interaction between in-plane nearest neighbors, but also interactions between neighbors in different layers are considered. Therefore, for the calculation of the band structure the type of layer stacking here considered is *AB*-stacking, also called the *Bernal* stacking.

As a first approximation, we can consider only the in-plane nearest neighbor hopping energy γ_0 and the out-of-plane nearest neighbor hopping energy $\gamma_1 \approx 0.39$ eV called the $inter - layer\ coupling$ [14]. The effective Hamiltonians in the low-energy limit for both valleys of bilayer graphene is:

$$H = \xi \begin{pmatrix} \Delta & 0 & 0 & \hbar v_F(k_x - ik_y) \\ 0 & -\Delta & \hbar v_F(k_x + ik_y) & 0 \\ 0 & \hbar v_F(k_x - ik_y) & -\Delta & \xi\gamma_1 \\ \hbar v_F(k_x + ik_y) & 0 & \xi\gamma_1 & \Delta \end{pmatrix} \tag{1.40}$$

where $\xi = 1$ in order to consider the two valleys and $\pm\Delta$ are the on-site energies for the first and second layer. When these are equal ($\Delta = 0$), so there is no asymmetry between the two layers, the energy dispersion close to the K points can be written as:

$$E_k = \pm\frac{\gamma_1}{2} \pm \sqrt{\frac{\gamma_1^2}{4} + (\hbar v_F k)^2} \tag{1.41}$$

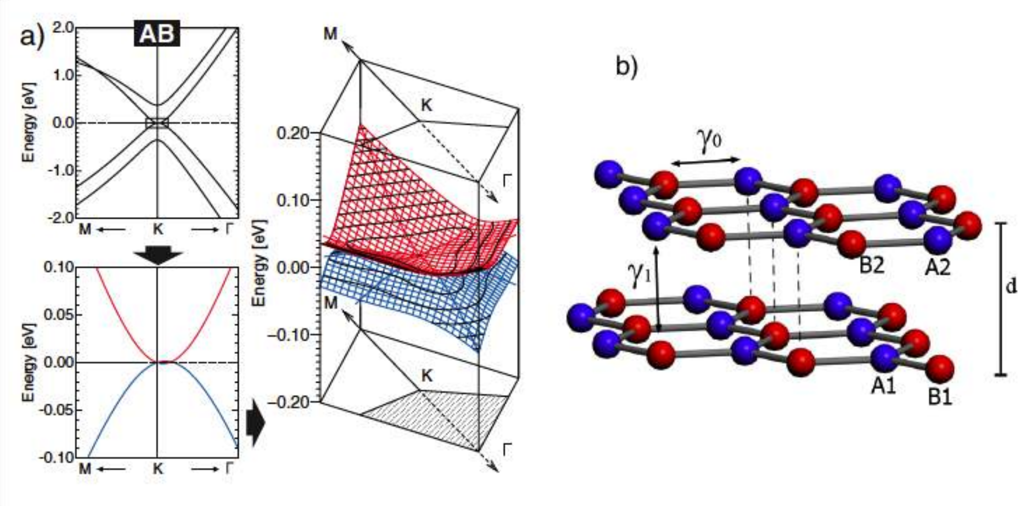

Figure 1.18. a) Details of bilayer graphene band structure in the vicinity of K and near the Fermi level; the valence band is in blue and the conduction band in red, (these results have been obtained by DFT calculations) b) lattice structure of the bilayer with the various hopping parameters. The sub-lattices A are indicated by blue spheres and B by red spheres. (adapted from [33])

with $v_F = \frac{3\gamma_0 a}{2\hbar}$. Thus, bilayer graphene has two valence and two conduction bands as seen in plot of Figure 1.18 (a). In the low-energy limit we can only consider the lowest conduction band and the highest valence band that touch each other at $E_F = 0$. Therefore the effective Hamiltonians for these bands can be written as:

$$H = -\frac{\hbar^2}{2m}\begin{pmatrix} 0 & (k_x \mp ik_y)^2 \\ (k_x \pm ik_y)^2 & 0 \end{pmatrix} \tag{1.42}$$

for the K and K' point respectively. Such Hamiltonian operate on a two component wave function, just as in the monolayer case in order to take into account the two sublattices, but here the two components are related to sublattices belonging to two different graphene planes. This Hamiltonian leads to an energy dispersion relation:

$$E_k = \pm\frac{\hbar^2 k^2}{2m} m = \gamma_1/v_F^2 \tag{1.43}$$

Electrons in bilayer have a finite effective mass m.

The two-component wave functions of the effective Hamiltonian are, for K:

$$\psi_{\pm K}(\vec{\kappa}) = \frac{1}{\sqrt{2}}\begin{pmatrix} e^{-i\theta_{\vec{\kappa}}} \\ \pm e^{i\theta_{\vec{\kappa}}} \end{pmatrix} \tag{1.44}$$

and for K',

$$\psi_{\pm K'}(\vec{\kappa}) = \frac{1}{\sqrt{2}} \begin{pmatrix} e^{i\theta_{\vec{\kappa}}} \\ \pm e^{-i\theta_{\vec{\kappa}}} \end{pmatrix} \tag{1.45}$$

here, the electrons behave as massive chiral particles and the Berry's phase is 2π instead of π as in SLG.

If some sort of asymmetry is introduced between the two layers, the diagonal terms of the Hamiltonian become different from zero. In this case the effective low energy Hamiltonian becomes:

$$H = \begin{pmatrix} \Delta & -\frac{\hbar^2}{2m}(k_x \mp ik_y)^2 \\ -\frac{\hbar^2}{2m}(k_x \pm ik_y)^2 & \Delta \end{pmatrix} \tag{1.46}$$

and hence,

$$E_k = \pm\sqrt{\Delta^2 + (\frac{\hbar^2 k^2}{2m})^2} \tag{1.47}$$

and this is an energy gap

$$E_g = 2\Delta \tag{1.48}$$

at the K, K' points. In [34] the authors have experimentally demonstrated that it is possible to induce and tune such a gap by introducing an asymmetry between the two layers by means of an electric field perpendicular to the graphene plane, which can be realized with the combination of a top-bottom electrostatic gating. This possibility makes graphene bilayer extremely promising for the realization of high speed and low-power transistors for digital computing.

1.2.2 Band structures of few layer graphenes

For describing the electronic properties of a trilayer graphene, many coupling energies between the different sub-lattices in the layers have to be used in the tight-binding band-structure calculation. These are: $\gamma_0 \approx 3.16$ eV and $\gamma_1 \approx 0.39$ eV, which are the same of bilayer graphene, $\gamma_2 \approx -0.019$ eV, $\gamma_3 \approx 0.315$ eV, $\gamma_4 \approx 0.044$ eV and $\gamma_5 \approx 0.038$ eV. In Figure 1.19 the three layer graphene lattice is shown with its band structure.

Ref. [35] has shown how the Hamiltonian of FLGs can be decomposed into subsystems similar to monolayer and bilayer graphene within an effective mass approximation. As a consequence the Hamiltonian of three layer graphene gives rise to six bands: two linear (thus similar to the monolayer case) and two couples of parabolic bands (similar to bilayer graphene) each characterized by a different effective mass.

This has been derived in a first approximation, by considering only γ_0 and γ_1 different from zero and only Bernal stacking. Such method can be applied to FLG

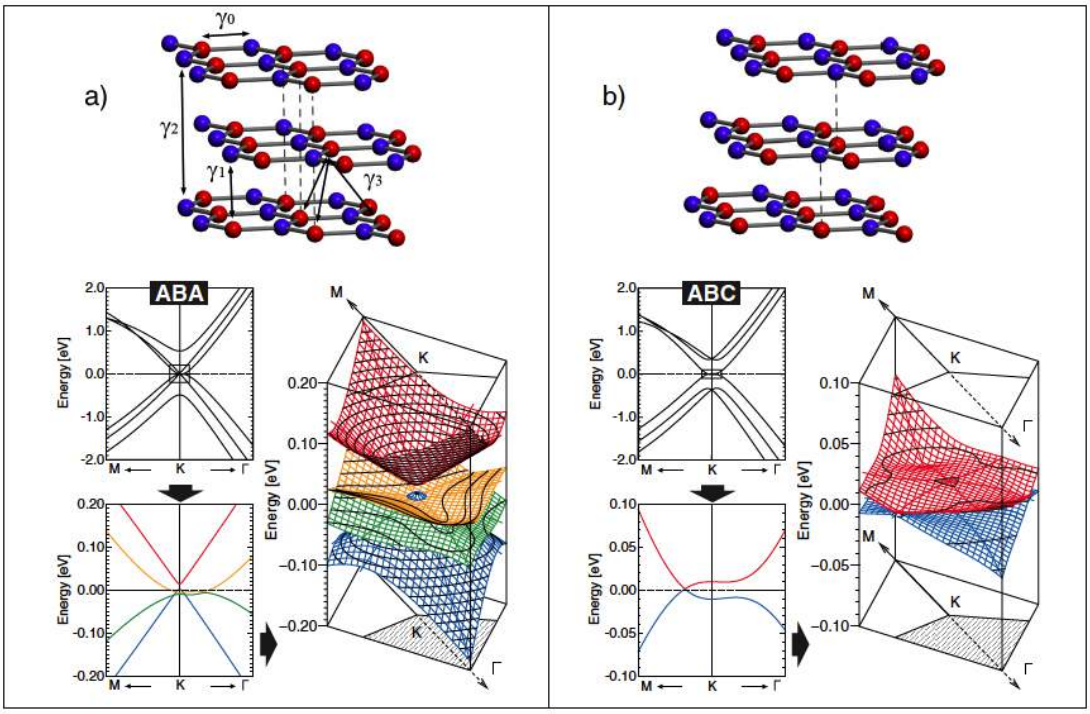

Figure 1.19. Lattice and band structure of three layer graphene a) *Bernal* stack presents crossing of bands along high-symmetry axes and for any point around K creating a domain of coexistence of electrons (orange) and holes (blue); b) in ABC stack there is one contact point at KM high-symmetry axis. (DFT calculations for both stackings) (adapted from [33])

making the derivation of its band-structure very simple, a useful tool especially for the interpretation of the optical properties of these materials. In Figure 1.20 the representation of the band-structure of FLG up to 6 layers is shown.

Another thing that has to be taken into account when dealing with FLGs is their stacking. In Figure 1.19 the lattice structure of a graphene three layer with different stacking orders is represented. The point is that such stacking order has a huge impact on the electronic properties of the material, leading to different band-structures as represented in lower part of Figure 1.19.

The authors of Ref. [33] have investigated the electronic properties of FLG using a Density Functional Theory (DFT) code within the local density approximation (LDA) scheme. Their DFT calculations demonstrate that the electronic band dispersion near the Fermi level, and consequently the nature of the charge carriers, is highly sensitive to the number of layers and the stacking geometry while experimentally observed ambipolar transport is only possible for a FLG with a Bernal-like stacking pattern, whereas semiconducting behavior is predicted

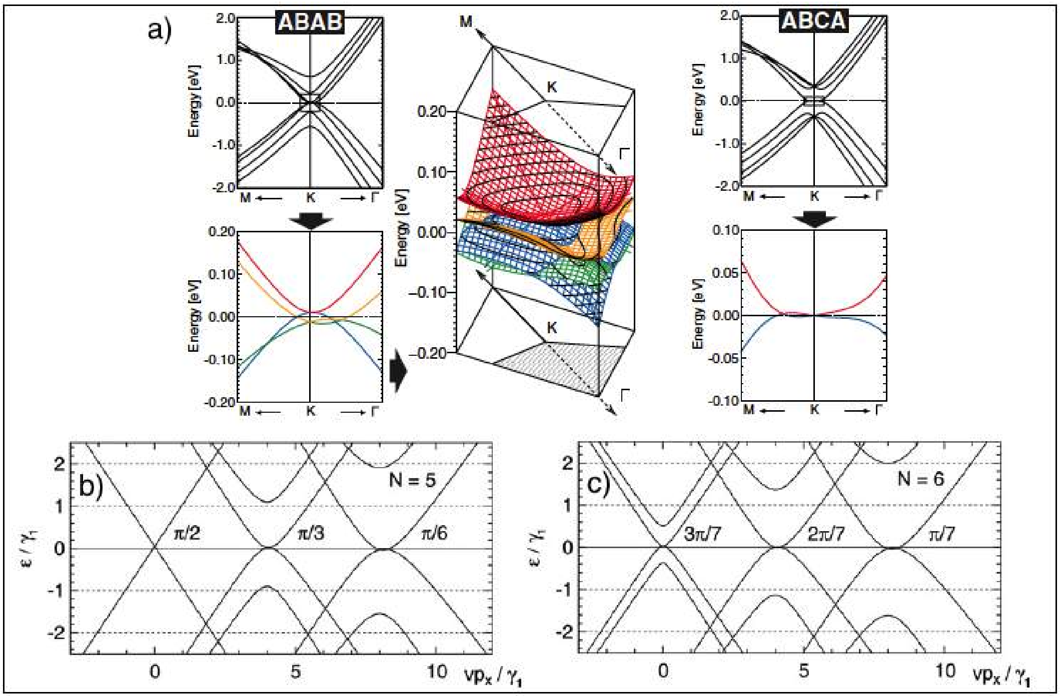

Figure 1.20. a) Band structure for four layer ABAB and ABCA stacked graphene (by DFT calculations); b) and c) are band structure of FLG, N=5 and N=6 respectively. The energy bands are shown separately for each of subsystems with a horizontal shift.(edited from [33] and [35])

for other geometries. They report the band structures of different possible FLG materials. As shown in Figure 1.18 (a) the valence band (VB) and conduction band (CB) of AB bilayer graphene admit two contact points avoiding coexistence of electrons and holes. This is because the symmetry group of AB bilayer does not contain horizontal mirror plane, hence, VB and CB can not be degenerated.

In band structure of ABC three layer graphene a single crossing point between VB and CB is located on KM axis as shown in Figure 1.19 (b). As a consequence any coexistence of charge carriers is strictly forbidden in this case.

For $ABCA$ four layer graphene the band structure is very similar to bilayer graphene: two bands join the Fermi level and allow only a few crossing points (K and one point on the KM axis). The pseudogap is 4.8 meV and net overlap between VB and CB is 2.1 meV. These band structures of rhombohedral stacked FLGs does not exhibit any measurable domain of coexistence of carriers and are only characterized by a pseudogap bounded by saddle points. For the Bernal stacking, they studied the $ABAB$ four layer graphene. Similarly to the previous case, its band structure presents crossings (Figure 1.20 (a)) allowing a net overlap between a hole band (plotted in blue) and an electron band (in orange). The overlap with the first valley is 22.6 meV, and with the second valley is 17.6 meV. An important observation is that in contrast what happens in the ABA three layer, the $ABAB$ does not have any horizontal mirror symmetry; the crossing behavior can not be explained by symmetry arguments. Therefore, the graphene structure with Bernal-like stacking (ABABA . . .) are suitable for explaining the ambipolar transport, since electrons and holes coexist in these structures, for a sufficiently wide domain of energy.

Bibliography

[1] http://en.wikipedia.org/wiki/timeline_of_carbon_nanotubes.

[2] Marc Monthioux and Vladimir L. Kuznetsov. Who should be given the credit for the discovery of carbon nanotubes? *Carbon*, 44(9):1621 - 1623, 2006.

[3] Andreoni W. The physics of fullerene-based and fullerene-related materials. *Springer*, 2000.

[4] Harold W. Kroto. Symmetry, space, stars and C_{60}. *Nobel Lecture, December* 7, 1996.

[5] Novoselov K. S., Geim A. K., Morozov S.V., Jiang D., Zhang Y., Dubonos S.V., Gregorieva I.V., and Firsov A.A. *Science*, 306(666), 2004.

[6] Wallace P. R. *Phys. Rev.*, 71(622), 1947.

[7] K. S. Novoselov, D. Jiang, F. Schedin, T. J. Booth, V. V. Khotkevich, S. V. Morozov, and A. K. Geim. Two-dimensional atomic crystals. *Proceedings of the National Academy of Sciences of the United States of A merica*, 102(30):10451-10453, 2005.

[8] Andre K. Geim and Allan H. MacDonald. Graphene: Exploring Carbon flatland. *Physics Today*, 35-40, 2007.

[9] A. H. Castro Neto, F. Guinea, N. M. R. Peres, K. S. Novoselov, and A. K. Geim. The electronic properties of graphene, *Reviews of modern physics*, 81, 2009.

[10] M. I. Katsnelson, K. S. Novoselov, and A. K. Geim. Chiral tunnelling and the Klein paradox in graphene. *Nature Physics*, 2(9):620-625, 2006.

[11] Bena C. and S. A. Kivelson. *Phys. Rev.*, B72(125432), 2005.

[12] Geim A. K. and Novoselov K. S. The rise of graphene. *Nature Materials*, 6(3):183-191, March 2007.

[13] Novoselov K. S., A. K. Geim, S. V. Morozov, D. Jiang, M.I. Katsnelson, I. V. Gregorieva, S.V. Dubonos, and A. A. Firsov. *Nature*, 438(197), 2005.

[14] Zhang Y., Y.W. Tan, H. L. Stormer, and P. Kim. *Nature*, 438, 2005.

[15] Deacon R. S., K.C. Chuang, R. J. Nicholas, K. S. Novoselov, and A. K. Geim. *Phys. Rev.*, B76(081406), 2007.

[16] N.W. Ashcroft and N.D. Mermin. *Solid state physics*. Holt, Rinehart and Winston, 1976.

[17] C. Berger et al., *Science*, 312, 1191, 2006.

[18] Novoselov K. S., Z. Jiang, Y. Zhang, S. V. Morozov, H. L. Stormer, U. Zeitler, J. C. Maan, G. S. Boebinger, P. Kim, and A. K. Geim. *Science*, 315, 2007.

[19] Klaus von Klitzing. The quantized Hall effect. *Nobel Lecture, December* 9, 1985.

[20] K. V. Klitzing, G. Dorda, and M. Pepper. New method for high-accuracy determination of the fine-structure constant based on quantized Hall resistance. *Phys. Rev. Lett.*, 45:494-497, Aug 1980.

[21] N. M. R. Peres. The transport properties of graphene: An introduction. *Reviews of modern physics*, 82, 2010.

[22] Alexander N. Obraztsov. Chemical vapour deposition: Making graphene on a large scale. *Nature Nanotechnology*, 4(4):212-213, 2009.

[23] Sukang Bae, Hyeongkeun Kim, Youngbin Lee, Xiangfan Xu, Jae-Sung Park, Yi Zheng, Jayakumar Balakrishnan, Tian Lei, Hye Ri Kim, and Young Il Song. Roll-to-roll production of 30-inch graphene films for transparent electrodes. *Nature Nanotechnology*, 5(8):574-578, 2010.

[24] J. Hass, W. A. de Heer, and E. H. Conrad. The growth and morphology of epitaxial multilayer graphene. *Journal of Physics : Condensed Matter*, 20(32):323202, 2008.

[25] Walt A. de Heer, Claire Berger, Xiaosong Wu, Mike Sprinkle, Yike Hu, Ming Ruan, Joseph A. Stroscio, Phillip N. First, Robert Haddon, Benjamin Piot, Claement Faugeras, Marek Potemski, and Jeong-Sun Moon. Epitaxial graphene electronic structure and transport. *Journal of Physics D : Applied Physics*, 43(37):374007, 2010.

[26] ScienticAmerican. http://www.scienticamerican.com/slideshow.cfm?id=diygra phene- how-to-make-carbon-layers-with-sticky-tape, 2008.

[27] M. Bruna, Ph.D. thesis, Politecnico di Torino, 2010-2012 (unpublished).

[28] C. Miao, C. Zheng, O. Liang and Y. Xie;
Chemical Vapor Deposition of Graphene; *Physics and Applications of Graph ene – Experiments*, Dr. Sergey Mikhailov (Ed.), 2011.

[29] C. Mattevi, H. Kim, and M. Chhowalla. A review of chemical vapor deposition of graphene on copper. *J. Mater. Chem.*, 21, 33243334. 2011.

[30] X. Li, W. Cai, L. Colombo and R. S. Ruoff, *Nano Lett.*, 9,4268, 2009.

[31] Eun-Ah Kim, and A. H. Castro Neto, *Europhysics Letters*, 84, 57007, 2008.

[32] McCann E. and Fal'ko V.I. Landau-level degeneracy and quantum Hall effect in a graphite bilayer. *Phys. Rev. Lett.*, 96(086805), 2006.

[33] S. Latil and L. Henrard, Charge carriers in few-layer graphene films. *Phys. Rev. Lett.*, 97, 036803, 2006.

[34] Zhang Y., Tang T.-T., Girit C, Hao Z., Martin M.C., Zettl A., Crommie M.F., Shen Y.R., and Wang F. Direct observation of a widely tunable bandgap in

bilayer graphene. *Nature Letters*, 459, 08105, 2009.

[35] Koshino M. and Ando T. Electronic structures and optical absorption of multilayer graphenes. *Solid State Communications*, 149:1123-1127, 2009.

Chapter 2

The Electrochemical Gating

2.1 The standard electric field effect

The Field Effect Transistors (FETs) follows the principle called the electric field effect that refers to the modulation of electrical conductivity of a material under study by the application of an external electric field. The most used materials for these kind of studies (and applications) are semiconductors because it is convenient and possible to switch from low to high resistivity regimes in a time scale compatible with the carriers' velocity. In fact the current leading information and communication technology industry is based on silicon and germanium based field effect transistors.

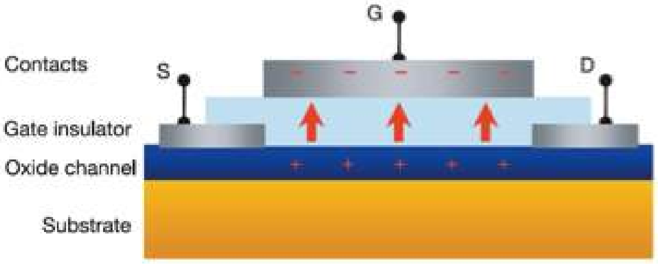

Figure 2.1. Cross-section of a typical field effect transistor with source and drain contacts on both the ends with a solid gate dielectric to control the current flow through the channel (edited from [1]).

The device configuration of FETs is based on a planar geometry and is fabricated in a simple way having an oxide layer contacted by a metallic pad. This creates a capacitor whose charge is stored on the surface of the semiconductor. These types of devices are known as Metal-Oxide-Semiconductor Field Effect Transistors (MOSFETs). On applying gate voltage from the gate pad as shown in the Figure 2.1, the current flows from the source to the drain enabled by the formation of the active/conducting channel. This technique has been extensively studied and applied to a wide variety of materials whose characteristic behavior have been investigated by altering the charge carrier densities.

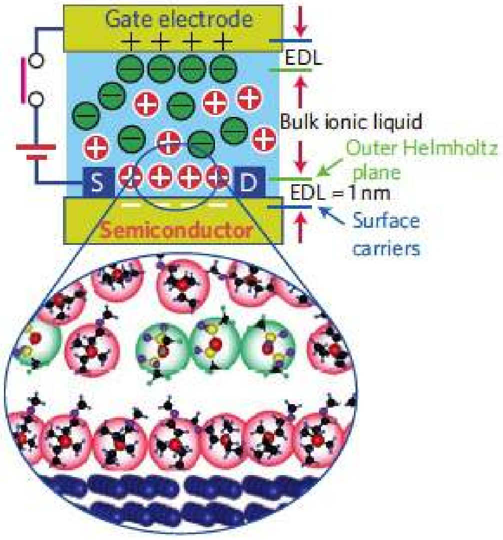

Figure 2.2. Interface between the ionic liquid and semiconductor of an EDL device. Top: schematic of charge accumulation by an EDL formed at an interface between ionic liquid and solid semiconductor. Cations (red circles) and anions (green circles) can be electrostatically accumulated onto the channel surface by applying a positive and negative gate voltage, respectively. Bottom, a magnified view of the interface between a semiconductor and an ionic liquid.[10]

But the technique of electric field effect can also enable us to study the fundamental physics of materials which could behave differently upon modification of the charge density without any change in the lattice properties. This technique has the advantage over the other techniques that no chemical doping or pressure effects are introduced, which could be permanent. The possibility to tune the charge carrier density of different materials is an important issue both in fundamental physics and in view of possible applications. For materials that have low intrinsic carrier densities, the effect of electric field shows a considerable change in the properties. Hence, they are extensively used in semiconductor industrial applications. However for other materials that have intrinsically high carrier densities, the observed effects due to electric field are minimal. The maximum electric field that can be achieved in a MOSFET device is limited by the breakdown voltage of the dielectric layer: usually it cannot exceed 10^8 V/m with a consequent induced charge density equal to $\sigma = \epsilon_0 \epsilon_r E_b$ where E_b is the breakdown electric field. As it will be shown in the next paragraphs, the efficiency of this system can be improved by the substitution of the oxide layer with an electrolyte solution. In fact by using a standard solid dielectric gating it is possible to induce a surface charge $n_{2D} \approx 10^{13}$ cm^{-2} while by using an electrolyte gating, this charge can reach values as high as $n_{2D} = 10^{14} - 10^{15}$ cm^{-2} and more (depending on the material of the active channel) as a consequence of electric fields of the order of $30 - 100$ MV/cm.

2.2 Field effect by polymer electrolyte solution: The electrochemical gating technique

In order to modify the surface properties of the materials, one of the necessary requirements is to induce a high surface carrier density by overcoming the limitations posed by the standard FETs. Thus to overcome the limit of the dielectric breakdown and increase the accumulated sheet carrier density by few orders of magnitude becomes a primary prerequisite. The breakthrough which are able to exceed these limitations comes from electrochemistry.

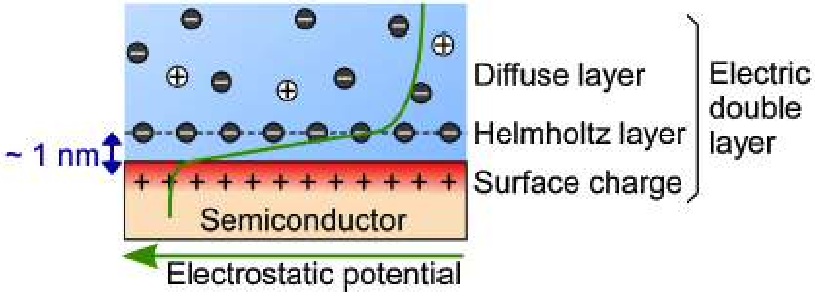

Figure 2.3. The Stern model of an electric double layer. The circled plus and minus signs correspond to cations and anions in an electrolyte, respectively. The curve illustrates electrostatic potential drop at the interface.[34]

Basically an electrochemical cell is incorporated in the FET architecture [31] (Figure 2.2). When a voltage is applied between two electrodes immersed in an electrolyte solution, positive and negative ions present in the electrolyte solution are driven by electric potential towards the oppositely charged electrodes. This electric double layer (EDL) formed at the interface accumulates high-density charge carriers that are sometimes sufficient to even induce superconductivity [32]. These kinds of devices are collectively known as an EDL capacitor. (Figure 2.3)

The EDL is formed at both the interfaces between the channel and the PES and the gate pad and the PES. If the applied gate voltage is not high enough to induce an electrochemical reaction at the interface, then the ions are aligned on the

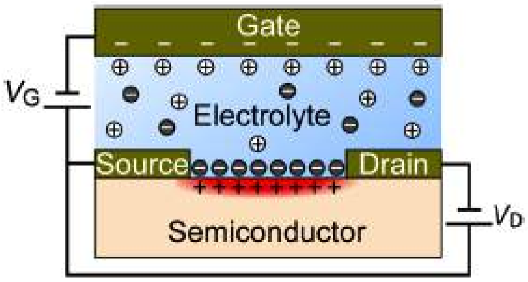

Figure 2.4. Schematic of an electric double layer field effect device. V_G and V_D denote gate voltage and drain voltage, respectively.[34]

surface of the electrodes. These dynamically accumulated charges remain confined at the surface by the applied electrostatic potential and form a two dimensional electron gas.

The ions at the electrolyte's side and electronic charges at the electrode face each other and the approximate distance of this confined capacitor is about 1 nm or less. A magnified view of the electrolyte and the electrodes when the electronic charges are induced (during EDL formation), is schematically shown in Figure 2.4. This idea was originally conceptualized by Von Helmholtz in 1853, also referred to as the Helmholtz layer.

A significant advantage of using this technique is that most of the applied voltage drop occurs within the EDL and thus the electric field produced at the interface is extremely large ($>$ 10 MV/cm or 1 V/nm). As the thickness of the EDL is of the order of a nanometer, the magnitude of capacitance developed by regarding the two parallel plates of the double layer as a capacitor can be large i.e., of the order of 10 μ F/cm^2. We refer to these devices as field effect devices (FEDs) and an advantage of these FEDs are that the operation voltage is reduced (because of its extremely large capacitance).

2.3 Field effect in metals

Metals intrinsically have high charge-density and due to this reason, field induced modulation effects are not pronounced. This fact diminishes their use for a direct contribution to technological or industrial applications. However, since the 1960s there have been a lot of fundamental scientific study. These studies tell us that minimal charge modulation effects are possible in metals because the electronic screening length (represented by Thomas-Fermi length) is smaller or of the order of one atomic diameter. Because of this the charge induction layer is expected to be confined in the surface zone of the metallic film which is smaller than the first atomic layer, making the field effect phenomenon almost unobservable even in a few nanometers of thin films. Initial experiments carried out on different materials showed differences in materials response behaving differently under the electric field effect. For instance, an increased conductivity on applying negative gate voltage was observed in gold which is compatible to an increase in electron density of gold.

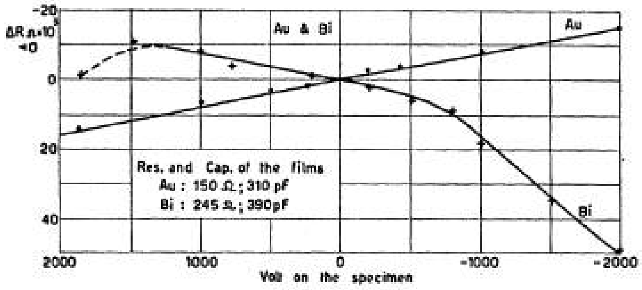

Figure 2.5. Resistance variation in gold and bismuth as a function of gate voltage.[3]

For the specific case of gold, the results presented in Ref. [3, 4] have been ascribed to conductance obtained by taking into account both the electronic density and mobility given by the equation for the film conductance as follows:

$$G = \frac{we}{l} \int_0^t \mu[n(x)]n(x)dx \tag{2.1}$$

where w is the width of channel, l its length, t is thickness and the x-axis is perpendicular to the film surface, giving an explicit dependance to the density of electrons n. The variation of conductance is given by the following equation:

$$\Delta G = -\frac{\Delta R}{R^2} = \frac{e}{l^2}[\mu + n\frac{d\mu}{dn}\Delta N] \tag{2.2}$$

and the ratio of above equations:

$$\frac{\Delta G}{G} = \frac{\Delta N}{N} \tag{2.3}$$

An important implication of this relationship is the direct proportionality of relative variation of conductance and ΔN, the total number of electrons added in the system by electric field effect. The additional term on the right side of equation 2.2 describes the effect of changing the carrier density on their mobility and it is compatible with a scattering time τ which depends on the density of states at the Fermi level:

$$n\frac{d\mu}{dn} = n\frac{d\mu}{dN(E_F)}[\frac{dN(E)}{dE}]_{E_F}\frac{dE_F}{dn} = -\frac{constant}{N(E_F^2)}[\frac{dN(E)}{dE}]_{E_F}\frac{dE_F}{dn} \quad (2.4)$$

If one assumes the free-electron dependence of the density of states (DOS), $N(E) \propto \sqrt{E}$, equation 2.4 can only give an inverse proportionality between mobility of electrons and their number. The authors of this work reported inconsistency of sign of this proportionality and stated the unsustainability of the description of field-effect in terms of bulk free-electron conductivity. This mismatch was also attributed to the surface effects, larger mobility of the induced charges close to metal/dielectric interface. Along with gold, results for Bismuth are also shown in Figure 2.5 which are compatible with a multivalent semimetal, with electrons and holes conduction. Bismuth was found to be much more sensitive to impurities present in the lattice. Hence free electron approximation cannot be used to predict these results.

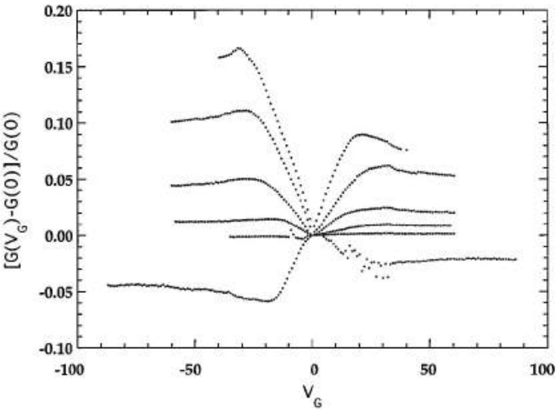

Figure 2.6. Dependence of $\Delta G/G(0)$ on V_G for a series of Pb films, with sheet resistances of 40, 25.34, 17.9, 11.31, 7.5, and 3.25 $k\Omega$. The top curve shows the most resistive film, with sheet resistances decreasing for each subsequent curve.[5]

Then an experimental study of field effect in films of pure elements like Bi, Pb was carried out with the aim to investigate the superconductor-insulator transition driven by the effect of changing film thickness and to test the predictions of theoretical model based on order parameter phase fluctuations [5]. Experiments were carried out on thin films of Bi and Pb, so that their properties traversed the insulator-to-superconductor transition. An increase in conductance as a function of gate voltage of either polarity was observed in non-superconducting Pb films. The amplitude of the effect was seen to decrease on increasing temperature, and on increasing the film thickness (Figure 2.6). In films just thick enough to become superconducting, the effect was almost vanishing and, surprisingly, it changed sign and increased again going through the superconductor-to-insulator transition. Some evidences of a glassy behavior in non-superconducting films were also reported and different possible explanations were given by asserting the fact that the addition of charge of either sign will drive the film out of equilibrium. Later, these findings were explained in terms of the underlying a-*Ge* layer rather than to the intrinsic material property of the metallic film [6].

Following these field effect experiments by solid dielectric gating on metals, we repeated these measurements by gating metallic films with a PES of special composition. This technique allowed us to induce a high amount of charge and observe its pronounced effects. The charge induced was measured by a classic method of electrochemistry called the double-step chronocoulometry as described in details in [7, 8] and briefly in the next chapter. The device preparation and processing is also described later and in Ref. [7]. Four-wire resistance measurements of metallic thin films of *Cu*, *Ag* and *Au* were made by inverting the current in each measurement to eliminate the possible thermoelectric contributions of the resistance as well as to avoid the leakage current of the gate. Resistance has been calculated as:

$$R = (V_+ - V_-)/2I \tag{2.5}$$

where $V_\pm$ are the voltage drops for forward and backward currents.

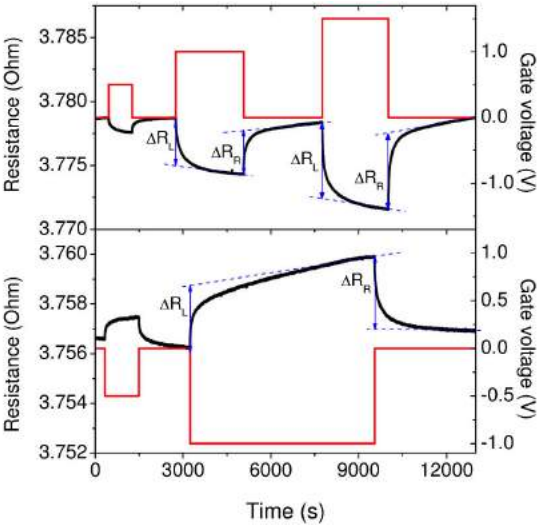

Figure 2.7. Typical response of the film resistance to positive and negative gate voltages.[6]

The thin film resistance is simultaneously measured with the application of gate voltage. As a step bias is applied the corresponding resistance variation is seen in the Figure 2.7 due to charge induction at the surface of the thin film as measured by double step chronocoulometry. The resistance variation for each gate voltage is calculated as follows:

$$\Delta R = [R(V_G) - R_0] \tag{2.6}$$

where $R_0 = R(V_G = 0)$. This value of ΔR is obtained by averaging the two values of resistivity shift, one during the voltage application and the other during the voltage removal, referred to as ΔR_L and ΔR_R in Figure 2.7.

We made a detailed study of how the charge induced is distributed at the PES-metal interface. The technique of double-step chronocoulometry is powerful to extract the value of the induced charge just stored at the interface from the total charge present in the system. At the PES-metal interface, this charge interacts with the material under field-effect and increases its bulk charge density $n_{3D}(z)$ over a certain depth from the interface along z that is perpendicular to the surface. Actually it is important to separate the amount of charge stored inside the perturbed layer from that of the unperturbed one. In the case of metallic thin films and within a simplified semiclassical model, it is possible to approximate $n_{3D}(z)$ with a step function whose depth is equal to the electronic screening length ξ. Here, the induced charge is supposed to be distributed uniformly within this volume of thickness ξ and the volumic charge density is simply given by:

$$n_{3D} = n_{2D}/\xi, \tag{2.7}$$

where n_{2D} is the output of the chronocoulometry measurement of the 2D induced charge.

In this scenario, the charge is induced over the film and the system behaves as a parallel of two resistors: first one is the resistance of the bulk proportional to $1/n_{3D}t$ where t is the thickness of the film and the second is the resistance of the perturbed region proportional to $1/n_{3D}\xi$ which becomes $1/n_{2D}$ since the volume charge density of the perturbed region is equal to n_{2D}/ξ. Thus the resistance of the film when gated by PES becomes:

$$R(V_G) = \frac{1}{n_{2D} + n_{3D}t} \tag{2.8}$$

Hence, our quantity of interest, the relative resistance variation that occurs during gate voltage application is expressed to be:

$$\frac{\Delta R}{R'} = \frac{R(V_G) - R_0}{R(V_G)} = -\frac{n_{2D}}{n_{3D}t} \tag{2.9}$$

In this equation, $\Delta R/R'$ depends only on the total thickness of the film: the dependence on the material is expressed by n_{3D} while n_{2D} is the extra charge induced by field effect.

Since each device for the different metal (Au, Ag and Cu) has been prepared differently with respect to different suitable substrates, film thickness and production, each device had peculiar features. For each material, it was possible to relate the value of the induced charge with the value of resistance shift of the film [**?**].

In order to provide a complete description of field effect in metallic films, a precise measurement of the following parameters were carried out: induced charge, resistance variation and film thickness. In Figure 2.8 the relative variation of resistance versus the induced charge n_{2D} is reported. The inset shows a zoom of the yellow rectangle for the data of gold thin films.

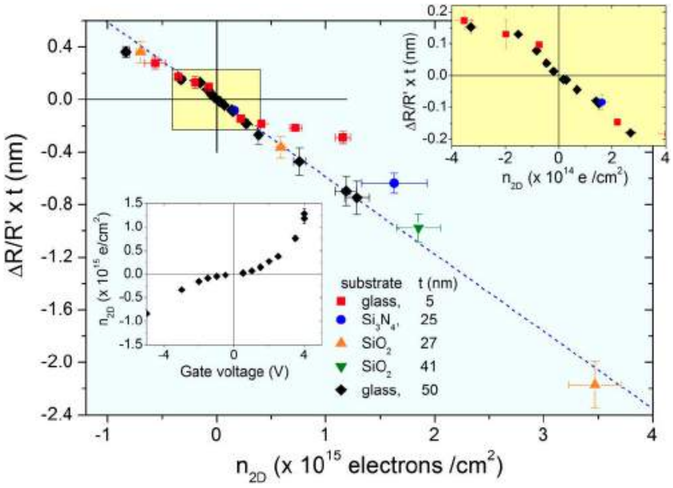

Figure 2.8. Dependence of $(\Delta R/R').t$ on n_{2D} (i.e., number of electrons per cm^2) as obtained for various films with different thickness and on different substrates, indicated in the legend. The upper inset shows a zoom around the origin of the axes. The lower inset shows the dependence of n_{2D} on the gate voltage, for the 50 nm-thick Au film.[10]

A careful and precise study was necessary in order to estimate the thickness of the film under consideration. The resistivity of the sample can be represented by equation:

$$\rho = R\frac{wt^*}{l} \tag{2.10}$$

where R is the measured resistance, w is the width, l is the length and t^* is the equivalent thickness of the sample. This last quantity takes into account the inhomogenity of the film and is lower than its geometrical thickness. The quantity wt^* is the effective area of the cross section of the sample that carries electrical current and accounts for the voids in the polycrystalline structure if the film

We can introduce the quantity F that gives a relationship between the geometrical and equivalent cross section and is always positive and equal to one if the sample is as uniform as a single crystal. Details on how to evaluate the reduced area are mentioned in Ref. [7, 6].

$$F = \frac{wt}{wt^*} \tag{2.11}$$

The resistivity was measured experimentally between 300 K and 3 K and the induced charge by double step chronocoulometry. We report the results in Figure 2.8 and 2.9 for different metals. The same series of measurements were performed in silver and copper thin films and the data are reported in Figure 2.9. According to equation 2.9 $(\Delta R/R').t$ and n_{2D} exhibit a linear relationship with a negative slope expressed by $1/n_{3D}$.

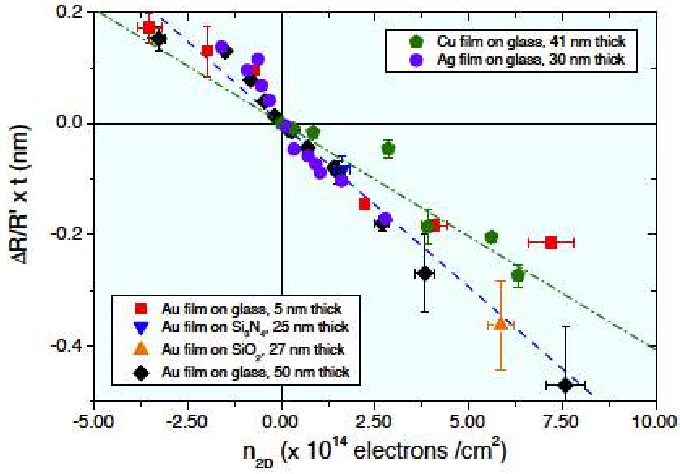

Figure 2.9. Dependence of $(\Delta R/R').t$ on n_{2D} as obtained for films of different metals (Au, Ag, Cu) with different thickness and on different substrates.[10]

From Figure 2.9 it appears clear that the series of data for Au and Ag lie on a line with different slope with respect to Cu. This is due to the fact that the values of the bulk charge density n_{3D} are equal to 5.90×10^{22} cm^{-3} for Au and 5.86×10^{22} cm^{-3} for Ag in the framework of free-electron model. These values are higher if compared to Cu where n_{3D} is 8.47×10^{22} cm^{-3}. Note that the values of the relative resistance variation, $(\Delta R/R')$ for 5 nm thick films (red squares in Figure 2.8 and 2.9), is found to be lower and it deviates from the linear fit for induced charges greater than 2×10^{14} cm^{-2} in similar conditions. This could possibly be explained due to rise of multiple scattering at the surface of the metallic film, however to confirm this interpretation it is necessary to measure electrons' mean free path in the thin films. But in this case the free electron model (equation 2.9) could not be appropriate to describe the physics of such a thin system because it neglects the probability of surface scattering phenomena.

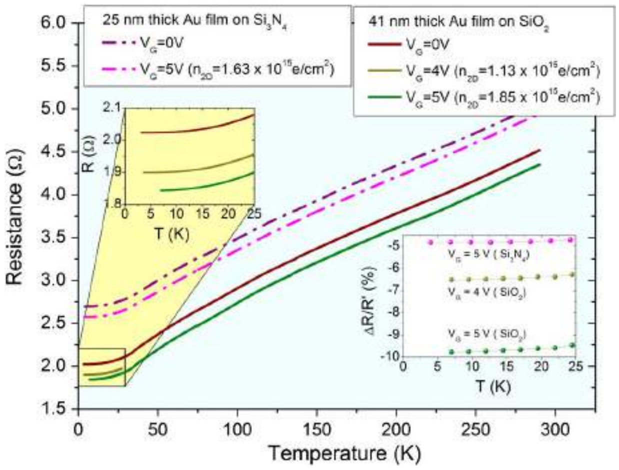

Figure 2.10. Temperature dependence of the resistance of two *Au* films for different values of the gate voltage. The corresponding values of n_{2D}, measured at room temperature, are indicated in the legend. Upper inset: zoom of the low temperature region. Lower inset: relative resistance variation $\Delta R/R'$ at low temperatures, extracted from the curves in the main panel.[6]

To observe the effects and confirm that the shift in resistance is actually due to the formation of an electrical double layer (EDL) at the interface, some measurements were performed at cryogenic temperatures. Also through this, it was verified that the leakage current through the gate does not contribute to any change in film's resistance. When the polymer goes down in temperature it freezes at ≈ 240 K (the glassy transition) thereby freezing the EDL (and the gate electric current goes to a zero value). The corresponding resistance variation, due to the gate voltage application, is referred to as ΔR. The δR with respect to temperature at different applied gate voltages is shown in Figure 2.10. In the Figure 2.10, data for 25 nm and 41 nm thick films are shown, for n_{2D} values measured by chronocoulometry at different applied gate voltages. A remarkable point of these measurements is the value of the relative resistance shift ($\Delta R/R'$), observed at cryogenic temperatures, that reaches a value 10% higher for a gate voltage application of 5 V, as shown in the inset of Figure 2.10.

It is clear through this discussion that the limit of standard solid back gate devices, $n_{2D} = 10^{13}$ cm^{-2} corresponding to the case of suspended silicon nitride membranes, is successfully overcome by polymer gating thereby inducing a record of surface charge, more than $n_{2D} = 4 \times 10^{15}$ cm^{-2} using the PES.

Then it was interesting to explore how much charge can be induced in the different metals studied and how it depends on the sequence of voltage applications.

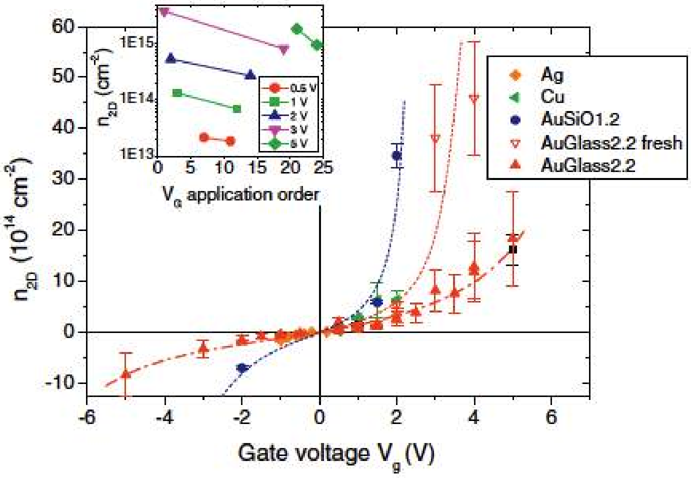

Figure 2.11. Induced surface charge density n_{2D} as function of the gate voltage V_G for different devices made of different metals (Au, Ag, Cu). Although most of the points are gathered around a common trend, some data show much higher values of the surface charge density. In the inset the dependence of n_{2D} on the sequence of application of V_G is shown.[6]

The results are reported in Figure 2.11 showing the surface charge density n_{2D} with respect to gate voltage. It seems an incongruity that the same surface charge density is obtained on gold for different gate voltages (between 1.5 and 3 V, for example) or even a lower induction is obtained for higher voltages. A simple explanation of this behavior comes from the inset of Figure 2.11 where it is shown that for any gate voltage, charge induction is maximum on the first time application and systematically decreases at the increase of the number of applications. Since the PES is very stable over long times, this behavior might be rather ascribed to a sort of memory effect and this effect is compatible with a possible loss of Li ions at the interface with the electrodes that limits the magnitude of the EDL and consequently the performances of the field-effect device.

2.4 Field effect in carbon based materials

2.4.1 Field effect in single and few layer graphene

Almost a revolution was initiated by an article published in October 2004 [11], when condensed matter physicists reported that they had prepared graphene i.e., two-dimensional sheets of carbon atoms and observed the ambipolar electric field effect in their samples. Since then, major chip-makers are active in graphene research and the International Technology Roadmap for Semiconductors, the strategic planning document for the semiconductor industry, considers graphene to be among the candidate materials for post-silicon electronics [12]. Graphene is potentially well suited for this purpose because of its promising carrier transport properties and its purely two-dimensional structure. With the possibility of having channels just one atomic layer thick, graphene is the most attractive material for its use in transistors. It may be possible to make devices with channels that are extremely thin. This fact will allow graphene field-effect transistors to be scaled to shorter channel lengths and higher speeds without encountering the adverse short channel effects that restrict the performance of existing devices.

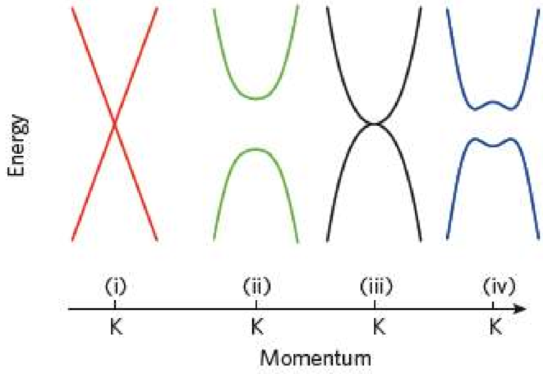

Figure 2.12. Band structure around the K point of (i) large-area graphene, (ii) graphene nanoribbons, (iii) unbiased bilayer graphene, and (iv) bilayer graphene with an applied perpendicular field. Large-area graphene and unbiased bilayer graphene do not have a bandgap, which makes them less useful for digital electronics.[12]

As described earlier, because of the zero bandgap, devices with channels made of large-area graphene cannot be switched off and therefore are not suitable for logic applications. However, the band structure of graphene can be modified, and it is possible to open a bandgap in three ways: by constraining large-area graphene in one dimension to form graphene nanoribbons, by biasing bilayer graphene and by applying strain to graphene (as shown in Figure 2.12).

In the first, seminal article of 2004 [11] the solid-dielectric field-effect measurements were explained quantitatively by a model of a 2D metal with a small overlap between conductance and valence bands. The gate voltage induces a surface charge density $n = \epsilon_0 \epsilon V_G / te$ and, accordingly, shifts the position of the Fermi energy ϵ_F. Here, ϵ_0 and ϵ are the permittivities of free space and SiO_2, respectively; e is the electron charge; and t is the thickness of our SiO_2 layer (300 nm). For typical

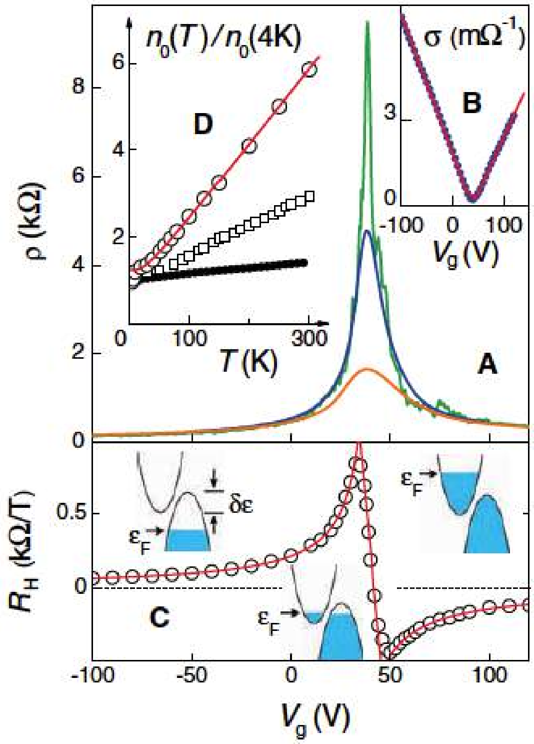

Figure 2.13. Field effect in FLG. (A) Typical dependences of FLG's resistivity ρ on V_G for different temperatures ($T = 5,\ 70\ and\ 300\ K$ from top to bottom curves, respectively). (B) Example of changes in the film's conductivity $\sigma = 1/\rho(V_G)$ obtained by inverting the 70 K curve (dots). (C) Hall coefficient R_H versus V_G for the same film; $T = 5K$. (D) Temperature dependence of carrier concentration n_0 in the mixed state for the film in (A) (open circles), a thicker FLG film (squares), and FLG ($d \approx 5nm$; solid circles). Red curves in (B) to (D) are the dependences calculated from the model of a 2D semimetal illustrated by insets in (C).[11]

$V_G = 100$ V, the formula yields $n \approx 7.2 \times 10^{12}$ cm^{-2}. The electric field doping transforms the shallow-overlap semimetal into either completely electron or completely hole conductor through a mixed state where both electrons and holes are present (Figure 2.13). The three regions of electric field doping are clearly seen on both experimental and theoretical curves. For the regions with only electrons or holes left, R_H decreases with increasing carrier concentration in the usual way, as $1/ne$. The resistivity also follows the standard dependence $\rho^{-1} = \sigma = ne\mu$ (where σ is carrier mobility). In the mixed state, σ changes little with V_G, indicating the substitution of one type of carrier with another, while the Hall coefficient reverses its sign, reflecting the fact that R_H is proportional to the difference between electron and hole concentrations.

To open a band gap useful for conventional field-effect devices, very narrow with well-defined edge channels are needed which represents a serious challenge. In general, the larger the band gap that opens, the more the valence and conduction bands become parabolic (rather than cone-shaped): this decreases the curvature around the K point and increases the effective mass of the charge carriers, which is likely to decrease the mobility.

Bilayer graphene is also gapless (Figure 2.12), and its valence and conduction bands have a parabolic shape near the K point. If an electric field is applied perpendicular to the bilayer, a bandgap opens and the bands near the K point take on the so-called Mexican-hat shape. This opening was predicted by theory [13, 14] and has been verified in experiments [15, 16]. Theoretical investigations have also shown that the size of the band gap depends on the strength of the perpendicular field and can reach values of $200 - 250$ meV for high fields $1 - 3 \times 10^7$ V cm^{-1}.

The most frequently stated advantage of graphene is its high carrier mobility at room temperature. Mobilities of 10,000 - 15,000 cm^{2}V^{-1}s^{-1} are routinely measured for exfoliated graphene on SiO_2-covered silicon wafers and upper limits between 40,000 and 70,000 cm^{2}V^{-1}s^{-1} have been suggested. Moreover, in the absence of charged impurities and ripples, mobilities of 200,000 cm^{2}V^{-1}s^{-1} have been predicted, and a mobility of 10^6 cm^{2}V^{-1}s^{-1} was recently reported for suspended graphene. For large-area graphene grown on nickel and transferred to a substrate, mobilities greater than 3,700 cm^{2}V^{-1}s^{-1} have been measured. It is worth noting that reported mobilities for graphene devices need to be interpreted carefully because there are several definitions for the MOSFET channel mobility and they are difficult to compare [12].

For graphene, maximum carrier velocities of about 4×10^7 cm s^{-1} are predicted, in comparison with 2×10^7 cm s^{-1} for $GaAs$ and 10^7 cm s^{-1} for silicon. Moreover, at high fields the velocity in graphene does not drop as drastically as in the III-V semiconductors. Unfortunately, there is at present no experimental data available on high-field transport in graphene nanoribbons and in large-area graphene. However, other measurements suggest high-field carrier velocities of several 10^7 cm s^{-1} in graphene. Thus, regarding high-field transport, graphene seem to have a slight advantage over conventional semiconductors.

Furthermore, the techniques used to measure mobility are only vaguely described in some articles. Most frequently, the field-effect mobility, μ_{FE}, is measured as follows:

$$\mu_{FE} = \frac{L_{ch} g_m}{W_{ch} C_G V_{DS}} \tag{2.12}$$

where g_m is intrinsic transconductance, V_{DS} is terminal d.c. voltage, L_{ch} and W_{ch} are channel length and width, C_G is gate capacitance.

In the particular graphene MOSFET device reported by the Manchester group in 2004 [11] the 300 nm SiO_2 layer underneath the graphene served as a back-gate dielectric and a doped silicon substrate acted as the back-gate. Such back gate devices have been very useful for proof-of-concept purposes, but they suffer from unacceptably large parasitic capacitances and cannot be integrated with other components. Therefore, practical graphene transistors need a top-gate. The first graphene MOSFET with a top-gate was reported in 2007 [17], representing an important milestone, and progress has been very rapid since then. The channel mobilities exceeding 20,000 $cm^2V^{-1}s^{-1}$ in top-gated graphene MOSFETs are reported [18].

However, this progress has been accompanied by the appearance of a number of problems. MOSFETs with large-area graphene channels cannot be switched off, making them unsuitable for logic applications, and their peculiar saturation behavior limits their radio frequency performance. Additional complications arise in the interpretation of the overall gate capacitance, frequently approximated to oxide capacitance per unit area. In the case when the thickness of the oxide is small, quantum capacitance must be taken into account (discussed in details in the next chapter).

The primary challenges faced by the scientific community at present, therefore, are to create in a controlled and practical fashion a band gap in graphene, which would allow logic transistors to switch off and radio frequency transistors to operate and to develop other means of improving transistor saturation characteristics by, for example, realizing contacts that block one kind of carrier without degrading the transistor's speed. Also the use of graphene in transistors stems less from ultrahigh mobilities than from graphene's ability to scale to short gate lengths and high speeds by virtue of its thinness.

Considering the high values of parameters and to overcome the shortcomings, scientific community around the world has been highly motivated to carry out the research. Up to now, the investigation of transport properties through graphene layers has been focussed almost exclusively on the low carrier density regime ($n \approx 10^{12}$ cm^{-2}) due to the limited amount of carrier density accessible in conventional MOSFETs. More recently the high carrier density regime (n $\approx 10^{14}$ cm^{-2}) has been explored [7, 10]. This range of high surface carrier densities that can be induced by polymer or liquid gating EDL techniques could prove some exciting theoretical predictions (possible occurrence of superconductivity [21, 22]) and has also relevance for technological applications (transparent electrodes for flat panel displays [23], supercapacitors [24] and biosensors[25]).

With the recent development of EDL devices (discussed in the earlier part of this chapter) and the application to FLG systems, a considerable advancement has been obtained [7, 10]. By applying a gate voltage (up to several volts) the voltage itself is made to mainly drop across the interface leading to a very large geometrical capacitance in the approximately 1 nm thick EDL. As a result, the induced carrier density can easily exceed $n_{2D} \approx 10^{14}$ cm^{-2}, more than one order of magnitude larger than that in conventional solid-state FETs (Figure 2.2).

Ref. [7] has performed a comparative study of transport in ion-gated single-, bi-, and tri-layer graphene by inducing high carrier density of approximately 10^{14} cm^{-2}. They report that when the surface carrier densities, n_{2D} exceed 10^{13} cm^{-2}, the higher-energy split-off bands start to be populated and this opening of parallel transport channels affects the conductivity, σ_{2D} of these systems (Figure 2.14). For a single-layer graphene, a linear increase of σ_{2D} was observed upon accumulating either electrons or holes within a gate voltage $\Delta V \approx \pm 1$ V from the charge neutrality point.

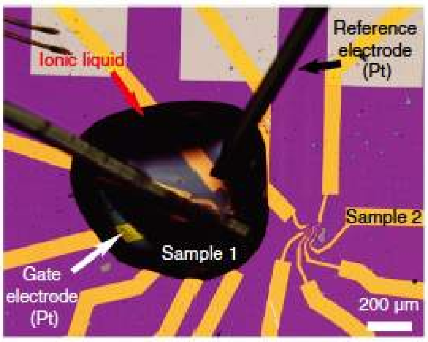

Figure 2.14. Optical microscope image of an actual device. Two separate graphene flakes are seen on the substrate, but only one of them is immersed in the ionic liquid with two Pt wires immersed in the ionic liquid, acting as gate and quasi-reference electrodes.[7]

On further increasing the voltage range, σ_{2D} exhibits a pronounced saturation. However, for a bilayer and three layer graphene the linear increase of σ_{2D} appears within a narrow range of $\Delta V \approx \pm 0.5$ V near the charge neutrality point followed by a nonmonotonic behavior at higher V_G as shown in the Figure 2.15 A-C. Using the carrier density determined from Hall measurements, the mobilities were directly determined with maximum values of 5.5, 3.5 and 9×10^3 cm^{2}V^{-1}s^{-1} close to the neutrality point, for single-, bi-, and three-layer graphene, respectively as shown in the Figure 2.15 D-F. The same Figure 2.15 shows the total capacitance that was determined as:

$$C = e\frac{dn_{2D}}{dV_G} \tag{2.13}$$

The data shows a strong asymmetry between electrons and holes but as it is known electron-hole symmetry holds approximately in graphene on the studied energy scale, these particular observed asymmetries are attributed to the properties

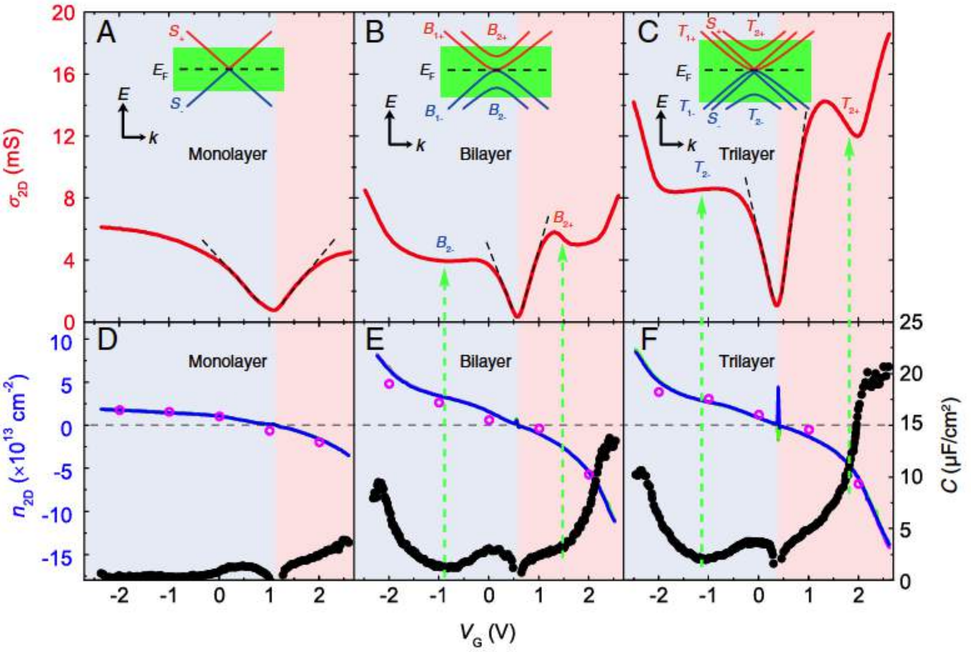

Figure 2.15. (A-C) The conductivity σ_{2D} of single-, bi-, and tri-layer graphene, respectively, as a function of applied V_G, using ABIM-TFSI ionic liquid gate. (D-F) Hall effect measurements of the carrier density, n_{2D}. Three curves (overlapped) measured by fixing magnetic field while scanning V_G and the pink dots measured by fixing V_G while scanning the magnetic field show consistent data. D-F also show the capacitance, C of the layers, obtained by differentiating the accumulated n_{2D} with respect to V_G. The insets of A-C illustrates main aspects of the band structure of single-, bi-, and three-layer graphene, respectively and green shaded areas illustrates range within which the Fermi level can be shifted in the three cases.[7]

of the EDLs only. In reality they originate from the different size of positive and negative ions forming the ionic liquid (i.e., 1-allyl-3-butylimidazolium bis-(trifluoromethanesulfonyl)-imide (ABIM-TFSI)) responsible for different thickness of EDLs for opposite polarities of the gate voltage. The capacitance seems to be strongly dependent on V_G and is dominated by the quantum capacitance, C_Q (discussed in details further). The dominant role of the quantum capacitance explains that the amount of carrier density accumulated in graphene with different number of layers (at the same gate voltage and using same ionic liquid) differs, as a direct consequence of the different density of states in graphene layers of different thickness.

The insets of Figure 2.15 A-C illustrate the main features of the band structures of graphene single-, bi-, and tri-layer. As we have already shown in the first chapter, in SLG only two (valence and conduction) linearly dispersing bands S2 touching at zero energy and in bi- and tri-layer graphenes additional bands at higher energy are present. The first of these bands starts at around 0.4 (B2) and 0.5 $\sim$ 0.6 eV (T2) from the charge neutrality point, for bi- and three-layer, respectively. Filling of these bands is expected to occur when the carrier density approximately exceeds 2 and 7×10^{13} cm^{-2} in these two cases. The "anomalies" (i.e., the non-monotonic behavior) in the conductivity occur at density values (larger for three layer than for bilayer) close to the ones estimated above. The anomaly in conductivity is attributed to the presence of an additional scattering channel - inter band scattering - that opens when the higher bands are filled, and that, as it is known from conventional semiconductors, can strongly reduce the carrier mobility. In contrast, no anomaly is seen in the monolayer, because no higher-energy band is present in its band structure in a reasonably low energy scale.

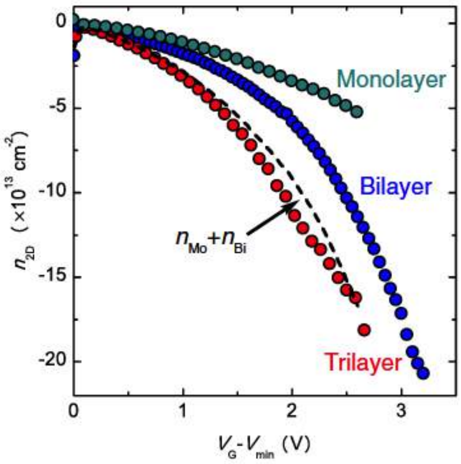

Figure 2.16. The dependence of carrier density n_{2D} on gate voltage V_G (measured from the charge neutrality point) for single-, bi-, and three-layer graphene devices, using DEME-TSFI as ionic liquid. The dashed black line is the sum of n_{2D} of single- and bi-layer graphene, which compares well to the n_{2D} measured in the three layer. This relationship is approximately expected from the known band structure of these materials, because the two lowest energy bands of three layer roughly correspond to the lowest energy band of single- and bi-layer graphene.[7]

Finally they report in Figure 2.16 the relation between n_{2D} and V_G for single-, bi-, and three layer graphene devices, from which it is found that the carrier density for the three layer closely matches the sum of the densities in single- and bi-layer. Such a relation is expected to approximately hold from the theoretical band structure of these systems, because the two lowest energy bands in three layer correspond approximately to the linear band of single layer and the lowest energy quadratic band of bilayer.

Another study of SLG was reported by Ref. [26]. They gated the graphene devices by PES (a different composition than ours), made by an aqueous dispersion of polyethylene oxide (PEO) and lithium perchlorate. The devices were patterned in the standard Hall configuration as shown in Figure 2.17 (top left) and later a drop of PES was casted (bottom left).

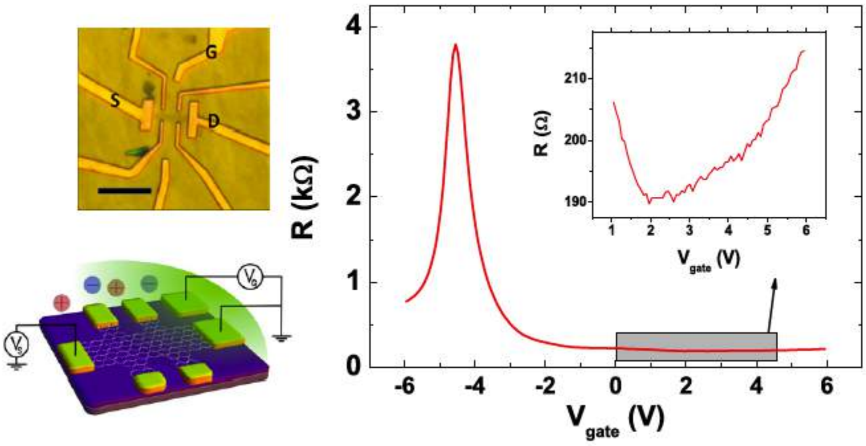

Figure 2.17. Optical image (top) and schematic of graphene device (bottom) in Hall-bar configuration, coated with PES. Here, S=Source, D=Drain, G=Polymer electrolyte gate. Scale bar: 10 μm. Resistance vs polymer gate voltage (right) (inset: R vs. V_G in the low-resistance region, showing an upturn in the device resistance).[26]

In the same Figure 2.17 (right), a plot shows the modulation of graphene's resistivity with applied gate voltage through PES at room temperature. They obtained a large and reversible modulation in graphene's resistance with small applied voltages due to large interfacial capacitance arising from a nearby layer of counter ions (same as EDL). However, the measurements are restricted to a maximum gate leakage of ~ 1 nA. At high gate voltages (or gate leakage currents) the devices showed a breakdown due to electrochemical reactions. Since the polymer is hygroscopic, the presence of adsorbed residual water contributed importantly to this leak, but at the same time allows a better ionic mobility. The typical mobility of pristine graphene samples they obtained at low doping was in the range $4000 - 7000\ \mathrm{cm}^2\mathrm{V}^{-1}s^{-1}$. Upon addition of the polymer electrolyte, the mobility of graphene remained larger than 3000 $\mathrm{cm}^2\mathrm{V}^{-1}\mathrm{s}^{-1}$ at $\mathrm{n} \sim 10^{13}\ \mathrm{cm}^{-2}$.

Without any gate voltage, graphene was found to be in a highly electron-doped low-resistance state and the charge neutrality point shifted from -3V to -5V. Such doping was attributed to a higher concentration of Li^{+} ions adsorbed in the vicinity of graphene, since graphene has small hole-doping prior to coating of the PES. The G-band Raman peak for graphene showed a shift of 6-7 cm^{-1} upon addition of the PES as well as a reduction in full-width at half-maximum (FWHM) which further supports the electron-doping of graphene. (Figure 2.18)

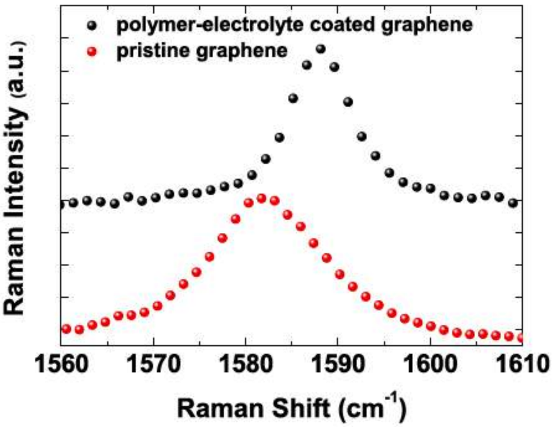

Figure 2.18. G-band Raman shift for pristine graphene and PES coated graphene.[26]

They performed the Hall measurements at room temperature and the resistivity and Hall mobility plotted as a function of the carrier density are shown in Figure 2.19 , respectively. The mobility shows a continuous decrease described by $\mu \sim 1/n$ between n = 1 × 10^{13} cm^{-2} and 6 × 10^{13} cm^{-2}, indicating that ρ approaches a saturation value.

They conclude that the total resistivity include contributions from charged impurities (from underlying substrate and electrolyte ions), defects on the graphene lattice and phonons. They report contributions to graphene resistivity by following factors:
1. Electrolyte ions present in the vicinity of graphene sheet increases with electron density. This cannot be estimated experimentally but theoretically, Poisson-Boltzmann equation could describe their distribution. Since the ion concentration estimated from this model diverges at the graphene/PES interface while its limited by finite ionic radius, space occupied by polymer and formation of electrolyte polymer complex, a modified Poisson-Boltzmann equation is considered.

With this and polymer packing density of 80% and an electrolyte ion effective radius around 1 nm, c_{max} takes values between 10^{25} m^{-3} and 5 × 10^{25} m^{-3}. The polymer dielectric constant is ∼ 5. The concentration of ions in the bulk polymer matrix is estimated to be about 5 × 10^{24} m^{-3}. The gate voltage dependence of the carrier density is plotted in Figure 2.19 (right). The slope of the linear fit of the Figure 2.19 (right) gives an estimate of the gate capacitance of the electrolyte

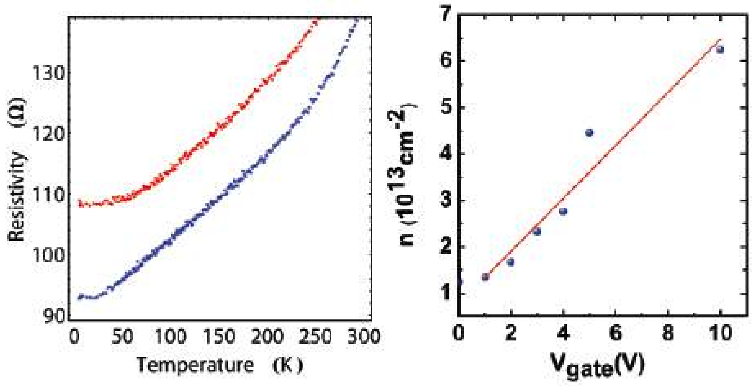

Figure 2.19. (Left) Resistivity vs temperature at two different densities n ∼ 6.2 × 10^{13} cm^{-2}(red), n ∼ 2.5 × 10^{13} cm^{-2} (blue). (Right) Carrier concentration vs applied gate voltage bias.[26]

gating, $C \approx 1$ μFcm^{-2}.

2. Influence of charged impurities from the SiO_2 substrate. This requires an estimate of the charged impurity density n_{imp} in the substrate, which can be obtained from a linear fit to the $\sigma - n$ plot at low densities prior to the addition of the polymer and they obtained an average value of $n_{imp} \sim 7 \times 10^{11}$ cm^{-2}.

3. As they discussed the electrolyte ion distribution was found almost temperature independent since the ions are practically frozen below the ice-point of water. Therefore, the phonon contribution ρ_{phonon} was extracted from the temperature dependence of the graphene resistivity at high doping. The resistivity vs temperature measurements are shown down to 4 K in Figure 2.19 (left). A Bloch-Grüneisen regime was observed between 4 K and 100 K providing a clear sign of large Fermi temperatures.

4. Another contribution was suspected to be induced by defects in the graphene lattice like strong potential defects such as vacancies and certain ad-atoms that lead to a density dependent resistivity.

Thus, they mention that the contributions to graphene's resistivity from ions, phonons and defects are either nearly constant (phonons and weak scatterers) or rapidly vanishing with density (charged scatterers and strong-potential defects). Also, they observed a consistent upturn in resistivity in a finite density window near n ∼ 3 × 10^{13} cm^{-2} (Figure 2.20). Note that at higher densities (1.6 × 10^{14} cm^{-2}), the resistivity decreases, then saturates (see inset of Figure 2.20).

The density dependence of the mobility and resistivity of their samples were analyzed by them considering various scattering mechanisms: Coulomb scattering from the electrolyte ions, electron-phonon scattering, and electron-impurity scattering. Vacancies, cracks and certain ad-atoms were found to be important

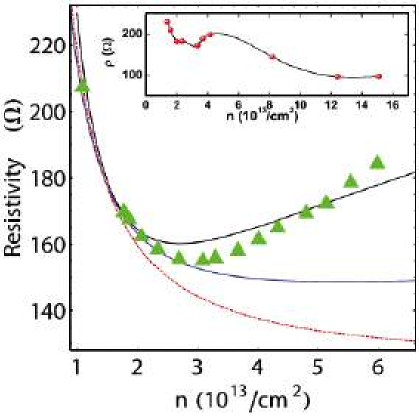

Figure 2.20. Resistivity vs carrier density (experimental data in green triangles). Best fits to resistivity without Fermi velocity renormalization (dashed red curve); with electron-electron interaction-induced renormalization (solid blue curve), by doubling the $e^- - e^-$ interaction coupling constant (solid black curve).[26]

scatterers in the low-density regime. However, weak scatterers are the most important scatterers in the range of densities (n $> 10^{13}$ cm^{-2}), as suggested by the 1/n density dependence of mobility.

Immediately after this article, the authors of Ref. [13] published their results on the related topic. They reported temperature dependent electron transport in graphene at different carrier densities. Employing similar electrolytic gate polymer, they demonstrated to be able to achieve a carrier density up to 4×10^{14} cm^{-2} for both electrons and holes.

They claimed that they could apply gate voltages V_{eg} of up to 15 V in order to avoid electrochemically induced sample degradation by immediately cooling the sample in less than 1 *minute* below 250 K. This procedure lead to a freeze of the ions that maintain the Debye layer (or EDL) on to graphene's surface. The results for the measured densities with respect to applied gate voltages are shown in Figure 2.21. They also measured $\rho(T)$ for more than ten SLG samples, in the temperature range 1.5 < T < 300 K and for $|n| < 2\times\ 10^{14}$ cm^{-2}. The measured $\rho(T)$ is shown in Figure 2.22. As can be seen from this Figure 2.22, $\rho(T)$ decreases monotonically as T decreases, saturating to ρ_0 in the low temperature limit. This residual resistance ρ_0 stems from the electron scattering on static impurities and point defects and is expected to be almost temperature independent. The resistance follows a strictly 2D Bloch-Grüneisen behavior, exhibiting a linear T to super-linear T^4 crossover, determined by the gate tunable characteristic Bloch-Grüneisen temperature Θ_{BG}. This has taken into account the quantum distribution of the two-dimensional acoustic phonons in graphene. Further they state that their quantitative analysis of the temperature dependent resistivity shows a

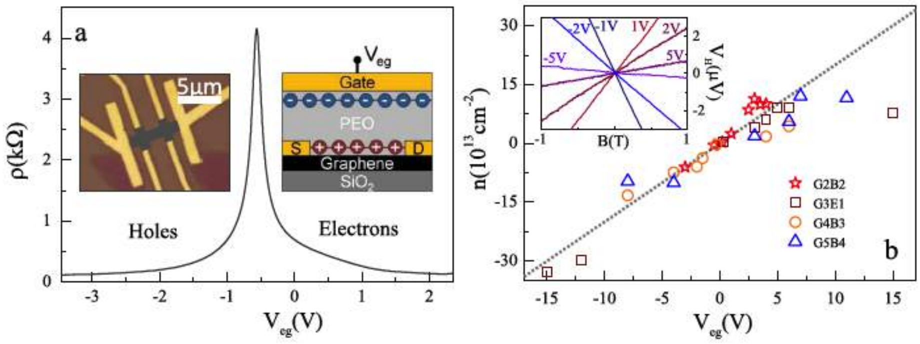

Figure 2.21. (a) Resistivity as a function of applied electrolyte gate voltage V_{eg} at T=300 K. Right inset: a schematic view of the electrolyte gated device. The Debye layers are formed d ∼ 1 nm above the graphene surface. The left inset shows an optical microscope image of a typical etched Hall bar device. (b) The inset shows the Hall voltage V_H as a function of the magnetic field B for different V_{eg}. The main panel shows the extracted densities n (by Hall measurements) as a function of V_{eg}. The slope of the line fit represents the capacitive coupling of the electrolyte gate to the graphene. (adapted from [13])

universal scaling behavior of the normalized resistivity $\rho(T)$ with the normalized temperature T/Θ_{BG}, representing the 2D nature of the electrons and phonons along with the chiral nature of the carriers in graphene.

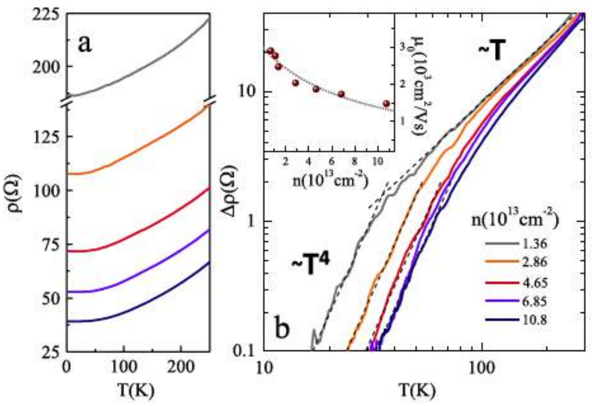

Figure 2.22. (a) Temperature dependence of the resistivity for different charge carrier densities of sample. (b) The temperature dependent part of the resistivity $\Delta(T)$ scales as T^4 in the low T range and smoothly crosses over into a linear T dependence at higher T. The dashed lines represent fits to the linear T and T^4 dependencies, respectively. The inset shows the mobility μ_0 at T=2 K as a function of the density n. The gray line is the theoretically expected mobility due to short and long range impurity scattering.[13]

Very recently, results on epitaxial three layer graphene were presented [28] investigating spin-orbit interaction (SOI) and its modulation through ultrahigh electric field generated in the so called EDL transistors.

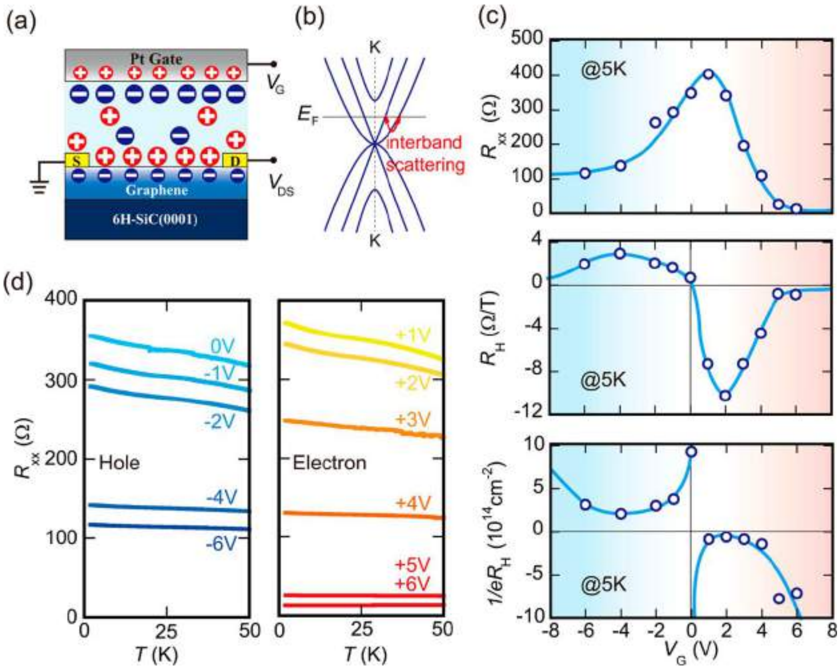

Figure 2.23. (a) Schematic diagram of EDL transistors based on epitaxial three layer graphene on 6H-SiC(0001) substrate. (b) Schematic band structure of three layer graphene at K point in the hexagonal Brillouin zone. (c) Sheet resistance R_{xx}, Hall coefficient R_H, and $1/eR_H$ value as functions of V_G at 5 K. Blue circles represent experimental data, and solid blue lines are provided to facilitate reading. (d) Temperature dependent R_{xx} under different V_G. Left and right panels are for hole and electron accumulation, respectively.[28]

The authors interpreted that in magneto-transport the dephasing length L_ϕ and spin relaxation length L_{so} of carriers can be effectively modulated with gate bias. As a result, SOI-induced weak antilocalization (WAL), together with a crossover from WAL to weak localization (WL), is observed near zero magnetic field. Based on the electric field modulation, a phase diagram deduced from the Iordanskii-Lyanda-Geller-Pikus (ILP) theory was established to distinguish WAL from WL. They report values of 7.7×10^{14} cm^{-2} for electrons at $V_G = +5$ V and 3.5×10^{14} cm^{-2} for holes at $V_G = -6$ V that are more than 100 times greater than typical values obtained in solid dielectric devices. As a direct result, as shown in the temperature dependent R_{xx} curves of Figure 2.23, they report an electric-field-induced crossover from localization (negative slope in R_{xx}-T curve) to metallic transport (positive slope in R_{xx}-T curve) at the highly charged interfaces. At these interfaces, localization has been ascribed to surface scattering from steps, surface defects, or impurities in the macroscopic-size graphene channel, while the metallic state originates from the Fermi level shift into the conduction or valence bands.

Then in Figure 2.24 they show the V_G dependent magnetoconductance, $\Delta\sigma(B) = \sigma(V_G, B) - \sigma(V_G, B = 0)$, of a biased graphene EDL transistor at 5 K with several important features and tried to fit the experimental data with four different localization theories. Among the four theories, only ILP theory is able to fit the $\Delta\sigma(B)$ well, even in a large magnetic field range up to 0.2 T, as indicated by the solid lines in Figure 2.24.

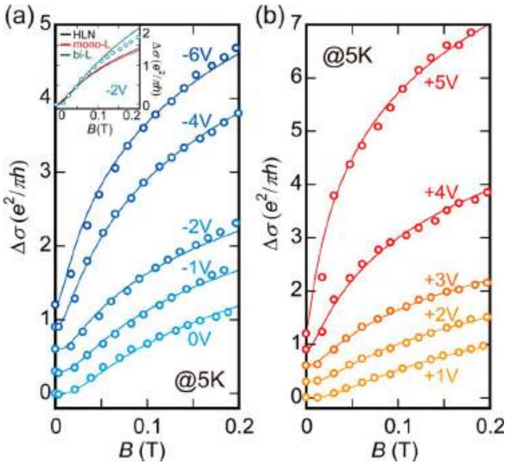

Figure 2.24. Magnetoconductance $\Delta\sigma$ of trilayer graphene in near-zero magnetic field regime at different V_G at 5 K. (a) and (b) show the $\Delta\sigma$ data and fitting curves using ILP theory in hole and electron sides, respectively. Circles represent experimental data and solid lines are their fitting curves. Curves and data are shifted up and down for clarity. Inset of (a): poor fitting curves for $\Delta\sigma$ at $V_G = -2$ V using Hikami-Larkin-Nagaoka (HLN) theory (black solid line); localization theories for monolayer graphene (red) and bilayer graphene (green).[28]

They suggested that the failure of the fitting equations specifically designed for graphene systems might be because of the lack of consideration of SOI. While within the scope of SOI, the failure of the Hikami-Larkin-Nagaoka (HLN) theory and the success of the ILP theory suggest the existence of SOI in three layer graphene EDL transistors.

Also this indicates that the Dyaknov-Perel (DP) mechanism related with Rashba spin splitting, rather than the Elliot-Yaffet (EY) mechanism caused by heavy impurities, is the dominating mechanism in three layer graphene systems.

Accordingly, as seen in the phase diagram in Figure 2.25 (b) obtained from the ILP theory and their fitting results, WAL in three layer graphene appears in the

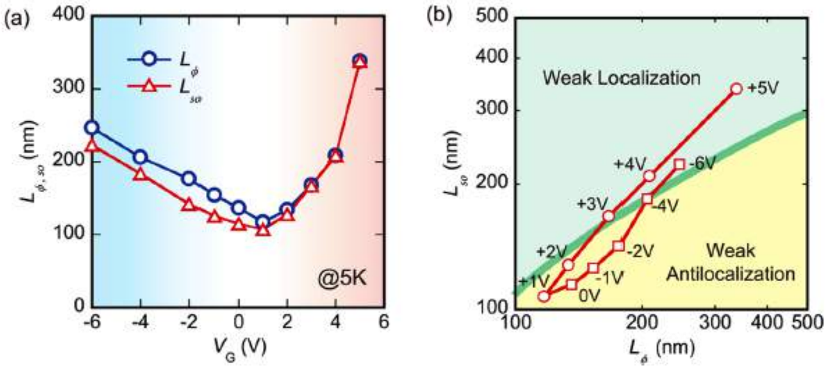

Figure 2.25. (a) V_G dependence of dephasing length L_{ϕ} and spin relaxation length L_{so} derived from ILP fitting. Blue circles represent L_{ϕ}, and red triangles represent L_{so}. (b) WAL-WL phase diagram in which the solid green line is the boundary between WAL and WL derived from the ILP theory.[28]

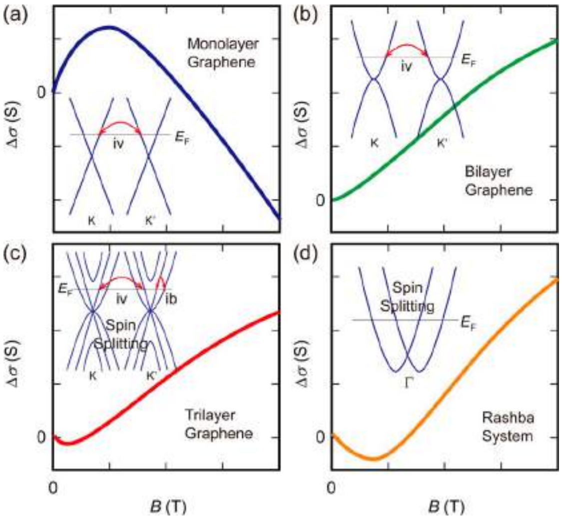

Figure 2.26. Schematic diagrams of $\Delta\sigma$ as a function of magnetic field at low temperature limit. The curves in (a) and (b) are based on experiments done on monolayer and bilayer graphene; the curve in (c) is drawn from observations in three layer graphene EDL transistors, and the curve in (d) is from experiments on conventional Rashba system. Insets: band structures and elastic scatterings of carriers such as intervalley scattering (iv) and interband scattering (ib).[28]

low n_s regime near the Dirac point, whereas the strong WL occurs at high n_s. This behavior is opposite to the conventional WL to WAL transition as n_s increases, showing the competition between the effects of SOI and intervalley scattering combined with inelastic scattering. Then a comprehensive understanding (Figure 2.26) of the quantum interference of trilayer graphene EDL transistors were further clarified by comparing the varieties of magnetoconductances and band structures shown by single- , bi-, and three-layer graphene as well as by a conventional Rashba systems. Since the WAL is observed at low-B regime in their experiment, they stated that it should be mainly induced by SOI, and the magnetoconductance curve in their experiment was explained as follows: SOI induces WAL in low-B limit and is suppressed in the higher-B regime so that intervalley-scattering-induced WL is observed.

A study of high carrier density in graphene with ionic-liquid gating has been made quite extensively [10], but a very high value of n_{2D} has not been achieved successfully even with ionic-liquid gates because the EDL capacitance, C_{EDL} between the ionic liquid and graphene involves the series connection of the geometric capacitance C_g and the quantum capacitance, C_q, which is proportional to the density of states. Authors of Ref. [10] investigated the variables that determine C_{EDL} at the molecular level by varying the number of graphene layers, n and thereby optimizing C_q. They report that C_{EDL} value is governed by C_q at n < 4, and by C_g at n > 4. This transition with n indicates a composite nature for C_{EDL}. Their finding clarifies a universal principle that determines capacitance on a microscopic scale, and provides nano-technological perspectives on charge accumulation and energy storage using an ultimately thin capacitor. At n = 1, a small C_{EDL} is observed, while increasing n, C_{EDL} increases and saturates at n > 4 as shown in Figure 2.27.

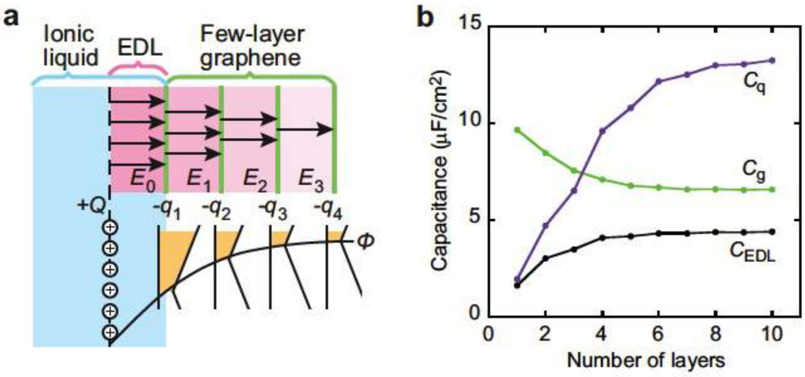

Figure 2.27. Model calculation of C_{EDL} (a) Schematic representation of the charge distribution $-q_i$ in FLG, which shields the electric field. (b) Calculated capacitances as a function of n. Geometrical capacitance C_g, quantum capacitance C_q, and EDL capacitance C_{EDL} are indicated by green, purple, and black lines, respectively. It is reported that the C_{EDL} is limited by C_q for n < 4 and by C_g for n > 4.[28]

2.4.2 Field effect in graphite

Since the parent material of graphene is graphite, a huge amount of study has been carried out on graphite. In our particular interest, the authors of Ref. [30] have studied out the effect of electric field on FLG, in order to investigate the possibility to obtain superconducting states by inducing excess charge at the surface of a sample. They made experiments on few multigraphene samples as a function of a bias voltage applied perpendicular to the graphene planes (of different thickness) and found that the resistance changes asymmetrically with the bias voltage sign.

They studied five FLG (thin graphite flakes) samples named S1, S2, S3, S4 and S5. Samples S1 and S3 were graphite flakes of $\simeq 40\ \mu$m length and with a non homogeneous thickness ranging between 20 nm and 40 nm. Samples S2 and S5 showed a homogeneous thickness of 40 nm and $\simeq 15\ \mu$m length. Sample S4 of 90 nm thickness was the thickest of all the studied samples. The temperature dependence of the resistance R(T) at zero bias voltage has been measured for every sample and shown in Figure 2.28(a). S1, S2 and S3 samples show a semiconducting behavior intrinsic to the graphite Bernal structure. The level of R(T) of sample S1 below 25 K as well as the features below 50 K in samples S2 and S3 and the metallic like behavior of S4 are due to the contributions of the surface of the sample (or sample-substrate) and/or due to the internal interfaces in the sample. As expected, the thicker S4 sample shows a metallic behavior below 100 K, which is related to the higher number of internal interfaces as reported in detail in Ref. [31]. These internal interfaces have a much larger carrier density than the graphene layers within the defect free regions of graphite. Therefore, the authors expected that in thicker samples the shielding of the electric field is much larger than in thinner ones.

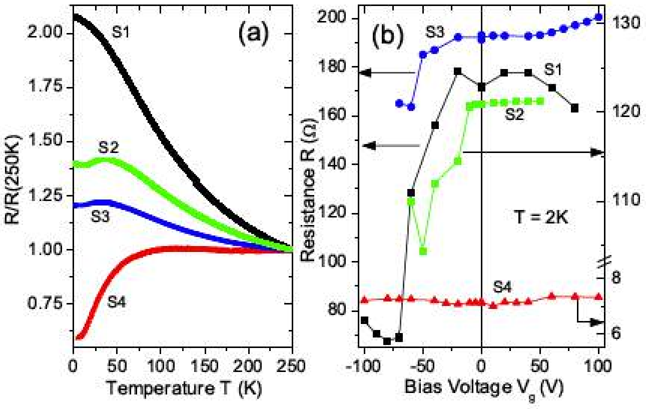

Figure 2.28. (a) Temperature dependence of the normalized resistance of four samples at zero bias voltage. (b) Bias voltage dependence of the resistance for samples S1 and S3 (left y-axis), S2 and S4 (right y-axis) at 2 K.[30]

They estimated the penetration depth of the applied electric field inside the samples and emphasizes that the actual screening depth depends on the experimental conditions, in particular the actual doping of the sample. In case the carrier density n of the non-defective graphene layers is smaller, then the larger will be the penetration depth of the electric field in the sample. Following Ref. [32] they estimated that at T < 30 K the effective penetration depth should be equal to at least seven graphene layers or about 2.4 nm. That would mean that the electric field mainly influences the near surface region of the samples, in case that no internal interfaces with much larger carrier density exist. Otherwise, as for sample S4, these interfaces would have largely screened the applied field and no effect was observed after application of a bias voltage. Figure 2.28 (b) shows the resistance vs applied bias voltage V_G at a constant temperature of 2 K. The curves shown in Figure 2.28 (b) were reversible, demonstrating the electrostatic nature of the observed effects.

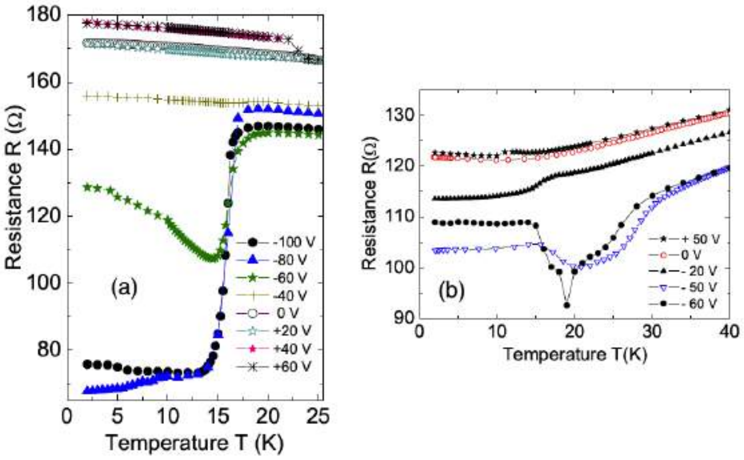

Figure 2.29. Temperature dependence of the resistance of samples at different constant values of V_G (a) S1 and (b) S2.[30]

The samples S1, S2 and S3 show an asymmetric behavior respect to zero voltage. For positive voltage the resistance does not change significantly. For negative V_G, however, a remarkable decrease of the resistance appears. A minimum value in the measured resistance was reached for slightly different negative bias voltages upon sample. These differences are related to the carrier inhomogeneity of the FLG samples. Note that for the thickest sample S4 the resistance does not show any significative change with V_G. This is due to the screening effect of the electric field by the internal interfaces. Their experimental measurement of temperature dependence of the resistance show a clear step like transition at V_G = -60 V for samples S1, S2, S3 and S5. Later they show in Figure 2.29 the results measured for samples S1 and S2 at different applied V_G. The authors claim that the overall shape of these curves suggests the existence of a non-percolative superconducting transition. The lower the bias voltage the clearer the transition triggered by the change in the carrier density. They compare their results with the overall behavior of the resistance under applied V_G that strongly resemble the one obtained for $ZrNCl$ flat thin film in Ref. [33]. They ascribe this behavior to the carrier inhomogeneities of their samples, a fact related to the large sensitivity of the carrier density of the graphite structure to defects and impurities.

They also inspected the behavior of the resistance under applied magnetic field and reported that an appropriate intensity of magnetic field in both directions (parallel and perpendicular) suppresses the transition.

They interpret this observed step like ”transition” as the sign of granular superconductivity, however, they argue that in order to reach a state of zero resistance in some part of the graphite sample, one needs to have a doped region large enough that one or several Josephson coupled superconducting patches exist between the voltage electrodes. This appears still difficult to be obtained by applying only an electric field in the samples used in this work.

Bibliography

[1] C. H. Ahn et al., Electric field effect in correlated oxide systems, *Nature*, 424, 1015, 2003.

[2] K. Ueno, H. Shimotani, H. Yuan, J. Ye, M. Kawasaki and Y. Iwasa. Field-induced superconductivity in electric double layer transistors. *Journal of the physical society of japan*, 83, 032001, 2014.

[3] G. Bonfiglioli, E. Coen, and R. Malvano. Modulation of conductivity by surface charges in metals. *Phys. Rev.*, 103:1906-1906, Sept. 1956.

[4] G. Bonfiglioli and R. Malvano. Surface states in metals. *Phys. Rev.*, 115:330-335, Jul 1959.

[5] G. Martinez-Arizala, D. E. Grupp, C. Christiansen, A. M. Mack, N. Marković, Y. Seguchi, and A. M. Goldman. Anomalous field effect in ultrathin films of metals near the superconductor insulator transition. *Phys. Rev. Lett.*, 78:1130-1133, Feb 1997.

[6] N. Marković, C. Christiansen, G. Martinez-Arizala, and A. M. Goldman. Electric-field effect in ultrathin films near the superconductor-insulator transition. *Phys. Rev. B*, 65:012501, Nov 2001.

[7] A. Sola, Ph.D. thesis, Politecnico di Torino, 2011-2013 (unpublished).

[8] G. Inzelt, Electroanalytical Methods: Guide to Experiments and Applications, edited by F. Scholz (Springer-Verlag, Berlin, 2010), p. 147.

[9] D. Daghero, F. Paolucci, A. Sola, M. Tortello, G.A. Ummarino, M. Agosto, R.S. Gonnelli, Large conductance modulation of gold thin films by huge charge injection via electrochemical gating, *Phys. Rev. Lett.*, 108, 066807, 2012.

[10] M. Tortello, A. Sola, Kanudha Sharda, F. Paolucci, J.R. Nair, C. Gerbaldi, D. Daghero, R.S. Gonnelli, App. Surf. Sci., 269 (2013) 17-22.

[11] Novoselov K. S., Geim A. K., Morozov S.V., Jiang D., Zhang Y., Dubonos S.V., Gregorieva I.V., and Firsov A.A. *Science*, 306(666), 2004.

[12] Frank Schwierz. *Nature Nanotechnology*, 5, 487-496, 2010.

[13] Castro, E. V. et al. Biased bilayer graphene: semiconductor with a gap tunable by the electric field effect. *Phys. Rev. Lett.*, 99, 21680, 2007.

[14] Gava, P., Lazzeri, M., Saitta, A. M. and Mauri, F. Ab initio study of gap opening and screening effects in gated bilayer graphene. *Phys. Rev. B*, 79,

165431, 2009.

[15] Ohta, T., Bostwick, A., Seyller, Th., Horn, K. and Rotenberg, E. Controlling the electronic structure of bilayer graphene. *Science*, 313, 951-954, 2006.

[16] Zhang, Y. et al. Direct observation of a widely tunable bandgap in bilayer graphene. *Nature*, 459, 820-823, 2009.

[17] Lemme, M. C., Echtermeyer, T. J., Baus, M. and Kurz, H. A graphene field-effect device. *IEEE Electron Dev. Lett.*, 28, 282-284, 2007.

[18] Liao, L. et al. High-κ oxide nanoribbons as gate dielectrics for high mobility top-gated graphene transistors. *Proc. Natl Acad. Sci. USA*, 107, 6711-6715 2010.

[19] Jianting Ye, Monica F. Craciun, Mikito Koshino, Saverio Russo, Seiji Inoue, Hongtao Yuan, Hidekazu Shimotani, Alberto F. Morpurgo, and Yoshihiro Iwasa, *PNAS*, 108, 32, 13002-13006, 2011.

[20] J. T. Ye, S. Inoue, K. Kobayashi, Y. Kasahara, H.T. Yuan, H. Shimotani and Y. Iwasa, *Nature Mat.*, 9, 125-128, 2009.

[21] Kopnin NB, Sonin EB. BCS superconductivity of Dirac electrons in graphene layers. *Phys. Rev. Lett.* 100:246808, 2008.

[22] Uchoa B, Neto AHC. Superconducting states of pure and doped graphene. *Phys. Rev. Lett.*, 98:146801, 2007.

[23] Lee B, et al. Modification of electronic properties of graphene with self-assembled monolayers. *Nano Lett.*, 10:2427-2432, 2010.

[24] Stoller MD, Park SJ, Zhu YW, An JH, Ruoff RS. Graphene-based ultracapacitors. *Nano Lett.*, 8:3498-3502, 2008.

[25] Ohno Y, Maehashi K, Yamashiro Y, Matsumoto K. Electrolyte-gated graphene field-effect transistors for detecting pH protein adsorption. *Nano Lett.*, 9:3318-3322, 2009.

[26] A. Pachoud, M. Jaiswal, P.K. Ang, K. P. Loh and B. Ozyilmaz, *Europhysics Lett.*, 92, 27001, 2010.

[27] D. K. Efetov and P. Kim, *Phys. Rev. Lett.*, 105, 256805, 2010.

[28] Z. Chen, H. Yuan, Y. Zhang, K. Nomura, T. Gao, Y. Gao, H. Shimotani, Z. Liu, Y. Iwasa. Tunable spin-orbit interaction in trilayer graphene exemplified in electric-double-layer transistors, *Nano Lett.*, 12, 2212-2216, 2012.

[29] E. Uesugi, H. Goto, R. Eguchi, A. Fujiwara and Y. Kubozono. Electric double-layer capacitance between an ionic liquid and few-layer graphene. *Scientific Reports*, 3:1595, DOI:10.1038/srep01595, 2013.

[30] A. Ballestar, J. Barzola-Quiquia, S. Dusari, P. Esquinazi, R. R. da Silva and Y. Kopelevich. Electric Field induced Superconductivity in Multigraphene, arXiv:1202.3327v1 [cond-mat.supr-con], 2012.

[31] J. Barzola-Quiquia, J.-L. Yao, P. Rödiger, K. Schindler and P. Esquinazi. Sample size effects on the transport properties of mesoscopic graphite samples.

Phys. Stat. Sol. (A), 205:2924-2933, 2008.

[32] M. A. Kuroda, J. Tersoff, and G. J. Martyna. Nonlinear screening in multilayer graphene systems. *Phys. Rev. Lett.*, 106:116804, 2011.

[33] J. T. Ye, S. Inoue, K. Kobayashi, Y. Kasahara, H. T. Yuan, H. Shimotani, and Y. Iwasa. Liquid-gated interface superconductivity on an atomically flat film. *Nature Materials*, 9:125-128, 2010.

[34] K. Ueno, S. Nakamura, H. Shimotani, H. T. Yuan, N. Kimura, T. Nojima, H. Aoki, Y. Iwasa, and M. Kawasaki. Electric-field-induced superconductivity in an insulator. Nature Mater., 7:855-858, 2008.

Chapter 3

Our implementation of EDL technique

3.1 Field effect devices (FEDs)

We decided to study the conductance variation produced by field-effect through an electrochemical gating mainly in single and few layers of graphene. For this purpose we produced graphene in two different ways: mechanical exfoliation and chemical vapor deposition (CVD). The detailed processes are described in section 1.1.3: here we describe some preliminary characterizations that have been performed to probe the number of layers through optical methods and the quality of these flakes through Raman measurements (before and after drop casting the polymer). Then the required patterning of the contacts over the flakes by electron beam lithography (EBL) to obtain Hall bar geometry is described.

Graphene layers can be identified when deposited on top of proper substrates using optical microscopy [1]. By analyzing the optical contrast of graphene planes with respect to the substrate it is possible to precisely characterize the number of layers. The most common of such substrates is Si/SiO_2 with SiO_2 thickness of about 300 nm (Figure 3.1). In this particular kind of substrates, since the dielectric thickness is comparable with the visible light wavelength, interference effects occur at the interfaces. Depending on the dielectric thickness different wavelengths are absorbed or reflected, giving particular reflectance spectra. The presence of a graphene layer on top of the SiO_2 surface can alter the boundary conditions at the interface so much that the resulting optical contrast can be used to identify the material, and easily characterize the number of atomic planes composing it. Such multilayer optical system can be studied within the framework of Fresnel coefficients calculation, using optical matrices, by analyzing the boundary conditions for electric and magnetic field for every interface (details are given in Ref. [2]).

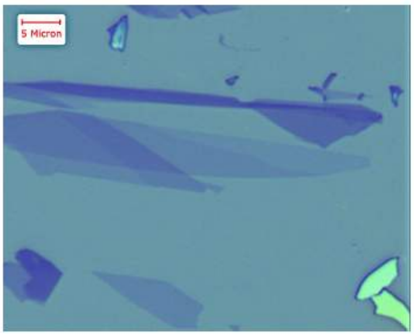

Figure 3.1. Optical image, obtained with a 100X objective in reflection configuration, of thin graphitic material deposited on top of a Si/SiO_2 substrate with dielectric thickness of 285 nm. The uniform background color is that of the bare and clean substrate. It is possible to notice area with different colors due to the presence of thin graphite layers, the darker the color the thicker the deposited material. The clear and shining parts in the lower right corner are thick graphite flakes, no longer transparent but reflecting the incident light.

Although graphene can be characterized by many techniques including atomic force microscopy (AFM), and transmission electron microscopy (TEM), Raman spectroscopy is a much more powerful tool. It can be used to determine the number of layers as well as to identify if the structure of graphene is perfect and account for associated defects. Raman fingerprints have been able to differentiate single-, bi- and few-layer graphene. A typical Raman spectrum of SLG shows a D-mode at approximately 1350 cm^{-1} and the G-mode at approximately 1583 cm^{-1}, while other modes are at 1620 cm^{-1} (D'), 2680 cm^{-1}($2D$), and 2947 cm^{-1}($D+G$) (Figure 3.2). The G mode is due to the E_{2g} mode at the Γ-point and the G-band arises from the stretching of $C-C$ bond in graphitic materials. The D-mode, instead is caused by the disordered structure of graphene. If graphene has a perfect structure, the Raman spectra results in the absence of D peak. If there are some randomly distributed impurities or surface charges in graphene, the G peak can split into two peaks, at 1583 cm^{-1} and D' peak at 1620 cm^{-1}. The main reason is that the localized vibrational modes of the impurities can interact with the extended phonon modes of graphene resulting in the observed splitting.

All kinds of sp^2 carbon materials exhibit a strong peak in the range 2500 - 2800 cm^{-1} in the Raman spectra. Combined with the G-band, this spectrum is a Raman signature of graphitic materials and is called $2D$ band. $2D$ band is a second order two phonon process and exhibits a strong frequency dependence on the excitation laser energy. $2D$ band can also be used to determine the number of layers of graphene because the shape of $2D$ band is pretty much different in FLG from that in the SLG. The $2D$ band in the SLG is much more intense and

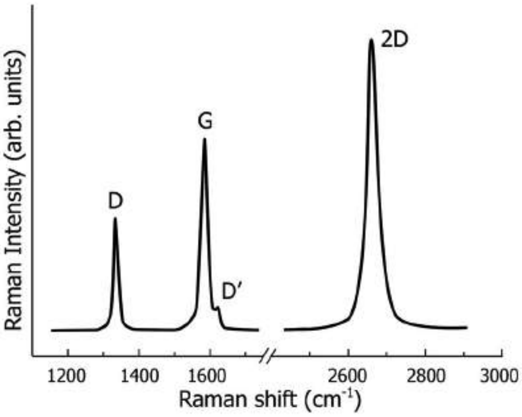

Figure 3.2. Typical Raman spectrum of single graphene layer.

sharper as compared to $2D$ band in FLG. The evolution of Raman spectra with the number of graphene layers depends majorly on the type of substrate and the method of preparation of the sample. In turn the G mode peak position and the intensity ratio of G and $2D$ bands depends on it. Figure 3.3 shows Raman spectra of graphene flakes used for our study. Note that the D peak corresponding to defects is absent even after deposition of the PES.

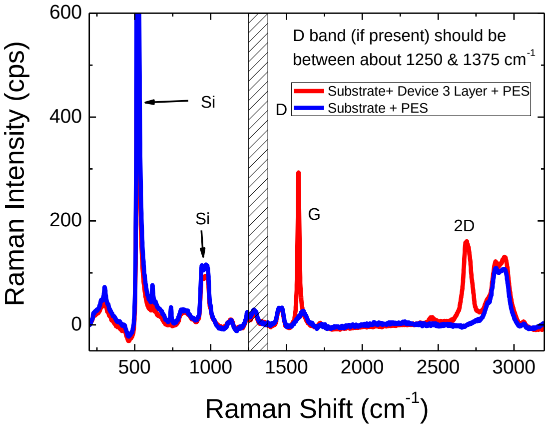

Figure 3.3. Raman spectrum of our field effect graphene devices after depositing PES.

3.1.1 Lithographic techniques

Photolithography (PLG) and electron-beam lithography (EBL), techniques are the most commonly used fabrication techniques that allow easy realization of structures with size down to few tens nanometers in the semiconductor industry and at research laboratories. Since the devices are designed to be planar for working on flat surfaces, these techniques are suitable for the fabrication of graphene-based electronic devices.

Photolithograhy

For realizing metal contacts on a graphene flake deposited on a SiO_2 substrate by positive PLG the following steps are required:

1. A layer of AZ5214E photoresist is spun on the substrate at 3500 rpm for 30 seconds.

2. Then the sample is baked on a hot plate at 110°C for 3 minutes in order to remove the solvent from the polymer layer. The resulting thickness of the resist layer is ≈ 1.4 μm.

3. The sample is placed in a mask-aligner that allows to position the lithography mask on the flake with micro-metric precision. This step is quite skill demanding since the photoresist layer changes the optical properties of the substrates, making the graphene flake almost invisible under the microscope.

4. When the right position of the mask with respect to the flake is reached and the mask has been brought in good contact with the sample, it possible to proceed with the UV exposure for 9 or 10 seconds, depending on the structures to be realized, small structures require lower exposure.

5. Finally the sample is immersed in the developer solution for 25 to 30 seconds, rinsed in deionized water and dried with nitrogen flow.

In the case of negative PLG the procedure is similar:

1. A layer of the same AZ5214E photoresist is spun on the substrate at 4000 rpm for 30 seconds.

2. Then the sample is baked on a hot plate at 85°C for 1 minute in order to remove the solvent from the polymer layer. The resulting thickness of the resist

layer is $\approx 1.1\ \mu$m.

3. The mask is aligned with respect to the flake's position and brought in contact with sample's surface.

4. UV exposure for 10-12 seconds, depending on the structures to be realized, small structures require lower exposure.

5. The sample is baked again at 85°C for 1 minute and re-exposed without the mask for about 40 seconds. This inversal bake and flood exposure make the sample's part exposed in the first instance to cross-link, making them insoluble by the negative developer.

6. The sample is then immersed, for about 10 seconds, in the negative developer solution that dissolves the exposed parts leaving behind the unexposed ones. A final rinse in deionized water and dry with nitrogen flow completes the procedure.

Both processes are schematized in Figure 3.4. Indeed, since the alignment process is the most difficult part of this procedure, the negative process results by far the easier one since most of the mask will be transparent, allowing an easier identification and alignment on the flake (see Figure 3.5).

Electron-beam lithography (EBL)

The resolution of non-projection PLG is limited by the wavelength of the illumination light used, that makes difficult to realize structures with lateral sizes smaller than 1 μm. Following the same principle, EBL has been developed. This technique exploits the interaction between a particular resist polymer and an electron-beam for realizing microscopic structures that, thanks to the very small size of the focused electron-beam, can be as small as a few tens of nanometers. This can be done by the same technology on which is based the scanning electron microscope (SEM), and indeed the fabrication work was performed on a SEM equipped with a $Nano - Patter\ Generation\ System$ (at Istituto Nazionale di Ricerca Metrologica, INRIM, Torino, Italy) that allows to control the electron-beam and scan the polymer surface with respect to a defined pattern [3]. The steps for the realization of microscopic structures with EBL are the following:

1. Graphene deposition must be made on a substrate previously patterned with a regular array of gold markers that will be used for the alignment.

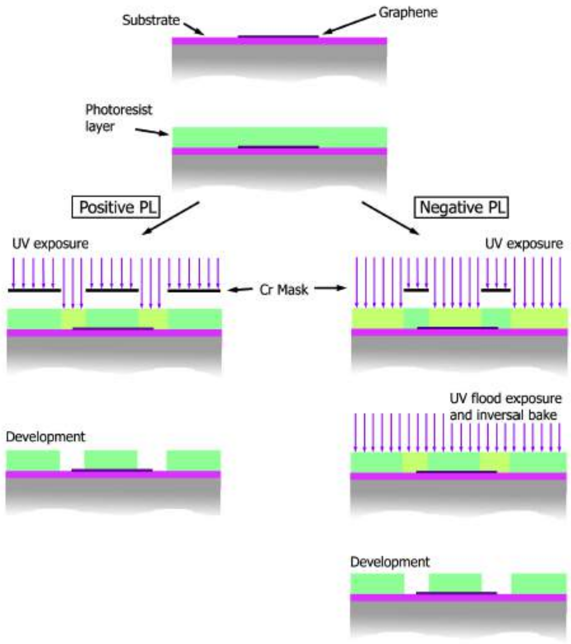

Figure 3.4. Photolithographic process for the fabrication of graphene devices.

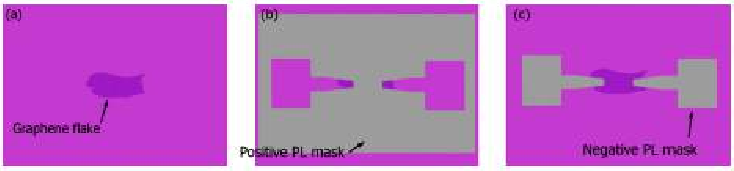

Figure 3.5. Alignment conditions in the different processes. In (a) the deposited graphene flake on which we want to fabricate electrical contacts; (b) in case of a positive process, most part of the mask is reflective and the flake is seen only through the holes of the contact geometry; (c) the alignment in negative process results much easier since most part of the mask is transparent.

2. The position of the flake with respect to the closest gold markers must be accurately measured by means of an optical microscope.

3. The PMMA resist (Polymethylmethacrylate, 950k, 4%) is spun on the substrate at 4000 rpm for 45 seconds.

4. The substrate is then baked on the hot plate at 165°C for 5 minutes in order to remove the solvent and harden the polymer layer.

5. The sample is now ready for the exposure. It is therefore placed in the lithography chamber, then the pattern is aligned with respect to the markers and written with the electron beam. The electron beam, a few pA at 30 kV, breaks the polymer chains making the exposed regions soluble in the developer.

6. The sample is developed for 70 seconds in a 4:1 mixture of isopropanol and MIBK(4-methyl-2-pentanone) at room temperature. For stopping the development and for further cleaning, the sample is washed in isopropyl alcohol (IPA) for 20 seconds and dried with nitrogen flow. The end result is a wafer covered with polymer except of the places where the contacts have to be deposited (exposed pattern).

The main difference between PLG and EBL is that the former is a parallel process, so that the pattern is exposed all at once, while the latter is a *serial* process because the beam has to scan, point by point, all the surface defined by the pattern. This means that it is difficult to realize by EBL big structures with size in the order of several hundreds on micrometers, the one typically required for contact pads. In this case PLG performs better even if it has lower resolution.

Metal deposition

Once the desired structures have been carved on the polymer, metallic structures can be made by metal evaporation and lift-off. Metal evaporation is carried out in dedicated machines where metal is heated in vacuum by an electron beam (several mA at 5 kV), as schematized in Figure 3.6 (left). The heated metal melts and sublimates depositing on the sample's surface placed in the chamber. Metallic contacts for electronic measurement are typically made by a thin layer of chromium or titanium, about 10 nm used as adhesion layer, and 50-150 nm of gold. After the metal deposition the sample is immersed in acetone that dissolves the resist polymer, thus removing the metal deposited on it. In the areas where the polymer was removed by lithography, the metal is deposited directly on the substrate and is not removed by acetone. Such procedure, called lift-off is visible in Figure 3.6 (right). In order to obtain a good lift-off, the thickness of the deposited metal film must be less than one third of the resist thickness. This means that in the case of EBL the metal deposition can be at most around 50-70 nm.

Etching the graphene flake into a Hall-bar configuration

QHE measurements typically require two current contacts and four to eight

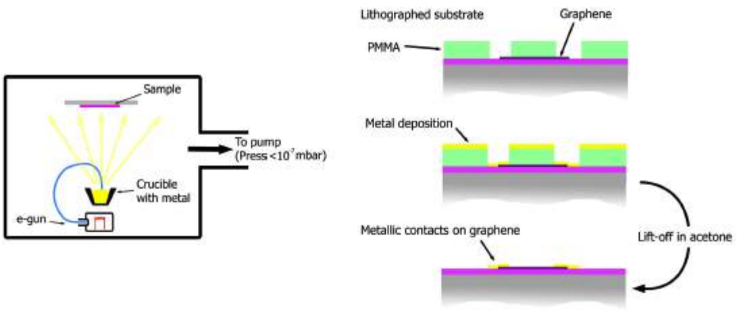

Figure 3.6. On the left, a scheme of the electron-beam evaporator. On the right the principle of lift-off used for the realization of metal contacts on graphene flakes.

voltage probes with the geometry schematized in Figure 1.10. Since the shape of deposited graphene flakes cannot be controlled prior to the deposition, as a final step for the fabrication of graphene-based devices for QHE measurements, the material must be etched and shaped into a Hall-bar. This can be done by an oxygen-based Reactive Ion Etching(RIE) process, after having realized a Hall-bar shaped protecting mask over the flake as schematized in Figure 3.7.

After the final step of the micro-fabrication, it is necessary to make the device suitable for an easy manual handling with a proper packaging. First, all the electric contacts are made with silver paint spots used to electrically connect to a copper platform to be measured on a pulse tube cryo-cooler. We used 20 μm gold wire to connect to the contacts on the device using a silver paint.

For large flakes, PLG is the fastest and the most simple way for fabricating graphene devices. Indeed, it requires no markers, fast manual alignment and, due to the high thickness of the photoresist layer, it is possible to make very thick metal evaporation that ease the final packaging. The advantage of PLG is that it gives the possibility of easily defining very large geometries. Moreover the large thickness of the photoresist layer allows to fabricate quite thick metallic contacts. On the other hand, with respect to graphene, PLG lacks for resolution. The contacts geometry, as well as the Hall-bar mask, are not well defined, with smoothed edges and ripples due to plastic deformations of the photoresist layer. To solve such problems it is possible to use PLG and EBL together for realizing different parts of the device. The large and thick pads can be fabricated by PLG, while the electrical contacts on the graphene flake, as well as the mask for the final shaping can be realized by EBL. However, in this method many fabrication steps are needed. The electrical contacts are realized by two steps, thus increasing the risk of damaging the graphene plane and the possibility of its contamination by resist residuals. These problems can be solved by depositing graphene on a

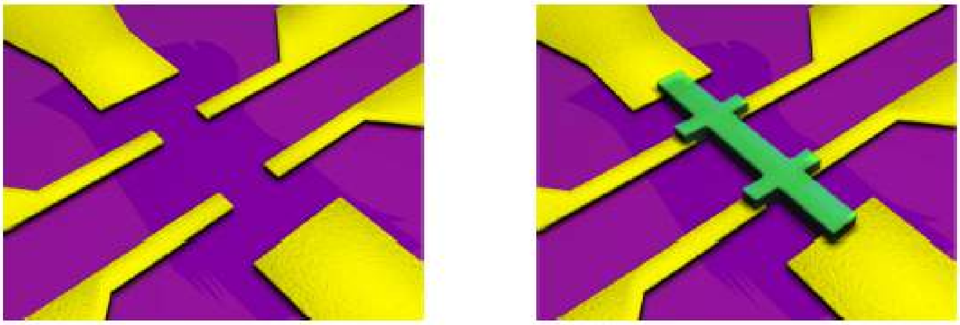

(a) Graphene flake deposited on a Si/SiO$_2$ substrate and contacted by metallic leads fabricated by EBL or Photolithography.

(b) By means of the same lithographic techniques Hall-bar shaped polymer mask is fabricated on the flake.

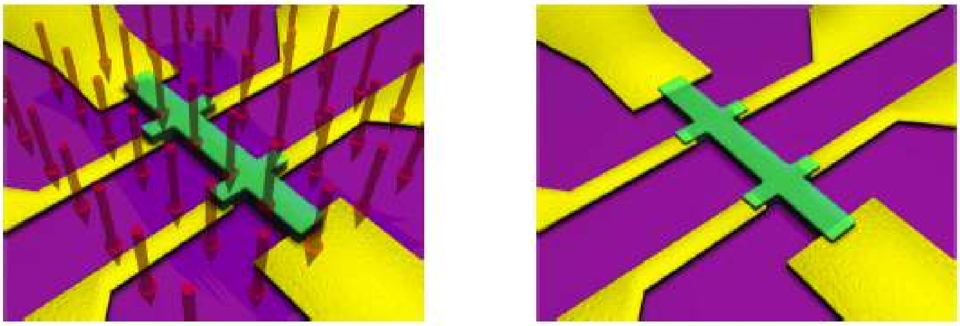

(c) The device is then processed by an oxygen-based RIE.

(d) The mask protects the underlying graphene flake from the oxygen-based RIE, the unwanted portion of the graphene flake are removed.

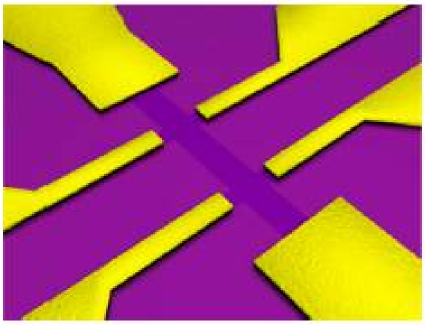

(e) The mask is then removed by immersing the sample in acetone, leaving the final device with optimized shape.

Figure 3.7. Sequence of fabrication steps for the final shaping of graphene devices for characterization.

substrate already patterned with aligned markers and then fabricate the small

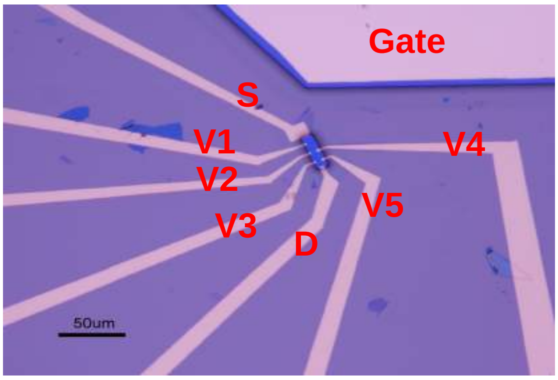

Figure 3.8. Typical device layout showing source (S), drain (D) and voltage contacts V with V1, V2, V3, V4, V5 labels. The gate pad is positioned besides the device in a planar geometry.

contacts by EBL before the big pads. In this way the interface between the two parts of the contacts is less critical and also the contacts/graphene interface is kept cleaner because it is realized at the very first step of the fabrication process.

A third way for fabricating graphene devices is by using only EBL for both contacts and pads. This requires a good EBL system able to define relatively large structures with good precision. The INRIM in 2010 has been equipped with such a machine, a $FEI\ QUANTA-3D$ SEM-FIB microscope, equipped with an NPGS [3] board for performing lithography, that now represents the main tool available at Nano-facility Piemonte [4]. Final device geometry is shown in Figure 3.8

3.1.2 Polymer preparation

The FEDs are fabricated in order to investigate the properties of different materials under the effect of electric field produced by PES. Hence, PES forms a very important part of these kind of experiments. We have made experiments with many different compositions of polymers and have opted for a particular composition of ingredients which has proved to induce record of surface carrier densities in metals and eventually in carbon based materials.

The PES for the gate has been developed within the collaboration of researchers of our group under the Department of Applied Science and Technology at Politecnico di Torino. Main research activities of these researchers have been focused in recent years on the development of Li-ion batteries. This technology is oriented to the realization of devices that can work for more than 1000 cycles and can operate at high volumetric and gravimetric energy densities, ranging between 200 and 300 Whkg^{-1}, and conductivity in the range of 10^{-7}-10^{-5} Scm^{-1} at room temperature. The Li-based polymers can ensure better mechanical integrity due

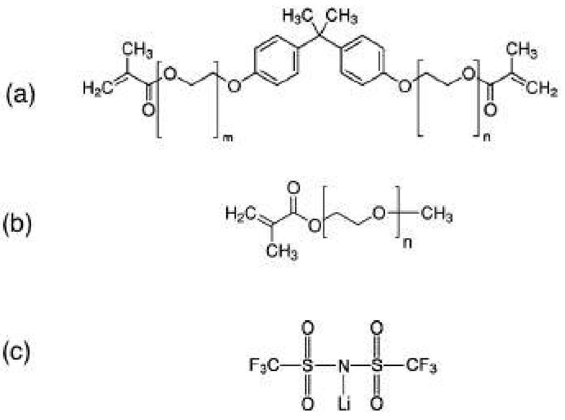

Figure 3.9. (a) Structure of Bisphenol A ethoxylate (15 EO/phenol) dimethacrylate (BEMA) (b) Structure of poly(ethylene glycol)methyl ether methacrylate (PEGMA) (c) Structure of bis(trifluoromethane)sulfonimide lithium salt (LiTFSI)

to the cross-linked nature of the polymer network, and wide thermal stability. All these properties of this polymer are favorable for our purpose of electrochemical gating. It has been verified that the electrical double layer (EDL) has been formed effectively using this PES at the interface of the sample under test. The choice of Li ions is favorable for the formation of a high capacitance EDL because of the reduced dimensions of the ions. The formulation of the solid polymer electrolyte membranes was based on Bisphenol A ethoxylate (15 EO/phenol) dimethacrylate (BEMA) (Figure 3.9 (a)), a methacrylic based di-functional oligomer having an average molecular weight of 1700, obtained from Sigma-Aldrich. Poly(ethylene glycol) methyl ether methacrylates in Figure 3.9 (b) with different molecular weights (i.e., PEGMA- 1100, PEGMA - 475 and PEGMA - 300 having average Mn of 1100, 475 and 300, respectively) were also obtained from Sigma-Aldrich. Bis (trifluoromethane) sulfonimide lithium salt (LiTFSI, CF3SO2NLi - SO2CF3, battery grade, in Figure 3.9 (c)), obtained from Ferro Corp. (USA), was used as the source of Li^+ ions. The free radical photo initiator was 2-hydroxy-2-methyl-1-phenyl-1-propanone (Darocur 1173/D1173), provided by Ciba Specialty Chemicals [5].

3.1.3 Device geometry

In order to study electric field effect on different graphene and metal devices, the devices are prepared in a planar configuration as follows: the flakes are either mechanically exfoliated and transferred to intrinsic Si substrate covered with SiO_2 ($\sim$ 300 nm thick) or grown through CVD on copper foils. Graphene flakes are selected and identified by optical microscopy and Raman spectroscopy depending on number of layers. Measuring D to G ratio and doping level also uses the latter technique to monitor the quality of samples. Mostly three-, four- and five-layer flakes were mechanically exfoliated and SLG was grown on copper to be used as channel in order to fabricate the FEDs. The source, drain and voltage ohmic contacts are patterned by standard EBL technique, metal evaporation (5 nm Cr/ 80 nm Au) and lift off as shown in Figure 3.10 (a). The voltage contacts are designed in a typical Hall bar configuration. All the devices were initially fabricated at INRIM, Torino, Italy and later at Cambridge Graphene Center, University of Cambridge, UK.

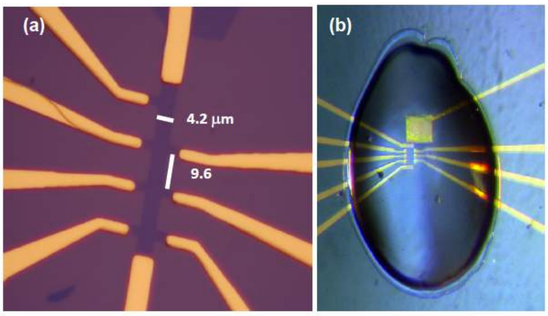

Figure 3.10. (a) Picture of a threlayer graphene FED, this graphene channel has been shaped for resistance and Hall effect measurements. (b) Photograph of a FED made of SLG grown by CVD on copper and transferred on a SiO_2 substrate, with the drop of PES on top.

In case of metal thin films a standard physical vapor deposition (PVD) was done in a deposition chamber equipped with a turbo-molecular pump and a heater. Vacuum can reach a 10^{-5} mbar measured by a Penning vacuum sensor. To shape the proper geometry of devices, a shadow mask was prepared and the evaporation was followed by a fine lift-off technique. For all the evaporated films we used silicon nitride or silicon oxide substrates that are cleaned in 30 minutes sonication and dried in a flow of argon or nitrogen. The photo-resist is exposed to a UV lamp and the mask we used is designed to obtain a 100 μm width strip with eight contact that allow simultaneous measurements of resistivity from different portions of the strip and Hall voltage because of the good alignment of the probe contacts. Later lift-off procedure was carried out in a soft flush of acetone.

To probe the structural quality of these metallic thin films from SEM images in Figure 3.11 (b) it is possible to see that the gold thin film is formed by different accretion islands that are connected to form a continuous network. Inside, small grain islands are present during the growth with a diameter of approximatively 15 nm. This kind of structure is comparable with the one present in the best Au films that can be obtained with the PVD technique.

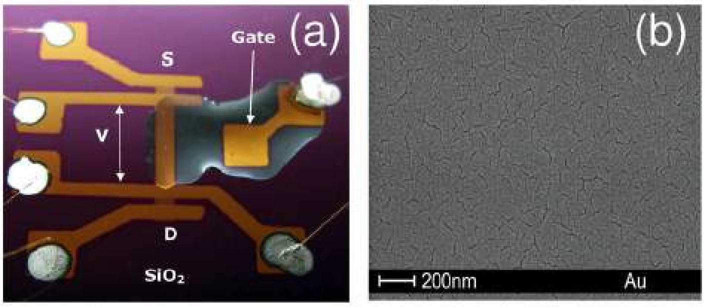

Figure 3.11. (a) Photograph of a *Au* FED on a SiO_2 substrate. D and S are the drain and source contacts; the voltage is measured between the inner contacts. The drop of polymer electrolyte covers the part of the film between the voltage contacts as well as the gate electrode. (b) SEM image of the *Au* film.[6]

A gate electrode several times larger than the active area (approximately 10,000 times for single and few layer graphene only) is positioned besides the active area as shown in the arrangement of Figure 3.8 and 3.10 (b). After designing contacts, PMMA photoresist is spin coated over the device apart from the active channel and the Au contact pads in order to prevent any possible interactions between PES and graphene edges/Au contacts. The Au pads are then contacted by thin Au wires using silver paint (made of silver powdered particles and a solvent, latter of which evaporates eventually forming a contact). The sample is then mounted on to a copper platform to be measured on a pulse tube cryo-cooler.

The configuration of PES we used is a reactive mixture of BEMA+PEGMA with LiTFSI in the presence of 3 wt% of a 2-hydroxy-2-methyl-1- phenyl-1-propanone free radical photo-initiator (Darocur 1173, Ciba Specialty Chemicals) as described in section 3.1.2. The quantities of BEMA and PEGMA are in a 3:7 ratio, and the LiTFSI is 10 wt% of the total compound. The PES was then polymerized by UV exposure using a medium vapor pressure *Hg* UV lamp, with radiation intensity on surface of the sample of 30 mW/cm^2. All the above operations were performed in the controlled *Ar* atmosphere of a dry glove box with O_2 and H_2 O content ≈ 0.1 ppm.

3.2 Measurement of Induced Charge: Experiments and models

As described in the previous section, after fabricating, processing and contacting the FEDs it is possible to make transport measurements. In this section we describe the different measurements and their procedure we carried out in order to study their properties. The electrochemical gate potential was applied by a Source

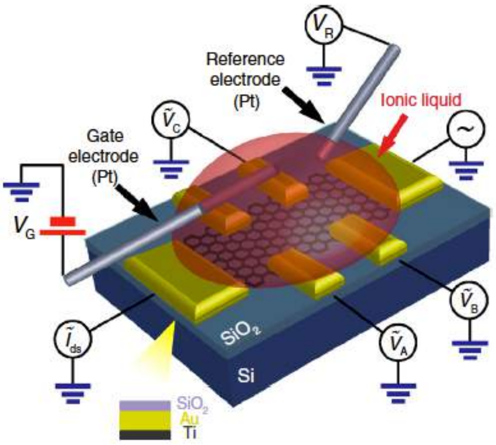

Figure 3.12. Schematic representation of a device including the bias configuration used in the electrical measurements.[7]

Measure Unit (SMU) through the PES to control the amount of carrier density induced at the PES/sample interface. The four-probe transport experiments were carried out using Keithley 6221/2182A instruments. Graphene flakes and the thin films of metal served as the channel as in a field effect transistor (FET) whose electrical characterization is performed with four probe measurements by inverting current during each measurement in order to cancel effects of thermoelectrical potentials due to the thermal gradient. Dielectric gate (as in the standard FETs) is replaced by drop of PES casted over the active area that is used to connect the channel with the gate pad (Figure 3.12).

As potential is applied through the gate electrode to the transport channel, immersed under the PES, the dissociated Li^+ cations and $TFSI^-$ anions inside the PES are driven to the interface of PES/channel (Figure 3.13). These ions accumulate towards the oppositely charged electrodes to form the dynamic and very thin EDL. The two plates of EDL formed by ions at the PES/channel interface, viewed as a nano-gap ($\approx$ 2 nm) capacitor with a considerably high capacitance, accumulates an incredible amount of counter charges that is impossible to attain through the use of conventional solid gate dielectric.

3.2.1 Double step chronocoulometry

Although a direct estimate of the total surface charge carrier density can be obtained through Hall effect measurements, however two considerations in our case limit the ability of Hall measurements to provide a precise value of the induced charge: a) our main interest lies in the fact that how much charge has been induced at the PES/sample interface while polymerizing PES to measure the corresponding

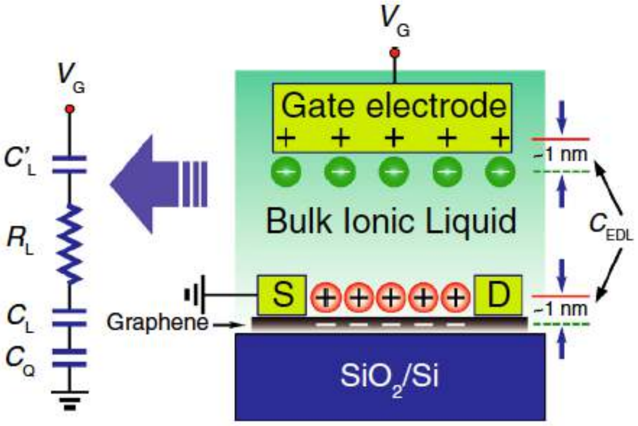

Figure 3.13. A schematic cross-section of graphene FED, together with the equivalent electrical circuit describing its operation. In the equivalent circuit, C'_L is the capacitance between Pt gate and liquid, R_L is the electrical resistance of bulk ionic liquid (here ionic liquid instead of PES), where transport is mediated by ions, C_L and C_Q, are the geometrical capacitance of double layer/graphene interface and the quantum capacitance of graphene associated with the finite density of states respectively.[7]

induced charge and b) the peculiar geometry of the FEDs measured here does not have specific details of various parameters related to geometrical characteristics and dielectric constant. Also, integrating the gate current flowing through PES provides an overestimation of charge that forms EDL since the current flows due to a combination of two effects which are absolutely necessary to separate. Owing to these limitations it would be useful to exploit the electrochemical properties of the PES with the aim to determine the amount of charge induced.

In this regard, a powerful technique of electrochemistry, that is suitable for our purpose is called the double-step chronocoulometry. It aids in separating the charge of the EDL from the electrochemical effects that are present and yields only the induced or the extra added charge. The series of operations to perform in order to extract the value of induced charge are described in detail in Ref. [8]. The technique is based on the analysis of electric current that flows through the PES on the application of a particular bias sequence. Making measurements in this way, it is possible to investigate the variation of sheet carrier density when we polarize the electrolyte with the view of extending this charge measurement techniques to other device fabrication processes where the use of PLG or EBL for precise Hall bar shaping is not possible. More details of this topic will be given in the following sections.

A general description of this powerful electrochemical can be found in Ref. [9]. Double-step chronocoulometry is a DC technique that is based on the analysis of the electric current that flows through the electrolyte solution when a particular bias is applied on it. The idea of chronocoulometry originated from the two Faraday's laws of electrolysis that are the application of the law of conservation of matter and conservation of charge to electrolytic processes. These laws define a quantity called the Faradaic current or diffusion current as:

$$I_d(t) = \frac{nFAD^{\frac{1}{2}}c^*}{\sqrt{\pi t}} \tag{3.1}$$

here, n is the number of electrons, F the Faraday's constant, A the area of the electrode, c^* is the equilibrium concentration and D is the diffusion coefficient. The most important feature of the Faradaic current is the reverse proportionality to the square root of time: this can be easily measured with a time-resolved amperometer and all the deviations from this behavior can be referred to other electrochemical phenomena. In particular the phenomenon that we investigate here is the charging of the EDL where the current vs time dependency deviates significantly from the expression of Faradaic current stated above as is shown in the following. In order to describe the formation of the EDL at the surface of the electrode, we model the electrolytic solution by an equivalent circuit that consist of two capacitors and a resistance in series (Figure 3.13). The two capacitances are the capacitance of electrical double layer C_{EDL} and of the electrode. The circuit that is described by the following equations is made by the parallel of C'_L , R_L and C_L (in Figure 3.13). The value of C_L $(= C_{EDL})$ depends on C_Q.

$$\frac{1}{C_{EDL}} = \frac{1}{C_g} + \frac{1}{C_Q} \tag{3.2}$$

The effect of C_Q dominates the expression since its value is small. The resistance in series R_s is the ohmic resistance of the electrolyte solution. The electrical current involved in the formation of the EDL is a capacitive current $I_c = dQ/dt$ that in the case of a potential step of magnitude E assumes the following form, assuming that at time $t = 0$, $Q = 0$:

$$I_c = (E/R_s)exp(-t/R_sC_{EDL}) \tag{3.3}$$

The expression of this current describes an exponential decay after the application of potential E with a time constant $\tau = R_sC_{EDL}$. The Faradaic current and the capacitive current occur almost simultaneously but the time decay is different: a dependency on square root of time occurs for the Faradaic current and an exponential dependency on time for the double layer charging current. The response of these two currents to a potential step is sketched in the Figure 3.14.

The time integral of the expression of each current gives the amount of charge involved in the process as:

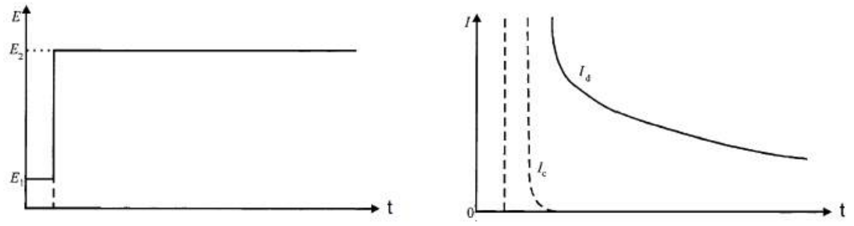

(a) (b)

Figure 3.14. a) Potential step application b) Faradaic current I_d and capacitive current I_c.[9]

$$Q = \int_0^t I dt \tag{3.4}$$

$$Q_d(t) = \int_0^t nFAD_R^{0.5} c_R^* \pi^{0.5} dt = 2nFAD_R^{0.5} c_R^* \pi^{-0.5} t^{0.5} \tag{3.5}$$

$$Q_c(t) = \int_0^t (E/R_s) exp(-t/R_s c_d) = EC_d(1 - exp(-t/R_s C_{EDL})) \tag{3.6}$$

Being derived from the Faradaic current, Q_d represents the diffused charge and Q_c coming from the capacitive current, represents the charge stored during the formation of the EDL. This latter charge is the observable on which we focus our study. The growth of these two charges as a consequence of application of a step bias is shown in Figure 3.15.

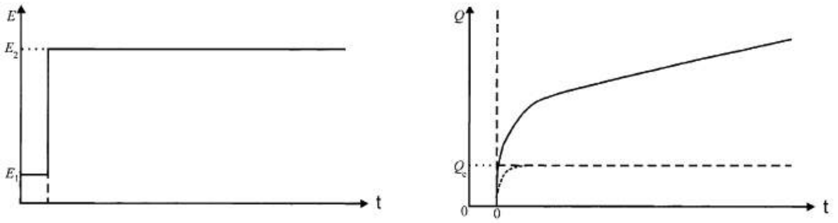

(a) (b)

Figure 3.15. a) Potential step application b) Diffused charge Q_d and electrical double layer charge Q_c.[8]

Since the evolution in time of $Q_d(t)$ and $Q_c(t)$ is simultaneous and the integration of the measured current gives a charge $Q(t) = Q_d(t) + Q_c(t)$, it is necessary to

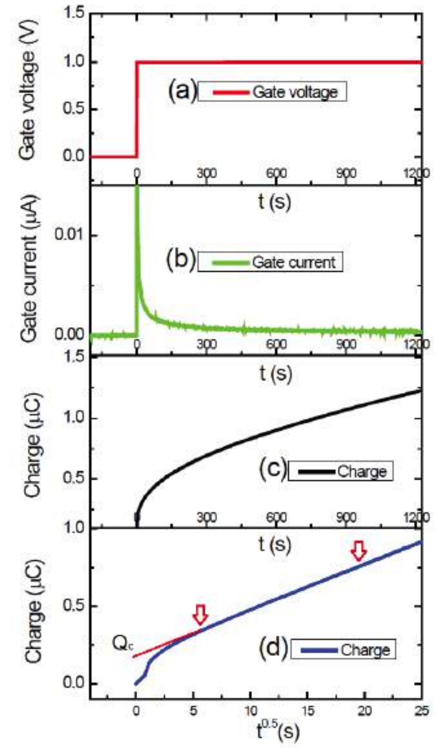

Figure 3.16. a) step potential applied to PES b) current flowing through the solution as a consequence of potential application: this current contain both Faradaic and capacitive contributions c) total charge $Q(t) = Q_d(t) + Q_c(t)$ obtained by integration of the current d) total charge plotted as a function of the square root of time: in this plot it is possible to extract the value of Q_c: red arrows show the linear fit region.

distinguish the two different contributions from their time dependency: $Q_d(t) \propto \sqrt{t}$ and $Q_c(t) \propto exp(-t)$. If one plots $Q(t) = Q_d(t) + Q_c(t)$ as a function of square root of time, the diffusive contribution to the charge $Q_d(t)$ will give a linear behavior and will allow detecting the exponential behavior of the double layer charge $Q_c(t)$. This procedure is equivalent to fitting $Q(t)$ with an arbitrary exponential and check the value at which $Q(t)$ deviates towards the $Q_d(t)$ behavior. The measurement procedure is summarized in Figure 3.16. In the bottom-most graph, charge is plotted as a function of the square root of time and the maximum value of Q_c is presented.

All these procedures involved during the application of a potential step have an equivalence to the case of removal of the same potential. This is the main principle of the two step chronocoulometry. In this way it is possible to measure both the charge that builds up the double layer during the application of bias and the charge that comes from the dissolution of the double layer, during the removal of the potential. This is a simple but powerful consistent check of the values measured at two different moments.

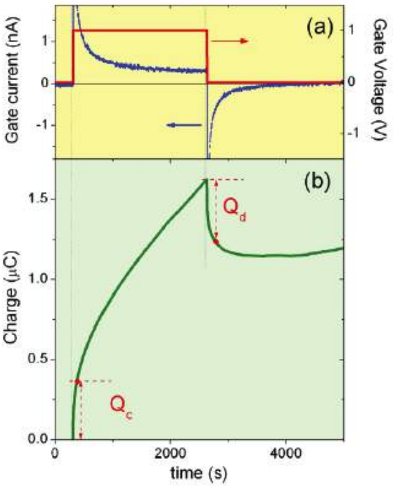

Figure 3.17. a) red line: application and removal of a step potential (1 V). blue line: current response to the potential b) total charge obtained as integral of the current: left part corresponds to the charging process and right part to the discharging one.[6]

In Figure 3.17 (a), the current response to the bias application is presented; it shows a peak both during application and removal of the gate voltage. In Figure 3.17 (b), the integration of the electric current i.e., the total charge is reported. It is possible to distinguish the charging process, represented by the left part of the curve from the discharging process, represented by the remaining portion of the curve. In Figure 3.18, a typical result of a double step chronocoulometry is presented: both lower and upper curve represents charge vs square root of time. The lower part of the curve in Figure 3.18 is the charge measured during the charging process, when the step voltage is applied: it starts to grow from zero and becomes linear when all the charge devoted to the formation of the EDL is stored: at this point, only the charge related to Faradaic current is detected and is represented by the linear branch of the charge vs square root of time curve.

The upper curve in the same Figure 3.18 shows the similar process that occurs during the removal of the bias voltage. In fact it is possible to separate the exponential part from the linear behavior but in a decreasing direction: the curve starts from a maximum value that is the charge stored in the EDL plus the charge diffused in the previous charging process. The amount of double layer charge measured during charging and discharging process is reported on the graph as Q_c

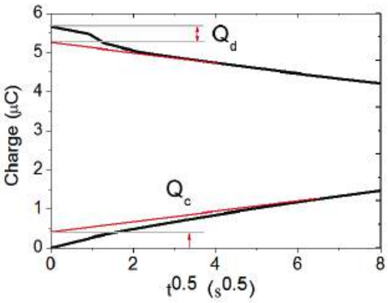

Figure 3.18. Total charge representing both for charging and discharging process is plotted vs the square root of time.

and Q_d respectively. As it is possible to see in this example, these two values are compatible since they belong to the same physical observable. Charges Q_c and Q_d are evidenced in the charge vs time graph of Figure 3.17 (b), where they can be evaluated only by an exponential fit. As anticipated above, the Faradaic current and the capacitive current have different time decay allowing their detectability and they can rise at the same time or with a delay between each other. The model described above always hypothesizes the simultaneous rising of these two current, and this is the most common case observed. However, in some cases, a starting time separation for the two currents is more compatible with the effect observed on the film under field effect whose electronic characteristics are investigated. This hypothesis allows us to take into account a value that is higher than the intercept between zero and the linear fit of the charge plotted in square root of time scale. An example of this modified procedure for the charge measurement is reported in Figure 3.19.

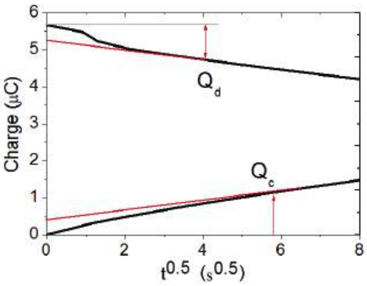

Figure 3.19. Total charge represented both for charging and discharging process plotted vs the square root of time under the hypothesis of a non-simultaneous rising of the Faradaic current and the capacitive current.

3.2.2 Comparison between double step chronocoulometry and Hall effect

In the previous section 3.2.1 the procedure of double-step chronocoulometry has been presented that allows the measurement of the charge in the EDL. If the graphene FEDs are shaped in a suitable way, it is possible to perform Hall effect and chronocoulometry measurements simultaneously. This procedure has been adopted to make a valid confirmatory check of double-step chronocoulometry as a tool to measure induced charges.

Hall effect was observed for the first time by Edwin Hall in 1879 and it is a consequence of the Lorentz force on a current flowing through a conductor under magnetic field.

$$\vec{F} = q(\vec{E} + \vec{v} \times \vec{B}) \tag{3.7}$$

The last term of equation 3.7 represents a force perpendicular both to the direction of current through the conductor ($\vec{v}$) and to the magnetic field ($\vec{B}$). This component ($\vec{B}$) generates a charge accumulation at the opposite borders of the conductor which in turn produces the Hall voltage V_H:

$$V_H = \frac{-IB}{den} \tag{3.8}$$

In the expression 3.8, I is the electric current, B is the magnetic induction, d is the thickness of the conductor, e is the fundamental charge and n is the volume density of charge of the conductor. The purpose of our experiments is not to obtain the precise value of the volumic charge density rather obtain its variations. The evolution from an unperturbed to a charged configuration of graphene device is detectable by Hall voltage variations. Simultaneously the EDL responsible for charge induction is monitored by the double step chronocoulometry. From the expression of Hall voltage (equation 3.8) it is possible to obtain:

$$\Delta n = \frac{Q + Q'}{V} - \frac{Q}{V} = \frac{IB}{deV'_H} - \frac{IB}{deV_H} \tag{3.9}$$

where V is the volume of the conductor, Q its charge since $n = Q/V$ is its volume charge density and Q' is the charge added to the conductor by field-effect. This charge modification changes the value of Hall voltage from V_H to V'_H. The expression 3.9 becomes

$$\frac{Q'}{Ad} = \frac{IB}{ed}(\frac{1}{V_H} - \frac{1}{V'_H}) \tag{3.10}$$

This is an expression of the induced charge that is independent from the properties of the conductor, in fact it is not necessary to know information about Q, its intrinsic volume charge as well as information about its thickness d. From equation 3.10, the expression of the induced charge with the hypothesis that it is distributed in a two dimensional region is:

$$\frac{Q'}{A} = \frac{IB}{e}(\frac{V'_H - V_H}{V_H V'_H}) \tag{3.11}$$

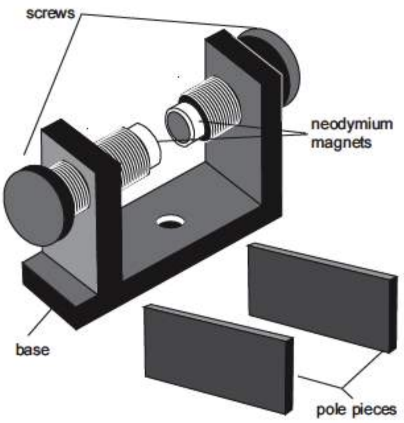

Figure 3.20. The variable gap magnet consists of two 3/4 inch diameter neodymium magnets on an iron base. Two flat pole pieces are supplied to provide a uniform field when needed. The gap may be varied from 0.5 cm to 8.9 cm by turning the screws.

This last expression 3.11 can be easily compared to a double step chronocoulometry measurement: Q' is compared to the capacitive charge and the surface area A is the exposed surface of the film within the same hypothesis stated above about the two-dimensional distribution of the induced charge. In order to carry out experiments the graphene devices were patterned in a Hall bar geometry as described in section 3.1 and shown in the Figure 3.8. Magnetic field was applied through a variable gap magnet, model $EM - 8641$ from $PASCO\ Scientific$ and every time the magnet was reverted manually in order to change the field direction. The device was either mounted on a pulse-tube cryocooler system or on a support stand system so that without removing the device from its position it becomes easier to flip the magnet as shown in Figure 3.21.

A CVD-grown SLG device was measured for this purpose: measurements have been performed with the variable gap magnet with magnetic fields of magnitude 0.4 T, 0.5 T and 0.6 T and the amount of electric current flowing through the channel was 1 μA. The first measurement led to the confirmation of the intrinsic charge density value for graphene $\approx 10^{13}$ cm^{-2} and the magnetic field dependency of the Hall voltage as evaluated for this purpose is shown in Figure 3.22.

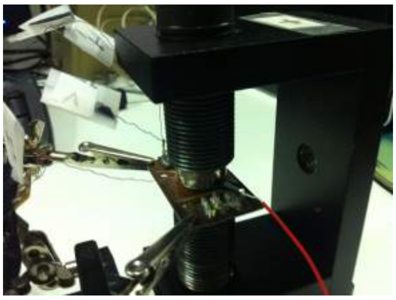

Figure 3.21. The variable gap magnet while measuring the device on a Cu platform as mounted with the help of support stand system connected to measuring instruments by connecting wires.

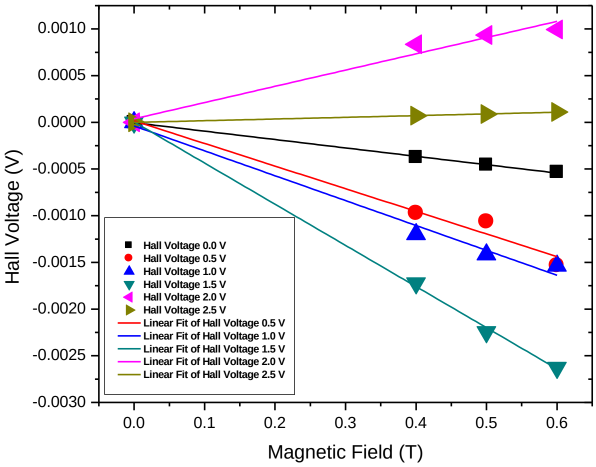

Figure 3.22. Linear fits of the Hall voltage vs magnetic field curve for a CVD–grown SLG device at different gate voltages

According to the expression 3.8 it is possible to calculate the linear fit of the Hall voltage vs magnetic field curve as in Figure 3.22 and obtain a value of n_{2D} since the thickness of a SLG film is known. By probing the graphene sheet with a source drain current of 1 μA we obtain a value of $\mathrm{n}_{2D} \approx 10^{13}$ carriers cm^{-2} that is similar to the value reported in literature. However this measurement is a preliminary confirmation about the nature of the sample under measurement because the purpose of this study is the evaluation of charge carrier density differences between the unperturbed and the charged conditions of the SLG sheet. For this purpose it is necessary to follow an experimental procedure that takes into account the steps reported in Table 3.1 and whose parameters are included in the expression 3.11. With this procedure it is possible to put in relation the charge-density differences with the surface charge measured by double-step chronocoulometry. One of the step of this procedure is reported as an example in Figure 3.23.

Table 3.1. Hall voltage measurement procedure for the compensation of longitudinal components

Measurement	1	2	3	4
Electric current	→	→	←	←
Magnetic field	$\odot$	$\otimes$	$\odot$	$\otimes$
Measured voltage	$V_H + V_L$	$-V_H + V_L$	$V_H - V_L$	$-V_H - V_L$

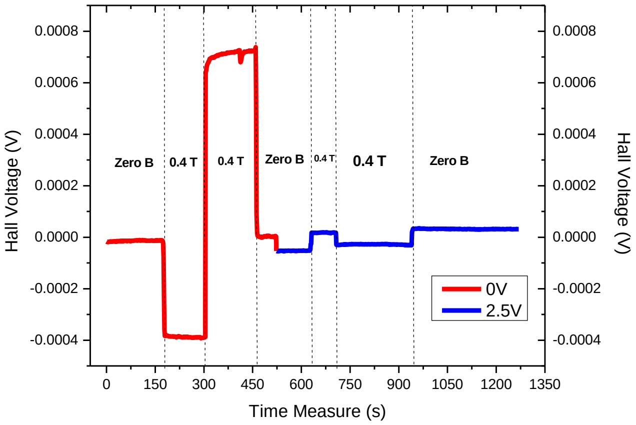

Figure 3.23. Hall voltage measurement step on the unpolarized film (red points) and on the film when 2.5V has been applied to the polymeric gate (blue points)

In the Figure 3.23 the Hall voltage is reported that is recorded continuously during the measurement under a steady magnetic field at 0.4 T. In the meanwhile, the value of magnetic field is reverted as prescribed in the third line of Table 3.1 and the corresponding values of Hall voltages can be seen as changes in different sections marked by dotted lines of Figure 3.23. The application of a voltage = 2.5 V to the PES (blue points on Figure 3.23) causes a drop of the Hall voltage that corresponds mainly to the variation of the longitudinal component: to extract the transverse component it is necessary to flip the magnetic field, as represented by the change of Hall voltage again as seen on the plot, and to repeat the whole procedure with an opposite value of the electric current. On the graph, Hall voltage jumps are labeled as $2V_{Hall}$ because the single value of Hall voltage is the difference between the value at 0 T and the one at 0.4 T. Then in this experimental set-up, we reverted the magnet to flip the magnetic field around the sample holder, as shown in Figure 3.21 : thus the output of this measurement is $2V_{Hall} = V_{Hall}(0.4\,T) - V_{Hall}(-0.4\,T)$. The labels V_H and V'_H used in the expression 3.11 correspond to the convention to report the unpolarized and the polarized conditions respectively. After repeating this procedure for several gate voltages and by comparing each measure with the corresponding value of double step chronocoulometry, it is possible to build the graph shown in Figure 3.24 for different layered graphene.

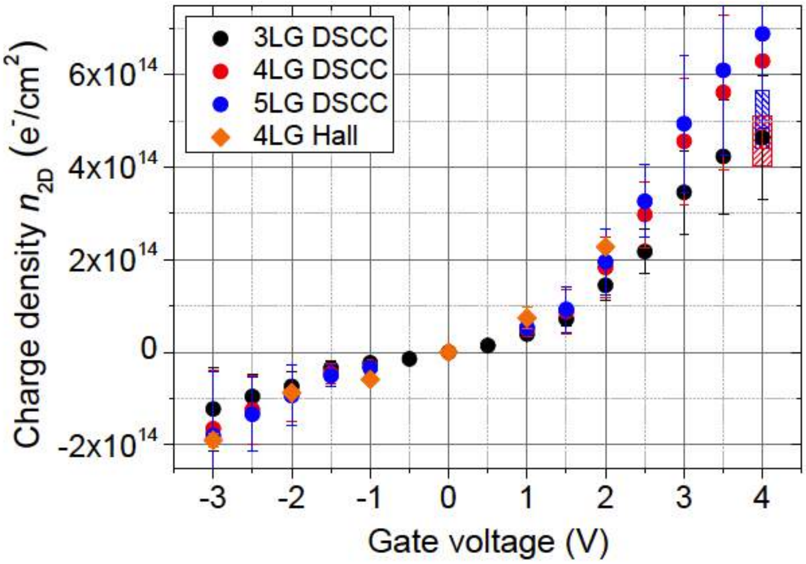

Figure 3.24. The induced charge density n_{2D} as function of the gate voltage measured by different techniques in three-, four- and five-layer graphene devices. The results of Hall effect (orange diamonds) and double step chronocoulometry measurements (black, red and blue circles) are compared. The range of n_{2D} values estimated at $V_G = 4$ V for four and five layer graphene from an ab-initio evaluation of the quantum capacitance of the devices is also shown (red and blue hatched regions).

The two series of measurements are compatible with each other: in particular it is very interesting to observe the non linear relation between gate voltage and induced charge. Usually there should be a linear relation between induced charge and gate voltage but sometimes, some non-linearities can rise because of measurement conditions or "memory-effects" from the previous polarization of the PES. In this case, the unusual behavior has been detected by the two different measurement techniques that refer to two different physical observables to measure the same quantity.

In summary the comparison of the induced charge evaluated by means of two different techniques, a classic Hall effect measurement and the new double step chronocoulometry we introduced, gives very good results, as shown in Figure 3.24 for four-layer graphene. Here, the induced charge density was measured in three layer graphene (black circles) and then the values for four and five layer graphene have been obtained by scaling the three layer graphene results with the calculated ratio of their quantum capacitance C_Q [11]. This is a possible form of further consistency check of the results shown in Figure 3.24. In fact, it is well known that in case of gating of a 2D material the EDL plus the 2D electron-liquid system can be modeled by a series of two specific capacitances: the geometric one C_g, which describes the EDL, and the quantum one, C_Q, that essentially describes the screening properties of the 2D conductor. This issue of quantum capacitance is explained in details in the forthcoming section 3.2.6. From the obtained values of C_g and C_Q we have calculated C_{EDL} and, consequently, n_{2D} for four layer graphene and five layer graphene at $V_G = 4$ V. The obtained ranges of values (including only the variability of C_g) are shown in Figure 3.24 as dashed bands (red for four and blue for five layer graphene respectively). In the range where the comparison of the three methods of n_{2D} determination is possible ($V_G \leq 2$ V) the average n_{2D} value coincides with the one obtained from double step chronocoulometry and thus we conservatively decided to use these double step chronocoulometry values in the whole V_G range including the proper error (of the order of $\pm 30\%$ at high doping) in the n_{2D} evaluation.

The fact that we can determine the induced charges through the double step chronocoulometry technique allows us to use it in all the cases for which it is impossible or very complicated to measure by the Hall effect procedure.

3.2.3 Dirac curves

Another interesting set of measurements were done on single and few layer graphene devices. A variation of R_{xx} with respect to V_G is observed upon accumulating both types of carriers, holes or electrons, within a narrow voltage range of $\Delta V_G = \pm 3V$ from the charge neutrality point. These measurements are popularly known as the Dirac curves. These experiments allow us to continuously drive the Fermi level from the valence band to the conduction band or vice versa. Figure 3.25 shows the sheet resistance R_{xx} dependence on the applied gate voltage V_G for a three layer graphene device gated with our PES.

Within a range of gate voltage $V_G = \pm 1$ V the sheet resistance is almost linear while just proceeding further, an upturn or non-monotonic behavior both for electrons and holes in R_{xx} is observed, which is attributable to the possibility of crossing the higher-energy bands present in three layer graphene. Eventually the drop in R_{xx} continues leading to a pronounced saturation at extremities when $V_G = \pm 3$ V. Moreover, it is necessary to know the value of induced sheet carrier density, n_{2D} as a function of V_G. Each type of carriers are induced as we change

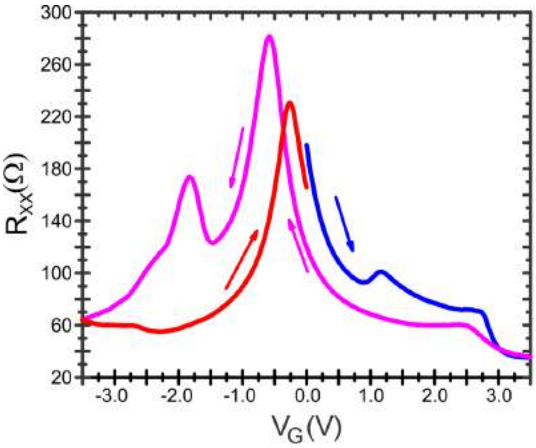

Figure 3.25. Sheet resistance, R_{xx} variation with respect to V_G for a three layer graphene device. Arrows show the direction of sweep, blue curve is followed by pink and then red. Mismatch of curves is attributed to strong hysteresis of ion dynamics.

the sign of V_G independently and has been obtained by Hall effect measurements at discrete values of applied V_G. The result of comparison is shown in section 3.2.2 alongwith other results for four layer graphene. As expected n_{2D} changes sign corresponding to the resistance maximum, confirming the shift of Fermi level, E_F across the charge neutrality point.

Since the relative size of ions forming the EDL is different, an asymmetric and hysteretic behavior is observed in practice. The difference can be clearly seen when the voltage sweep is applied first from positive to negative V_G and then vice versa as shown in Figure 3.25. This is due to the transport of ions in the PES that are able to rapidly form the two parallel plates of the capacitor with different thickness while, instead, the dissociated ions during the disruption of the EDL show a quite slower dynamics.

This slow dynamics of ions is a physical phenomenon and is a considerable disadvantage of these liquid-solid combination of geometry over the conventional transistors gated with the solid dielectrics. This observation leads to the asymmetry seen in these Dirac curves. More importantly, however, the devices gated by different PESs exhibit a fairly good agreement in the main features of the conductivity, including the absolute values, the nonmonotonic behavior, and the position of the features as a function of carrier density. This observation is important because it indicates that the features in the conductivity are intrinsic to graphene.

3.2.4 Measurement of resistance as a function of temperature and applied gate voltage

All the operations mentioned up to now are performed at room temperature in order to accumulate the maximum possible amount of charge over the surface of the samples. To study the behavior of each material in temperature, in particular, the procedure is followed by immediate cooling of the sample down to 2.7 K. This is done immediately as soon as the gate current stabilizes in order to avoid further degradation of samples due to electrochemical effects. At around the glassy transition (T = 240 K) of the polymer, the Li^+ and $TFSI^-$ mobile ions halt due to the freezing of BEMA and PEGMA fixing the accumulated charge on the two EDL plates that build in extreme proximity with the PES the PES/FLG interface. It is important to consider that the V_G must be applied at $T > T_{glass}$ and kept constant throughout the cooling down process. As regards the gate current, its small, non-vanishing value decays down to zero very smoothly on crossing the glassy transition. The sample is cooled down very carefully operating at optimal speed in order to avoid breaking of FLG flakes or contacts due to contraction of the polymer while descending down in temperature. During the warming up of each sample, the resistance $R(T)$ was again measured since this measurement is slower and, thus, more reliable. The results of these measurements are reported in Chapter 4 & 5.

3.2.5 Warnings, limitations and drawbacks of the technique

The main purpose of field-effect experiments is to exploit the properties of the nano-gap capacitor formed at the interface between the PES and the sample. For geometrical reasons, this capacitance is expected to be much larger than those associated to the solid dielectrics. Also, it is verified that we are able to induce an extra amount of charge uniformly at the surface, which creates a modification of the surface charge density from its intrinsic value thereby changing the type of doping present or even modifying its material properties. Nevertheless, polymer gating technique has few limitations and drawbacks that must be taken into consideration.

First of all there is the problem of the use of polymer gating to induce a high amount of charge at different temperatures. With polymeric gating it is necessary to polarize the EDL at room temperature and subsequently cool it down, while a solid dielectric is able to tune its charge induction even at low temperatures. Once the system is at cryogenic temperature it is not possible to tune the amount of induced charge because the ions that form the EDL are frozen in the polymeric matrix and aren't anymore sensitive to the external voltage. In Figure 3.26 it can be seen that the gate current that represents the movement of ions across the polymer matrix, approaches to zero below 250 K and it is not possible to make further electrostatic modifications.

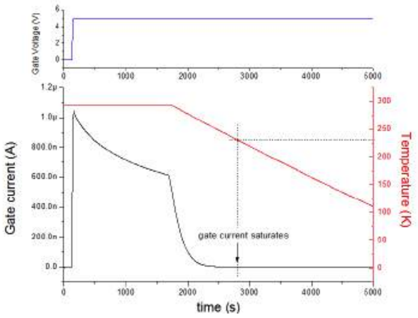

Figure 3.26. Top: Applied gate voltage; Below: Corresponding effect of the applied bias on the gate current plotted versus time at the decrease of temperature

In order to tune the induced carrier densities, it is necessary to reach again the room temperature by heating up the samples under test. In these conditions it is not possible to finely tune the amount of charge induced at low temperatures thereby making it a time consuming process. A feasible solution to this problem was proposed in Ref. [10], where the authors described double-gate technique for performing field effect experiments on atomically flat MoS_2. The double gating technique refers to a polymer gating technique combined with a standard dielectric gate from the bottom used for fine tuning the charge induction.

One of the major concerns of PES gating is related to the mechanical stability of the devices during the thermal cooling. This is an important drawback of these experiments since more than 80% of FEDs do not survive the first cooling cycle. This problem arises from the different coefficient of expansion of the PES and of the thin film under measurement, usually made of a metallic material or of graphene: the interface between these two materials is subjected to a huge mechanical stress while cooling down the system from room temperature down to cryogenic temperatures. Some precautions to reduce this problem have been introduced such a surface windowing with Polyimide resist or Kapton tape for devices with dimensions of the order of millimeters as well as a spin-coated window with Poly(methyl methacrylate) (PMMA) for smaller devices. However, often, this is not enough against the polymer capability of peeling the surface of the sample because of its thermal contraction. A solution that has not been investigated yet could be the deposition of the PES by spin coating: in this way it should be possible to control the gate geometry and avoid the configurations able to favor the polymer cracking and peeling. Another possible solution could be the modification of polymer's formulation in order to make its coefficient of expansion more similar to that of the substrate. As an example, a silicon-based polymer could have a coefficient of expansion more similar to the one of the substrate (usually made by a silicon oxide surface). However a change of polymer's formulation may lead to a lower charge-induction efficiency.

Another drawback of polymeric gating technique is the aging of the polymer: the performance of a FED depends on its previous utilization. This behavior can be observed in Figure 2.11 of section 2.3 where a series of induced surface charge densities n_{2D} are potted as a function of gate voltage. In the main graph of Figure 2.11 , values of surface charge density are reported from several devices fabricated with different metals: silver, copper and gold. It seems an incongruity that the same surface charge density is obtained on gold for different gate voltages (between 1.5 and 3 V, for example) or even a lower induction is obtained for higher voltages. A simple explanation of this behavior comes from the inset of Figure 2.11 where it is shown that for any gate voltage, charge induction is maximum at the first application and subsequently decreases at the increase of the number of applications. Since the PES is very stable over a long time, this behavior might be rather ascribed to a sort of memory effect, an effect that is compatible with a possible loss of Li ions at the interface with the electrodes that limits the magnitude of the EDL and consequently the performances of the FEDs.

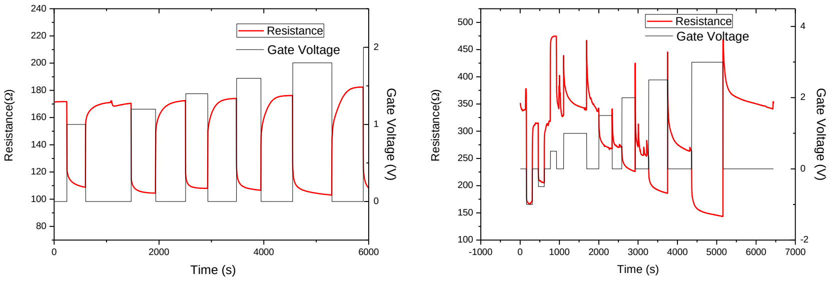

Figure 3.27. Resistance behavior with respect to applied bias for a three layer graphene under PES a) Reversible process (field-effect) b) Irreversible process (chemical interactions). Black line represents the gate voltage and red line the value of resistance

Another important point of concern is the chemical interaction between the PES and the sample. It is always necessary to check for this phenomenon in order to be sure that the change in physical properties is due to only the variation of the charge density. In fact, chemical reactions at the interface can lead to modifications of transport properties as well as variations of the charge density itself. For noble metals such as gold and inert materials, field effect is expected to be free from chemical reactions at the surface.

Preliminary measurements were made to control the reversibility of changes in resistance on applying gate voltage and the corresponding change on removal of the applied gate voltage. In the case when the resistance reverts back to the base value, then the change in resistance is ascribed to electrostatic induction of charges, however if on removal of voltage, the resistance does not revert then it is a clear case of occurrence by a chemical interaction process (Figure 3.27). In addition a very appropriate technique that can be employed to set the limit of the applied gate voltage that produces a reversible change in resistance is the cyclic voltammetry. It helps in defining an electrochemical stability window exceeding which irreversible changes in resistances on application of gate voltage are produced.

Cyclic voltammetry is a potentiodynamic electrochemical measurement based on the observation of the current flowing across the polymer-electrode interface. The electrode is composed by the material whose chemical interaction has to be investigated for field-effect purposes, an inert counter-electrode is used to close the circuit and the polymer is sandwiched between the two electrodes. This system is polarized with a linear potential ramp that is inverted when a set point is reached: when the potential reaches zero again, the procedure is repeated for subsequent cycles. Current values measured during this cyclic polarization are compared for increasing and decreasing potentials and for each cycle: irreversibility of the process appears as a decrease of the amplitude of current peaks for each cycle. The output of this kind of measurements is a current vs potential plot (Figure 3.28). This technique has been used to investigate a possible chemical interaction between lithium ions dissolved in the gating polymer and lead or lead-indium surface of superconductive devices. Cyclic voltammograms reported in Figure 3.28 show a widely different behavior for pure lead and lead-indium alloy: Figure 3.28 (b) is a zoom of Figure 3.28 (a) since the heights of the peaks of anodic and cathodic current are two order of magnitude bigger for lead compared to lead-indium alloy. The interaction between lithium ions dissolved in the liquid electrolyte solution and the working electrode is very little for lead-indium and the absolute values of negative and positive currents are comparable for each cycle as shown in Figure 3.28. This is a sign that no irreversible reactions are occurring between lithium and lead-indium alloy or that indium is limiting this interaction that is instead very big for pure lead, as appears in Figure 3.28. With this information in hand and experience of electrochemical gating on FLG we have set the limits of electrochemical stability window at $V_G = \pm 3\ V$.

3.2.6 Limitations due to quantum capacitance in graphene

As briefly mentioned in the previous Chapter 2, section 2.4.1 a high carrier density is expected to be attained with an ionic-liquid gate or a polymeric gate, but quantum capacitance, C_Q is the physical quantity that limits this charge induction. The high carrier density is expected to be so because of the thin EDL, i.e., the large geometrical capacitance determined by $C_g = \epsilon_{IL}\epsilon_0/d$. Here, ϵ_{IL}, ϵ_0

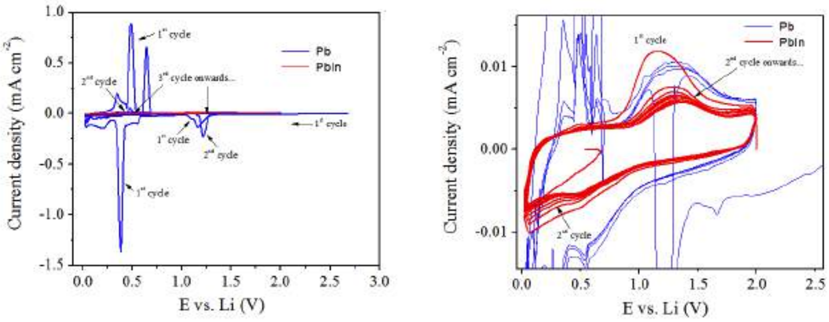

Figure 3.28. a) Cyclic voltammogram for pure lead (blue line) and lead-indium alloy (red line). b) Zoom of the cyclic voltammogram

and d are the relative permittivity of the ionic liquid, vacuum permittivity, and thickness of EDL, respectively [11]. However, carrier doping into SLG with ionic liquids is much lower than expected because the potential difference between an ionic liquid and SLG turns out to be smaller than the applied gate voltage V_G due to the shift of the Fermi energy E_F when one dopes SLG with an additional charge Q. This phenomenon is due to the quantum capacitance C_Q, defined as $C_Q = eQ/E_F = e^2D(E_F)$, which is connected to C_g in series. Thus, the total capacitance C_{EDL} between the ionic liquid and SLG is:

$$1/C_{EDL} = 1/C_g + 1/C_Q \tag{3.12}$$

The geometrical capacitance C_g depends on the properties of the PES and on V_G and can be determined from our gating experiments in Au thin films [6] where, of course, $C_Q \to \infty$. At $V_G = 4\ V$ it turns out to be in the range $50 - 140\ \mu F cm^{-2}$ depending on the "freshness" of the PES [10]. The quantum capacitance C_Q of our devices have been estimated from tight-binding and ab-initio DFT calculations (jellium model) of the effective electron mass m^* of the FLG flakes at the different charge dopings [12] by using the original definition of C_Q derived by [13].

$$C_Q = \frac{g_v m^* e^2}{\pi \hbar^2} \tag{3.13}$$

where g_v is the valley degeneracy factor. At $V_G = 4$ V, for example, we estimate $C_Q = 24 \pm 7$ and $27 \pm 8\ \mu\text{Fcm}^{-2}$ for four and five layer graphene, respectively, in good agreement with the values measured in three layer graphene at high charge doping [7].

Thus, the effect of C_Q dominates the total capacitance, C_{EDL} when its value is small and this is the case only in the two following conditions a) if the dielectric gate is very thin and b) number of layers, n in graphene systems, remains less than

4 [11]. Since here t_{ox} is small, the quantum capacitance, C_Q dominates the ratio because it is connected in series with C_g. Since density of states increases with increasing n, accordingly C_Q increases thereby limiting carrier density. Ref. [11] reports that at $n = 1$, a minimum C_{EDL} is observed but with increasing n, C_{EDL} increases until $n = 4$ and saturates further until n approaches 10. Thus in view to exploit the superior characteristics of graphene-based devices, therefore, it is of significance to elucidate the optimal n producing both the large C_{EDL} and specific surface area.

Bibliography

[1] Blake P., K.S. Novoselov, A.H. Castro Neto, D. Jiang, R. Yang, T.J. Booth, A.K. Geim, and E.W. Hill. Making graphene visible. *Applied Physics Letters*, 91:063124, 2007.

[2] Eugene Hecht. *Optics*, *4th edition*. Adelphi University, 2001.

[3] JC Nabity Lithography Systems, Bozeman, MT 59717 USA, Tel: (406) 587 0848.

[4] http://www.nanofacility.it

[5] Jijeesh R Nair, C Gerbaldi, M Destro, R Bongiovanni, and N Penazzi. Methacrylic-based solid polymer electrolyte membranes for lithium-based batteries by a rapid uv-curing process. *Reactive and Functional Polymers*, 71(4):409-416, 2011.

[6] D. Daghero, F. Paolucci, A. Sola, M. Tortello, G.A. Ummarino, M. Agosto, R.S. Gonnelli, Large conductance modulation of gold thin films by huge charge injection via electrochemical gating, *Phys. Rev. Lett.*, 108, 066807, 2012.

[7] Jianting Ye, Monica F. Craciun, Mikito Koshino, Saverio Russo, Seiji Inoue, Hongtao Yuan, Hidekazu Shimotani, Alberto F. Morpurgo, and Yoshihiro Iwasa, *PNAS*, 108, 32, 13002-13006, 2011.

[8] G. Inzelt, in Electroanalytical Methods: Guide to Experiments and Applications, edited by F. Scholz ($Springer-Verlag$, Berlin, 2010), p. 147.

[9] A Alan Maxwell Bond and Fritz Scholz. Electroanalytical methods: guide to experiments and applications. *Springer*, 2010.

[10] Jianting Ye, Y. Zhang, R. Akashi, M.S. Bahramy, R. Arita, and Y. Iwasa. Superconducting dome in a gate-tuned band insulator. *Science*, 338(6111):1193-1196, 2012.

[11] E. Uesugi, H. Goto, R. Eguchi, A. Fujiwara and Y. Kubozono. Electric double-layer capacitance between an ionic liquid and few-layer graphene. *Scientific Reports*, 3:1595, DOI:10.1038/srep01595, 2013.

[12] Galasso S., Cappelluti E. and Piatti E., unpublished.

[13] Luryi S., Quantum capacitance devices, *Appl. Phys. Lett.* 52, 501?503, 1988.

Part II

Results and Discussions

Chapter 4

Electrochemical gating and weak localization in few layer graphene

After all the necessary checks and precautions such as the resistance reversibility check to avoid chemical interaction, measurements of cyclic voltammetry to establish the limits of the electrochemical stability window, validation of the methods for the determination of the induced charge etc., here we report our results of transport measurements performed at room and cryogenic temperatures. The results of this chapter are described with regard to our measurements on FLGs, mainly three, four and five layers gated with our specialized PES.

4.1 Device structure and geometry

The detailed fabrication and geometry of FLG-FEDs have been discussed in details in Chapter 3 section 3.1. The devices were always prepared in a planar configuration as shown in Figure 4.1 (left). FLG flakes are deposited on a 285 nm thick SiO_2 on Si substrates by adhesive tape exfoliation of natural graphite. Then, the samples are analyzed by optical microscopy, in order to estimate the number of graphene layers composing the deposited thin flakes. The geometry of the contacts is defined using photolithography followed by Cr/Au (5 nm/60 nm) thermal evaporation and lift-off. The Hall bar geometry is defined by creating a photoresist (PR) mask by photolithography and etching the uncovered portion of the film by O_2/Ar reactive ion etching. A further layer of PR is then spun on the sample and windows are open by photolithography only on the FLG channel and the contact pads for device wire bonding and mounting. The PR mask is then hard-baked at 145°C for five minutes in order to improve its chemical stability. These FEDs have current contacts labelled as I^+ (source) and I^- (drain) and voltage contacts that are patterned in a Hall bar configuration. Since there can be different choices of gate, as shown here, we opted for a configuration in which a *Pt* wire is placed inside the PES and the gate voltage is applied through it. In Figure 4.1 (right) we show the general schematic of the way the FLG channel was connected electrically.

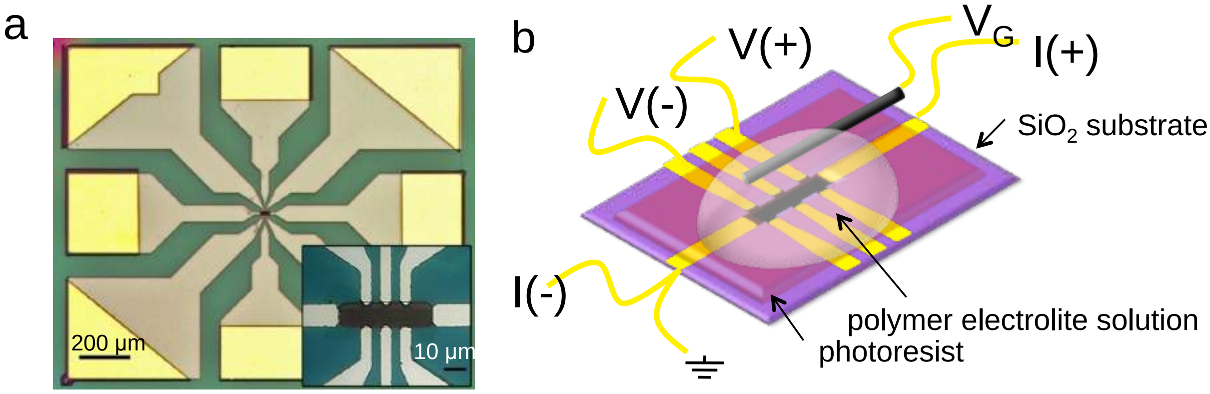

Figure 4.1. (a) An optical micrograph of a three layer graphene device used in experiments; (b) Scheme of FEDs with patterned contacts, Pt wire gate pad and electrical connections.[23]

4.2 Dirac curves

As described before, Dirac curves refers to the sheet resistance (or conductance) behavior with respect to the continuously applied gate voltage; these measurements are swept across the Dirac point in FLG.

In the ideal conditions the Dirac point and the charge neutrality point coincide, however in real devices a shift in the Fermi energy occurs spontaneously due to adsorbed water molecules over the surface and trapped charges both at the PES/FLG and FLG/substrate interfaces. A variety of strategies have been previously employed to induce additional charges over the surface [1, 2]. Out of all of those, electrically induced surface doping without involvement of solid gate has so far proven to be the one able to achieve the highest charge induction in the material under study. Figure 4.2 (b) shows the sheet resistance, R_{xx} dependence on the continuously applied gate voltage V_G for a three-layered graphene device using the PES gating technique. An inverse linear variation (the ambipolar electric field effect) of R_{xx} with respect to applied V_G was observed upon accumulating either type of the carriers, holes or electrons, within a narrow voltage regime of $\Delta V_G = \pm 1$ V from the Dirac point. This enabled the possibility to continuously drive the Fermi level, E_F from the valence band to the conduction band or vice versa. In section 1.2.2 we described the band structure of different FLGs, particularly Figure 1.19

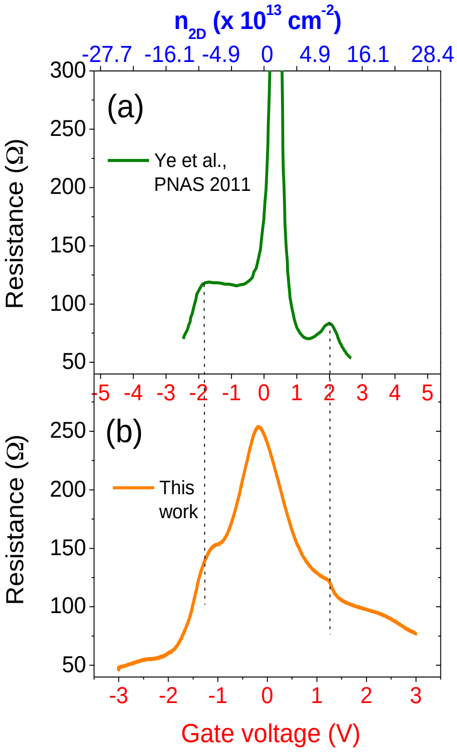

Figure 4.2. Comparison of the Dirac curves on three layered graphene devices plotted with respect to applied gate voltage V_G and sheet carrier density, n_{2D}; (a) results from Ref. [3] where the devices were gated with ABIM+TFSI ionic liquid; (b) our work, where devices are gated with BEMA+PEGMA+ LiTFSI as PES. Our configuration of PES is very well able to access a higher range of surface charge carrier densities and cross higher energy band edges in three layer graphene.

showed the electronic band structure of three layer graphene. Further continuation of the sweep at higher gate voltage leads to crossing of the split-off bands away from the Dirac point, thereby inducing sharp non-monotonicities in the resistance curves. For example, these depressions or non-monotonicities have been related to the crossing of a Van Hove singularity (VHS) when the Fermi level reaches the split band T_{2g} [3].

The position of these upturns is univocally associated with a specific charge density such that the Fermi level is able to cross the bottom of the split-off bands, and can thus be exploited to obtain a voltage-charge density calibration (Figure 4.2). Note also that our choice of the electrolyte allows us to reach the split-off bands at smaller voltages with respect to the ionic liquid employed in Ref.

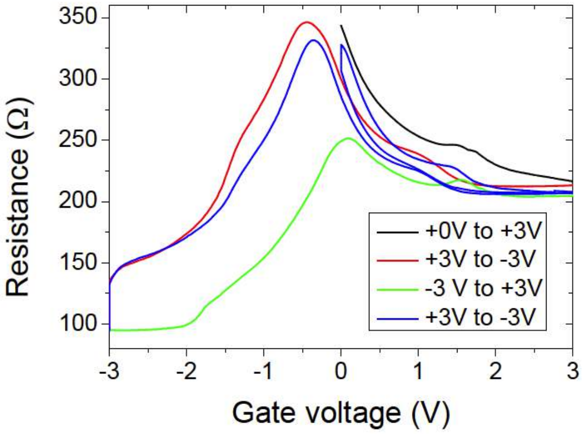

Figure 4.3. Dirac curves for a four layer graphene

[3], thus supporting higher charge induction capabilities for our configuration of PES. Eventually the drop in R_{xx} continues leading to a pronounced saturation at extremities when $V_G = \pm 3$ V. The behavior of R_{xx} is more properly represented as a function of the sheet carrier density, n_{2D}. In order to do so n_{2D} has been determined by single shot V_G application experiments and deduced by double step chronocoulometry (Figure 4.2). As expected n_{2D} changed sign corresponding to the resistance maximum, confirming the shift of E_F across the charge neutrality point. Also it was verified that the *order of magnitude* of charge carriers added to the system was the same for double step chronocoulomtery as well as Hall effect measurements as shown in Figure 3.24 for a four layer graphene device.

Figure 4.3 also shows the Dirac curves as we measured for a four layered graphene device. These curves show the hysteretic behavior as well as a non-monotonic behavior around $V_G = 2$ V that depicts the crossing of the higher energy split-off bands (shown in Figure 1.20) similar to those observed in the Dirac curve of three layer graphene.

4.3 Sheet R vs. T measurements: intermediate T range and electron electron scattering

All the aforementioned operations were performed at room temperature but now we report the results as a function of temperature. After drop casting, UV curing the PES and applying the gate voltage, measurements proceeded by an immediate cooling of the samples, in order to avoid any degradation of the sample due to electrochemical effects. The sample's four-wire resistance was explored in the range $4 - 290$ K as a function of both the number of layers and the induced charge density. In each measurement, the gate voltage was set at room temperature and the sample was subsequently brought down to the cryocooler's base temperature. The measurements were performed on three-, four- and five-layer graphene devices. The stacking sequence was Bernal for all the FLG devices used in these experiments. The samples were cooled down very carefully operating at optimal speed in order to avoid breaking of FLG or contacts due to the mechanical stress induced by thermal dilatation mismatch between the sample and the PES. Due to the previous remarks, the induced charge carrier densities are neither expected to vary significantly over time after the glass transition nor when the sample is warmed up again to the room temperature. Around the glass transition temperature ($T_{glass} \approx 240$ K) of the polymer, the Li^+ and $TFSI^-$ mobile ions freeze in their set configuration thereby fixing the accumulated charge in the two EDL plates.

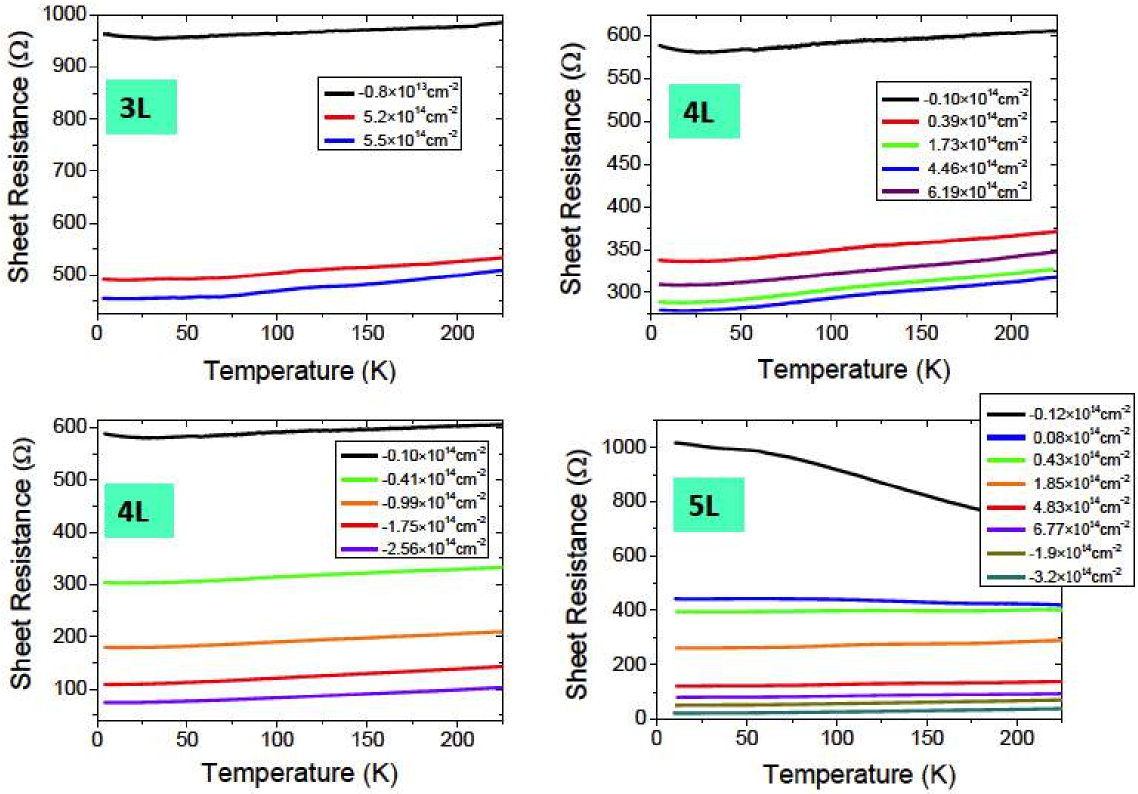

Figure 4.4. Raw data of sheet resistance vs. temperature at different induced charge densities for respective FLG.[23]

This was revealed by the sudden reduction to zero of the gate current due to ion diffusion upon crossing the glass transition temperature itself (Figure 3.26), and by the impossibility to further induce any current change by applying different voltages. Thus, the desired gate voltage V_G must be applied at $T > T_{glass}$ and kept constant throughout the cooling process.

Measurements were repeated as the samples were allowed to spontaneously heat up upon switching off the compressor of cryocooler: this allowed us to avoid the thermal fluctuations associated with the cryocooler's cool down cycles. We report the results of these measurements in Figure 4.4. Using the raw data presented in the Figure 4.4 we analyzed the behavior of the resistance at different temperature regimes.

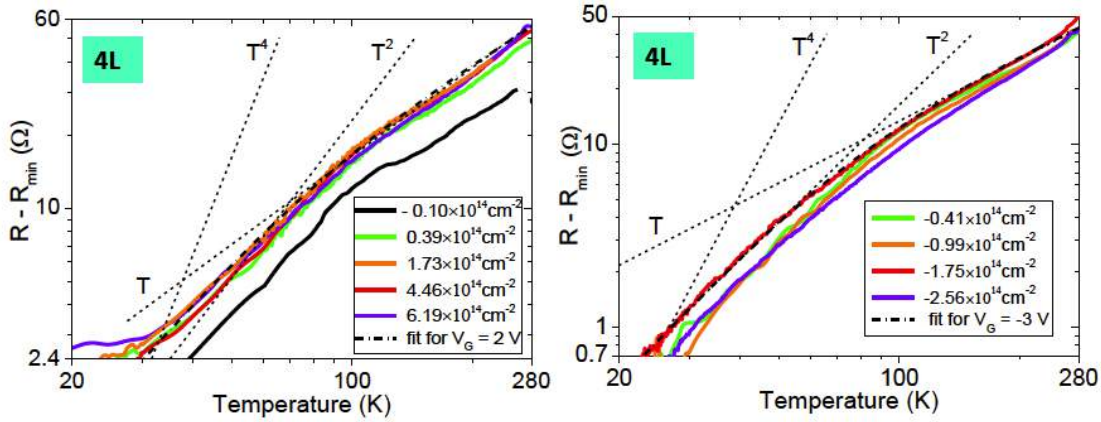

Figure 4.5. The temperature dependent part of the resistance scales as T^2 in the intermediate temperature range and smoothly crosses over into a linear T dependence at higher temperatures almost in each case. The dashed lines represent fits to T^4 dependency (shown here only for comparison with linear T and T^2 fits) for our experimentally obtained data of four layer graphene samples (left corresponds to positive charge induction while right to the negative charge induction)[23]

The low temperature range always showed a logarithmic upturn in the resistance (the metallic regime) and we interpret this as the characteristic weak localization behavior which will be addressed in the next section. Here we focus on the intermediate range of temperature, i.e. 20 K $< T <$ 280 K. When the resistances are in the complete metallic regime (any V_G for three and four layer graphene, $V_G \geq 2$ V, i.e. $n_{2D} \geq 1.85 \times 10^{14}$ cm^{-2} for five layer graphene) they show a linear behavior as a function of temperature in the range between about 100 K and 270 K. The slope of this high-temperature linear-T dependence practically does not change at the increase of the charge density n_{2D} (both positive and negative) as it can be seen from the curves of Figure 4.4 and has been already observed in SLG [13]. Below $\sim$ 100 K the curves change behavior assuming a steeper T dependence that is appreciable in the curves of Figure 4.4 (a), (b) and (c), but is also present (even if not visible due to the different scale) in the curves of Figure 4.4 (d). The standard way to get more information on the temperature dependence of the resistance curves is to plot them in a double logarithmic scale. Figure 4.5 shows an example of these $\log(R - R_{min})$ vs. log T curves (R_{min} being the extrapolated sheet resistance without the contribution of the logarithmic upturn observed at T <20 K at T tend to zero) in the case of the four layer graphene device and in the temperature range 20-280 K for both positive (panel a) and negative (panel b) charge induction. In both cases a linear T dependence is observed at T $\gtrsim$ 100 K. Below $\sim$ 80 K the temperature dependence becomes steeper, showing a dominant T^2 component (see Figure 4.5 (b)).

As a matter of fact the best fit of the sheet resistance in the temperature range 30-80 K is always obtained by a function $AT + BT^2$ where the quadratic term is more or less dominant. In the intermediate temperature range (70 K $\leq T \leq$ 100 K) we see a rather sharp (at least for positive gating, i.e. electron doping) crossover between the two regimes. These results have been reproducibly observed also in the three and five layer graphene devices (Figure 4.6).

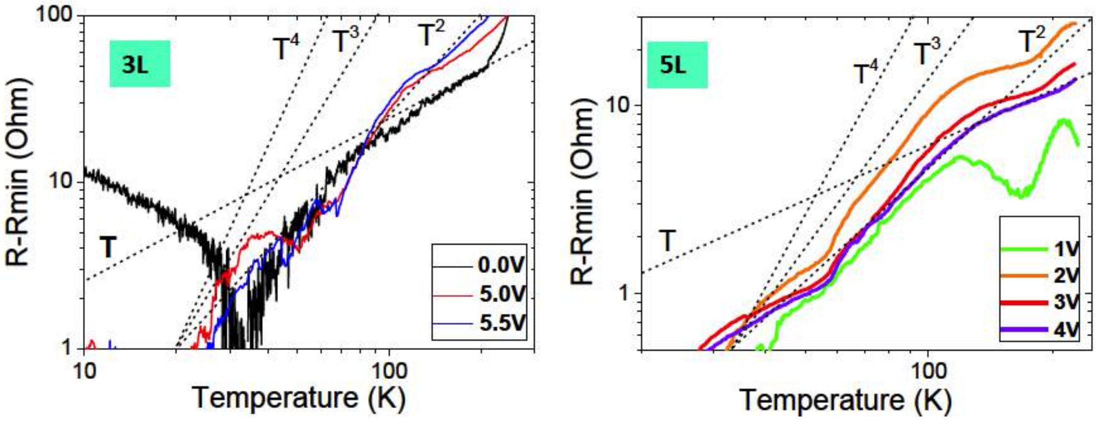

Figure 4.6. The temperature dependent part of the resistance in the intermediate temperature range for our experimentally obtained data of three (left) and five (right) layer graphene samples.[23]

They are somehow unexpected since a "classic" small-angle electron-phonon scattering should dominate the sheet resistance below the Bloch-Grüneisen temperature Θ_{BG} in a low-density electron system. This should lead to the well-known T^5 dependence in the 3D case and to a T^4 dependence in the 2D one, as theoretically predicted [12] and experimentally observed in SLG [13]. However, in our case, it is clearly impossible to fit the experimental data with a T^4 dependence (shown, as reference, in both the panels of Figure 4.5 and 4.6). The most straightforward explanation is that in our conditions (FLG samples immersed in the PES) the intermediate- and low-temperature sheet resistance is dominated by electron-electron collisions with both small momentum transfer (Nyquist term, $R \propto T$) and with large momentum transfer (direct ballistic term, $R \propto T^2$). The weight of the quadratic component varies with the number of graphene layers and the sign of doping, but, in any case, it becomes smaller at T < 20-35 K (see Figure 4.5 (a)) and the Nyquist term finally becomes dominant at temperatures below 15 K.

As far as the crossover to the high-temperature linear T dependence is concerned we can simply note that, independently from the value and the sign of the induced charge density, it always occurs at a temperature very close to the one where a similar crossover (but from a T^4 to a T behavior) has been observed in SLG at $n_{2D} > 4.65\times 10^{13}$ cm^{-2} (see Figure 2 of Ref. [13]). This temperature cannot be associated to the Debye temperature Θ_D of the material since it should be higher than 2000 K ($\Theta_D \approx 2300$ K in SLG [13] and $\Theta_D \approx 2500\ K$ for in-plane phonon modes of graphite) thus potentially leading to a crossover at $T > 400\ K$ ($\sim 0.2\ \Theta_D$). Following Ref. [13] it is thus tempting to interpret also in our case this crossover temperature as related to the Bloch-Grüneisen temperature Θ_{BG} of the FLGs at our high doping levels. In a simple, single-band and free-electron-like picture Θ_{BG} is the temperature at which the maximum momentum of acoustic phonons equals twice the Fermi momentum and is therefore able to completely span the Fermi surface. In this ideal case Θ_{BG} is given by:

$$\Theta_{BG} = \frac{2\hbar k_F v_S}{k_B} \tag{4.1}$$

where k_F is the Fermi wave vector of the spherical (or cylindrical) Fermi surface and v_S is the sound velocity. We fitted our sheet resistance curves by using a generalized Bloch-Grüneisen model similar to the one introduced in Ref. [12], but with the low-T exponent left as a parameter, i.e. by the function:

$$\Delta R(T) = R(T) - R_{min} = A \int_0^1 \left(\frac{\Theta_{BG}}{T} x^m \sqrt{1-x^2} e^{\frac{\Theta_{BG}}{T}x}\right)/(e^{\frac{\Theta_{BG}}{T}x} - 1)^2 dx \tag{4.2}$$

where A, m and Θ_{BG} are free parameters. Two examples of these fits, corresponding to the electron densities $n_{2D} = 1.73\times 10^{14}$ cm^{-2} and $n_{2D} = -1.75\times 10^{14}$ cm^{-2} are shown as dash-dot curves in Figure 4.5 (a) and (b), respectively. In the fits of all the curves of Figure 4.5 (a) and (b) (not shown here for clarity) the m parameter is 1.85 for electron doping (Figure 4.5 (a)) and ranges between 2.1 and 2.5 for hole doping (Figure 4.5 (b)).

The crossover temperature practically does not change at the increase of doping (for example from 0.39×10^{14} cm^{-2} to 6.19 10^{14} cm^{-2} as shown in Figure 4.5 (a)) and thus, if our interpretation is true, also Θ_{BG} obtained from the fit should remain almost constant at the different charge densities. Actually the Θ_{BG} values obtained from the fits of curves of Figure 4.5 range between 350 and 400 K for electron doping and between 350 and 430 K for hole doping without showing any trend as a function of n_{2D}. We obtained quite similar results in three and five layer graphene devices. At a first and superficial analysis in the framework of equation 4.2, since any k_F in FLGs increases at the increase of doping (even if not proportionally to $\sqrt{n_{2D}}$ as in SLG), the absence of Θ_{BG} tuning with the Fermi energy could be related to a reduction of the sound velocity produced by the strong charge doping. As a matter of fact a similar effect of tuning of the phonon dispersion relations with a decrease of the sound velocity of some acoustic modes (and consequent softening of the corresponding part of the phonon spectrum) has been already predicted in SLG at a very high level of charge doping [21]. Even though this effect could be present in FLGs, the situation here is quite more complex. First of all the FLG flakes with Bernal stacking are always a multiband electron system. For example, even at low electron doping (when E_F is tens of meV above the neutrality point) the four layer graphene is a two-band material with a Fermi surface made of two sheets and with two Fermi wave vectors that strongly depend on the direction in the k space. The situation becomes even more complex at the increase of the electron charge density. When $E_F \sim 230$ meV (with respect to the neutrality point) a third band crosses the Fermi level and a fourth does the same at $E_F \sim 600$ meV. These Fermi energy shifts are certainly compatible with the large electron densities obtained with our PES gating. In addition, in the presence of several bands, not only intraband scattering processes but also interband ones are possible, thus considerably complicating the picture. As a consequence, in contrast with the case of SLG, in FLGs equation 4.2 cannot be used anymore as a definition of Θ_{BG}. In this case, the constancy of the crossover temperature might arise from the interplay between the increase of the number and of the overall size of the FLG Fermi surfaces (at the increase of electron doping) and the presence of interband scattering processes. A quite similar situation can occur in the presence of a large hole doping. Only first-principles DFT calculations of the electron-phonon interaction accompanied by a semi-analytical solution of the Boltzmann equation in FLGs (as the one recently appeared in literature for MLG [22]) will clarify the causes of this crossover invariance.

4.4 Sheet R vs. T measurements: low T range and weak localization regime

After the above analysis, we plotted the normalized resistance as a function of temperature with the view point to observe increasing trend of metallicity in our

FLG samples. Hence, in the following we report the temperature dependent electron transport in FLG systems at different induced carrier densities, n_{2D} as tuned by V_G highlighting that it is possible to adjust its value up to 6×10^{14} cm^{-2} at $V_G = 3$V. Different FLG systems evidently exhibit different properties. As we have already discussed in the previous section, three- and four-layer graphene devices always exhibited an increasing resistance vs. temperature behavior, thus showing metallic characteristics even at the lowest charge carrier densities. The effect of any variation on the latter was limited to a modulation of the resistance value, strengthening the metallic behavior of the material for both positive and negative gate voltages (Figure 4.7 and 4.8 respectively).

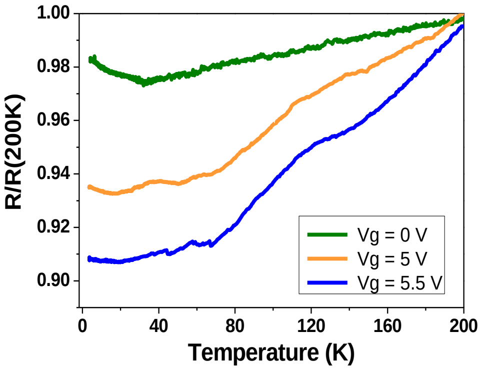

Figure 4.7. Normalized resistance behavior in temperature at different gate voltages for a three layered graphene device

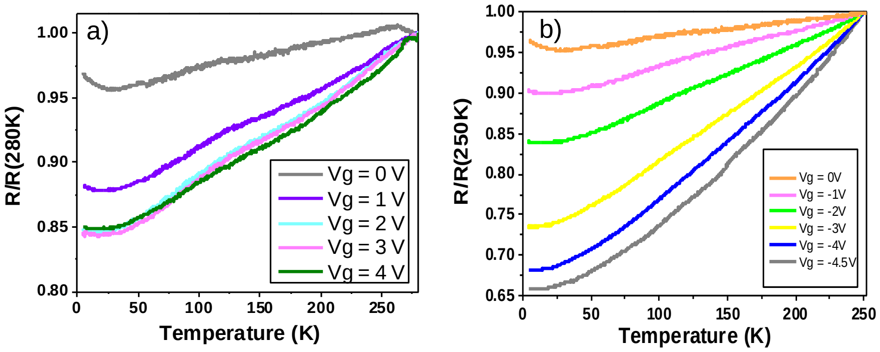

Figure 4.8. Normalized resistance vs temperature variation for a four layer device as a function of a) positive and b) negative applied V_G

At positive $V_G = 2$V, 3V and 4V, in the four layer graphene device the effect became less pronounced. For negative V_G, we observed a very well defined progression with a continuous increase of the metallic trend. In all the cases the most interesting observation regards the presence of a logarithmic increase of R(T) at $T < 20 - 30$ K, that we will soon demonstrate to be due to a carrier localization effect.

Figure 4.9 shows the temperature dependence of the normalized resistance as a function of temperature, at different gate voltages for a five-layered device; R(T) decreases as the temperature increases at $V_G = 0$V, exhibiting typical semiconducting-like localization behavior. Under the influence of applied V_G even at $V_G = 0.5$V the material shows a marked reduction in R(T) and exhibits less pronounced semiconducting like trend. Further decrease of semiconducting behavior leading to a gradual increase of resistance with temperature and thus corresponding to a crossover to a metallic-like behavior was observed by increasing V_G from 2V to 4V. This has also been observed with application of V_G = -3V and -4V.

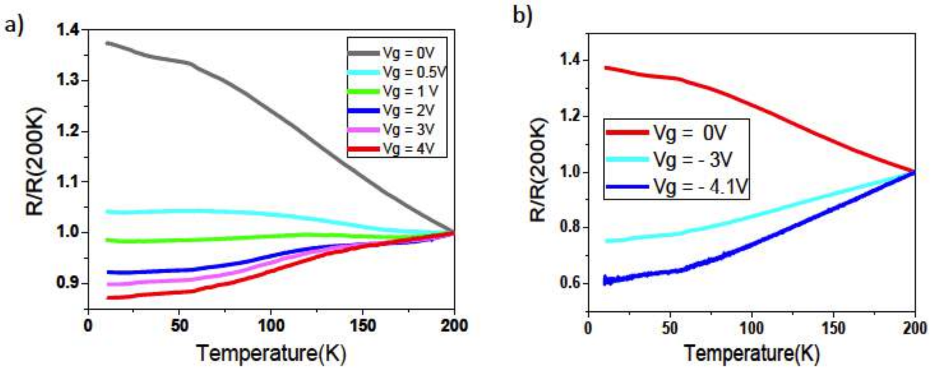

Figure 4.9. Semiconducting- to metallic-like resistance (normalized) behavior in temperature at different applied gate voltages for a five-layered graphene device

As we make a closer look at lower temperatures by using a semi-logarithmic plot as shown in Figure 4.10, a logarithmic upturn in FLG resistance was consistently observed. Both the upturn intensity and the temperature at which this upturn starts depended on charge density as well as on the number of graphene layers.

Similar logarithmic upturns in the resistance of metallic materials are well known to be caused by either Kondo effect, weak localization (WL), electron-electron interactions (EEI) or a combination of these effects. We must therefore discriminate between these possibilities.

Kondo effect is caused by carrier scattering by diluted magnetic impurities. Unlike other authors [4] we do not intentionally introduce any defects in our samples; furthermore, Raman spectra acquired on our devices both before and after

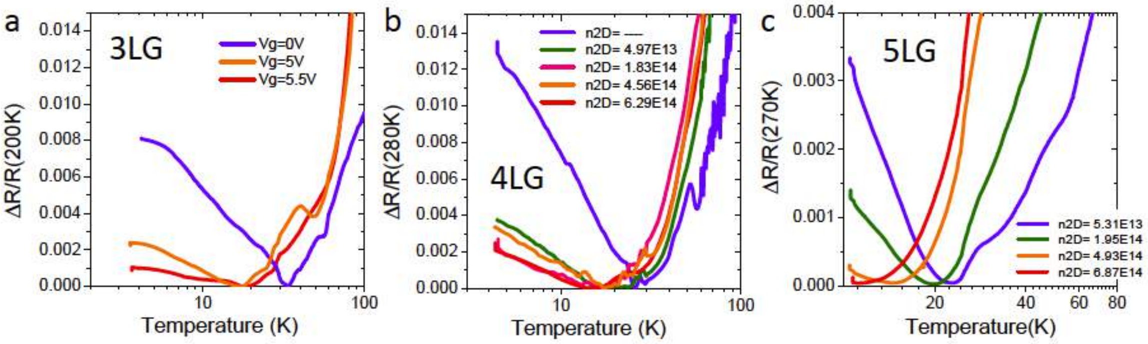

Figure 4.10. Linear resistance behavior plotted in logarithm of temperature for different FLG devices at different applied gate voltages/induced charge densities

the PES deposition showed no appreciable *D* peak (Figure 3.2), thus strongly supporting the absence of any relevant defects in our samples. We thus discard the possibility of a contribution from Kondo effect to the resistance upturn.

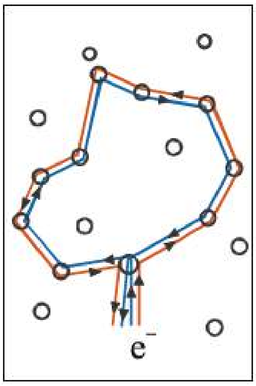

Figure 4.11. The trajectories of an electron scattered by impurities that give rise to the quantum correction to the conductance called Weak Localization (WL)

WL is caused by quantum mechanical interference between carrier wave functions upon elastic scattering: two electrons that elastically scatter clockwise and counterclockwise in the same closed loop interfere constructively, leading to an increase in the back scattering probability and thus the material resistance (Figure 4.11). Since phase coherence must be maintained throughout the entire closed loop in order for WL to occur, obviously WL is suppressed by the increased inelastic scattering probability associated with the temperature increase.

WL is suppressed as well by the application of a magnetic field, due to the time-reversal symmetry breaking between the clockwise and counterclockwise loops generated by the magnetic field. EEI, on the other hand, does not suffer from such a magnetic field suppression.

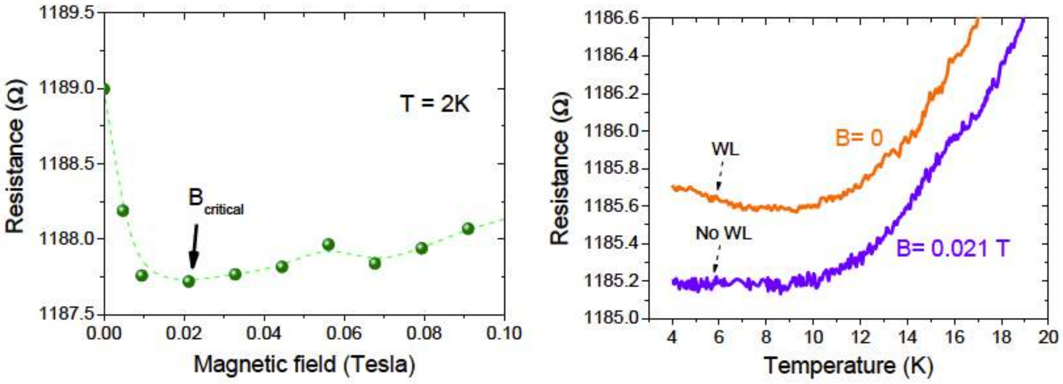

Figure 4.12. (Left) Resistance (R) as a function of magnetic field (B) for a three layer ABC stacked graphene measured in order to distinguish between WL and EEI effects; upturn in resistance gets suppressed at a critical magnetic field, $B_{critical}$=0.021 T; (Right) R vs T experiments were done again to observe the effect on R at fixed $B_{critical}$: no upturn in R; at $B = 0$: the upturn reappears.

A widely exploited solution to discriminate between the two effects is thus to measure the sample's magnetoresistance: a positive magnetoresistance is associated with weak antilocalization (WAL); a null magnetoresistance with EEI; a negative magnetoresistance with WL.

Thus, we performed magnetoresistance measurements in a helium cryostat. An ABC-stacked three-layer graphene device was probed experimentally at constant temperature of 2 K and found to have negative magnetoresistance; symmetrically, the logarithmic upturn of the resistance with decreasing temperature was found to be suppressed upon the application of a critical magnetic field=$B_{critical}$=0.021 T as seen in Figure 4.12 (right). These results strongly support the conclusion that, in FLG samples, only WL is the source of the measured resistance behavior at low temperatures. In order to completely rule out the contribution from EEI, we also measured the device resistance while heating up the sample under $B = B_{critical}$: the logarithmic upturn was found to be completely suppressed within the noise level, and this suppression was entirely reversible upon removal of the magnetic field.

4.4.1 Theoretical analysis of weak localization within the framework of models specific to graphene

With these results in the hands we tried to fit our experimentally obtained data within the framework of graphene specific models as reported in the literature. In the following we present a complete description of the theoretical interpretation corresponding to our experimental results. Since the band structure for single- and bi-layer graphenes is completely different from standard 2D materials, to the charge carriers have been attributed Berry phases of π and 2π, respectively. In realistic devices, due to the Berry phase analysis, disordered SLG is expected to display WAL and bilayer graphene to exhibit standard WL behavior. In the high charge carrier density region, the trigonal warping, i.e. imperfect shape of the Dirac cones in the band structure, tends to suppress the respective WAL in SLG and WL in bilayer graphene systems. However in the low density regime the same effect of suppression is caused by weak disorder like ripples and dislocations although at the same time enhances the intervalley scattering of the electrons. As a consequence, WL effect is restored by intervalley scattering so that the electrons in a graphene sheet tend to localize. The cumulative effect of all these factors is described by relaxation rate, τ_*^{-1} introduced in the following. Thus for finite intervalley scattering rate, $\tau_i^{-1} << \tau_*^{-1}$ and long phase coherence time $\tau_\phi > \tau_i$, it is natural for graphene to display WL and negative magnetoresistance. Here these τ's represent different characteristic scattering times, such as τ_ϕ is the phase coherence lifetime associated to the inelastic scattering processes like electron-phonon interaction (at high and moderate T) and electron-electron interactions (at low T) which destroy the phase coherence, τ_i is the intervalley scattering time related to electrons scattering from one Dirac cone valley to another. τ_{tr} is the transport scattering time, equals to the twice of τ_e, the elastic scattering time obtained by ρ_0 and τ_{e-e} is the electron-electron scattering time also called the inelastic scattering time (due to Nyquist contribution and normal T^2 contribution) and τ_* is the effective scattering time mainly related to trigonal warping effects.

Typical magnetoresistance behavior of single- and bi-layer graphene is shown in Figure 4.13 with the two extreme situations: $\tau_*^{-1} << \tau_i^{-1}$ and $\tau_*^{-1} >> \tau_i^{-1}$. For our realistic case $\tau_* << \tau_i << \tau_\phi$ the magnetoresistance in both single- and bi-layer material is typically of a WL type.

Warping determines the relaxation rate τ_* which suppresses intravalley (anti)localization. Here Cooperon is a particle-particle correlation function usually described in WL regime. However the two intervalley Cooperons are not affected by trigonal warping due to time-reversal symmetry of the system. Thus, the temperature dependance of $\tau_\phi(T)/\tau_i$ is obtained from resistance measurements from the formulas mentioned in Ref. [5]:

$$\delta\sigma(T) = -\frac{e^2}{\pi h} ln(1 + 2\frac{\tau_\phi(T)}{\tau_i}) + \delta_0(\tau_*) \tag{4.3}$$

Here, the small correction $\delta_0(\tau_*)$ originates from two intravalley Cooperons strongly suppressed by the trigonal warping effects and intervalley scattering. Given that trigonal warping is extremely pronounced anywhere except for the

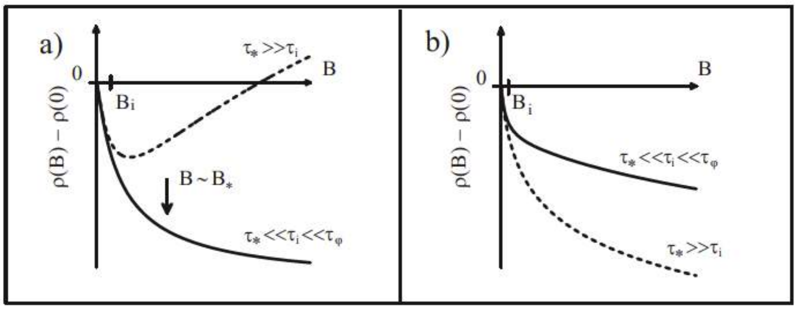

Figure 4.13. (a) Typical magnetoresistance behavior expected in a phase coherent ($\tau_\phi >> \tau_i$) SLG for a weak intervalley scattering, $\tau_* << \tau_i$ (solid line) and for the case when the symmetry-breaking intravalley scattering is slower than the intervalley one $\tau_* >> \tau_i$ (dashed). (b) Magnetoresistance of bilayer graphene, $\tau_* << \tau_i$ (solid line) and $\tau_* >> \tau_i$ (dashed).[5]

extreme vicinity of the Dirac point, we neglect this term. Therefore equation 4.3 reduces to,

$$\delta\sigma(T) = -\frac{e^2}{\pi h} ln(1 + 2\frac{\tau_\phi(T)}{\tau_i}) \tag{4.4}$$

$$ln(1 + 2\frac{\tau_\phi(T)}{\tau_i}) = -\frac{\pi h}{e^2}\delta\sigma(T) \Rightarrow 1 + 2\frac{\tau_\phi(T)}{\tau_i} = exp(-\frac{\pi h}{e^2}\delta\sigma(T)) \tag{4.5}$$

$$\frac{\tau_\phi(T)}{\tau_i} = [exp(-\frac{\pi h}{e^2}(\sigma_{total}(T) - \sigma_{Boltzmann})) - 1]/2 \tag{4.6}$$

Since these characteristic scattering times are related to the value of the conductance and not only to its variations, we performed four-wire measurements in order to exclude the effects of contact resistance/conductance. Due to experimental limitations like frequent breaking of contacts, this was not possible for the three layer graphene samples measured under electrochemical gating. For this reason the following analysis is presented mainly for four- and five-layer graphene samples.

In our case, it is also necessary to correctly normalize the ratio $\tau_\phi(T)/\tau_i$ with respect to Ref. [6]. As we know, at the increase of temperature, WL is destroyed at a temperature corresponding to the condition $\tau_i = \tau_\phi$. Thus, the $2\tau_\phi(T)/\tau_i$ curve must have a minimum in correspondance to the mentioned temperature. However this is possible only if resistance is normalized i.e., the exact width-to-length (W/L) ratio of the gated channel is used in order to convert the measured four wire resistance into the sheet resistance, R. Since W/L is unknown or ill-defined due to experimental limitations, then its exact value is determined by enforcing the condition that $2\tau_\phi(T)/\tau_i = 1$ at the minimum of the resistance curve as measured experimentally. As an example of the result of this procedure, we show in Figure 4.14, the ratio of $\tau_\phi(T)/\tau_i$ for four- and five- layer graphene devices.

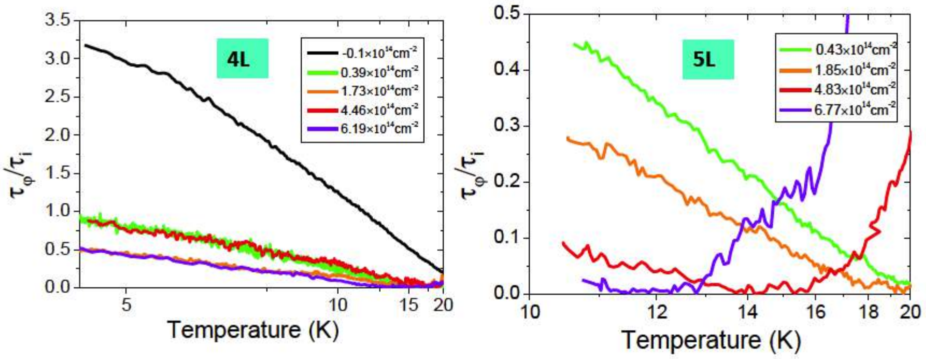

Figure 4.14. Ratio $\tau_\phi(T)/\tau_i$ plotted as function of logarithmic temperature scale at different induced carrier densities in a four- and five- layer graphene samples

Our measurements of the sample's sheet resistance allows us to directly obtain the temperature dependence of the ratio $\tau_\phi(T)/\tau_i$. Also τ_i can be safely assumed to be temperature independent, thus the temperature dependence of $\tau_\phi(T)/\tau_i$ is the same as that of $\tau_\phi(T)$ which in turn allows us to determine the dominating scattering process in the considered range of temperatures. By expressing $\tau_\phi \propto T^{-p}$, the index p gives the information on relevant scattering processes. At low temperatures, electron-phonon scattering determines p = 3, 4, or 5 depending on phonon dimensionality and degree of disorder; electron-electron scattering determines $p = 1$ for Nyquist (small momentum exchange) scattering and $p = 2$ for direct (large momentum exchange) scattering. As shown in Figure 4.14 for a four- and a five-layered graphene devices the $\tau_\phi(T)/\tau_i$ curves show almost no sign of super-linear behavior in the WL region, therefore we can conclude that electron-electron Nyquist scattering is the dominant inelastic scattering mechanism in this regime. The predicted behavior for Nyquist scattering is, ([7]):

$$\tau_\phi^{-1} = A\frac{k_B T}{2x} ln(\frac{x}{\hbar}) \tag{4.7}$$

where $x = \epsilon_F \tau_{tr}$ and A is a coefficient of the order of unity.

Typical parameters for 2D systems lead to a value of $x >> 1$, and thus an increasing τ_ϕ behavior with charge density n_{2D}. Upon strong localization conditions, $x < 1$ and the Boltzmann model no longer holds. Intermediate values of x instead marks a crossover from strong to weak localization and show a region where τ_ϕ can present an increasing behavior with n_{2D}. The exact form of the curves is determined by the dependence with n_{2D} of ϵ_F (which in the linear regions of the bands is a square root) and by τ_{tr}. Indeed, we find that our $\tau_\phi(T)/\tau_i$ values in both four- and five-layer graphene are weakly decreasing with the carrier density n_{2D} as shown at 2 K in Figure 4.19, in contrast with previous measurements on mono- and bi-layer graphene reported in literature [8]. Actually in these reference works the explored range of charge densities was limited by the capacitance of the solid gate dielectric, spanning only up to units in 10^{13}, while here we are able to reach values tens of times higher. This remark opens up two main possibilities. The first one is that in extremely high charge density regimes the elastic scattering rate is strongly reduced with respect to the low density regime; the second one is the aforementioned hypothesis the usual $x >> 1$ condition is not met in our experimental conditions, and that we are exploring the crossover region from weak to strong localization. To discriminate between the two hypothesis, we cannot limit ourselves to determine only the ratio of the phase coherence lifetime and the elastic scattering time. Thus, if we want to determine the values of these two quantities separately and not only their temperature dependence, we need either another independent measurement or a theoretical calculation to give us a reliable estimation of the elastic scattering time τ_{tr}.

In order to compute the values of this scattering time we must determine few other related parameters as described in the following. We first turn to compute the transport scattering time, τ_{tr} by using the standard Boltzmann (or Drude) equation for conductivity as proposed in Ref. [9]:

$$\sigma_{Boltzmann} = \frac{N_k N_S}{4} e^2 \tau_{tr} \sum_i N_i(E_F) v_{F_i}^2 \tag{4.8}$$

Figure 4.12 (left) shows that, in the absence of the WL contribution, the device's resistance (or conductance) saturates to a constant value at low temperature. Thus, the Boltzmann resistance (or the conductance, $\sigma_{Boltzmann}$) at the minimum (maximum) of our experimentally measured curves can be estimated from the minimum (maximum) value that the sheet resistance (conductance) assumes just before the onset of the logarithmic upturn (downturn). Then in order to extract τ_{tr} from the expression 4.6, we estimated $\sigma_{Boltzmann}$, e is the standard charge of an electron while N_K and N_S are the valley and spin degeneracy pre-factors. Here, v_{F_i} is the Fermi velocity of the i-th band, averaged between the $\Gamma - K$ and $K - M$ directions in the first Brillouin zone. The Fermi level E_F, Fermi velocity v_{F_i} and Density of States (DOS), $N_i(E_F)$ are calculated via Density Functional Theory (DFT) supercell approach by adding a uniform doping level equivalent to n_{2D} to the material in a Jellium model by our group's theoretician and other collaborators at Istituto dei Sistemi Complessi (ISC), Consiglio Nazionale delle Ricerche (CNR), Rome, Italy. They independently computed the elastic scattering times for the four- and five-layer gated graphene devices through ab-initio DFT calculations.

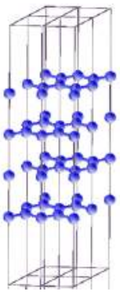

Figure 4.15. Supercell structure to model the band structure of a four layer graphene in ab-initio DFT calculations

Calculations were performed using the all-electron, full-potential, linear augmented plane wave (FP-LAPW) method as implemented in the ELK code [15] and the local density approximation [16] was adopted for the exchange correlation potential. For example, to model the four-layer graphene, a three-dimensional supercell with $c = 40\ a.u.$ was set, so that the periodic images are at least 10 Å apart, in order to avoid interactions and the distance between the layers is taken to be 3.35 in all the cases (Figure 4.15). Doping was simulated by adding electrons to the systems, together with a compensating positive background [17]. The Brillouin zone was sampled with a 28 × 28 × 1 mesh of k-points and the radius of the muffin-tin spheres for the carbon atoms were taken as $1.342a_0$, where a_0 is the Bohr radius. We set the parameter $RMTK_{max} = 7$, where RMT is the smallest muffin-tin radius and K_{max} is a cutoff wave vector and the charge density is Fourier expanded up to a maximum wave vector $G_{max} = 12a_0$.

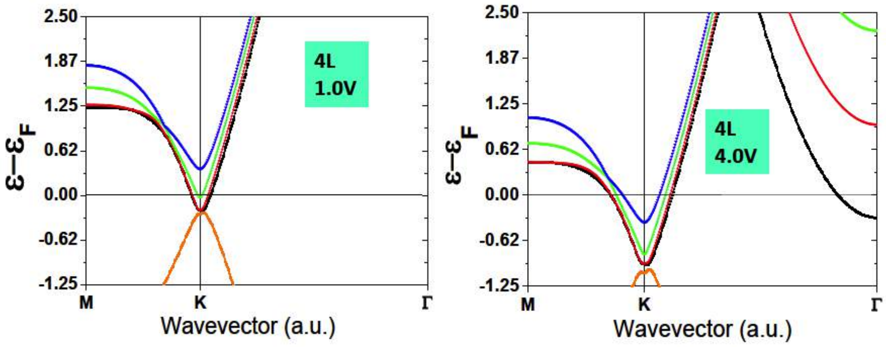

Figure 4.16. Electronic band structures obtained by ab-initio DFT calculations for four layer graphene at 1V (left) and at 4V (right)

The convergence of self-consistent field calculations is attained with a total energy convergence tolerance of 10^{-8} Hartree. Our collaborators performed the calculations of the band-structure for four- (Figure 4.16) and five-layer graphene that allowed us to obtain the values for both the DOS and the electron velocity for the populated bands at the Fermi level for the different values of the induced charge density. These quantities are related to the Boltzmann conductance value and the elastic scattering rate τ_e^{-1} by the equation 4.8 or $\tau_{tr} = 2 \times \tau_e$ [6]. The procedure to estimate the value of n_{2D} from the three layer graphene induction level by rescaling the quantum capacitances [10] and considering the series of the quantum capacitance of the material (estimated) and the capacitance of the electric double layer (measured by experiments on metals) is already mentioned in section 3.2. In addition, for four layer graphene we also compared these values with Hall effect measurements in order to confirm the values obtained from chronocoulometry.

The exact values of τ_{tr} are thus determined and are reported in Figure 4.19 as function of n_{2D}. In the literature τ_{tr} is found to follow a dependence on charge density of the type n^{γ}, where $1 < \gamma < 2$ and is thus expected to show an increasing behavior as n increases. However, we observe a decreasing trend of τ_{tr} for four layer graphene and more or less a constant behavior for five layer graphene in Figure 4.19, which is quite unexpected. This situation can be imagined as produced by some increase of induced-charge scattering centers at the surface of a graphene that already had some defects to which these new scattering centers are now added.

The physical situation can be imagined as the occurrence of following phenomenon: a) the increase of charge should increase the screening effect amongst the carriers and thus decrease the scattering potential of defects leading to decreased scattering rate. This could increase τ_e and in turn τ_{tr} also, b) in our case τ_{tr} decreases as a function of n_{2D} so there should be another source of defects present in the system that is able to give elastic scattering, hence we guess these are the new charged scattering centers introduced by the PES c) both the previous mechanisms are simultaneously present: in four layer graphene the winner is mechanism b) while in five layer graphene after the initial dominance of b), at higher doping a) becomes more important and τ_{tr} starts again to increase.

This means that the elastic scattering rate decreases at the increase of the carrier density due to the improved screening of elastic scatterers by the increased density of charge carriers. Thus, we suspect that the observed decrease of τ_{tr} in our four layer graphene data is due to the defects that were already there and for five layer graphene the two effects seem to cancel each other leading to its constant behavior. A schematic is shown in Figure 4.17 for the perturbed potential due the induced charge carriers introduced by the PES.

Now our main aim remains to determine the values of $\tau_{\phi}(T)$ and τ_i as a function of induced n_{2D} corresponding to different applied gate voltages. As reported in the literature and from the inverse linearity of $\tau_{\phi}(T)/\tau_i$ with temperature, we expect that both $\tau_{\phi}(T)$ and R are dominated by electron-electron scattering at

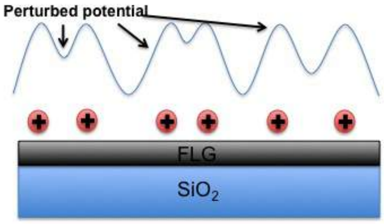

Figure 4.17. Schematic depicting the perturbed potential due to induced charge carriers at the surface of FLG samples

very low temperatures. In fact Ref. [11] suggests that electron-electron scattering is the main source of de-phasing (i.e. inelastic scattering) up to very high temperatures due to weak electron-phonon scattering. Ref. [12] discusses in details the temperature dependence of electron-phonon scattering. In particular, they point out that at intermediate temperature range $\sim 30-100\ K$, scattering by in-plane acoustic phonons does not account for all experimentally measured resistance behavior. According to them other scattering mechanisms might explain the observed experimental features. They also remark on how the crossover from linear to super-linear temperature dependence in the resistance in experimental data happens at higher temperatures than expected. This sometimes turns out to be experimentally observed as a second order degree i.e., quadratic ($R \sim T^2$) variation instead of the expected fourth order degree i.e., quartic ($R \sim T^4$) variation. Authors of Ref. [13] report their experimental findings for SLG gated with an electrolyte. Note that the Bloch-Grüneisen temperature, Θ_{BG} which sets the typical range for the crossover increases with doping level, further suppressing phonon scattering for higher gate voltages. In the low temperature limit, $T << \Theta_{BG}$, they observed a $R \sim T^4$ dependance, reflecting the 2D nature of the electrons and the acoustic phonons in graphene. While at higher temperatures, the typical semiclassical behavior of the resistivity $R \sim T$ was reported.

We feel safe to claim that below a few tens of $Kelvin$ in our devices, $\tau_\phi(T)$ has a form

$$\tau_\phi(T) = AT^{-1} + BT^{-2} \tag{4.9}$$

due to electron-electron scatterings only; here in equation 4.9 the coefficient of A, T^{-1} is a contribution from Nyquist scattering (small momentum exchange) and the coefficient of B, T^{-2} comes from Coulomb scattering.

From equation 4.8, in general, we can write the sheet resistance as follows

$$R = (\frac{N_k N_S}{4} e^2 \tau \sum_i N_i(E_F) v_{F_i}^2)^{-1} \tag{4.10}$$

here,

$$\tau^{-1} = \tau_{tr}^{-1} + \tau_{\phi}^{-1} = \tau_{tr}^{-1} + \frac{T}{A} + \frac{T^2}{B} \tag{4.11}$$

Therefore, R can be suitably represented as

$$R = (\tau_{tr}^{-1} + \frac{T}{A} + \frac{T^2}{B})/(e^2 P) \tag{4.12}$$

here P is a constant as

$$P = \frac{N_K N_S}{4} \sum_i N_i(E_F) v_{F_i}^2 \tag{4.13}$$

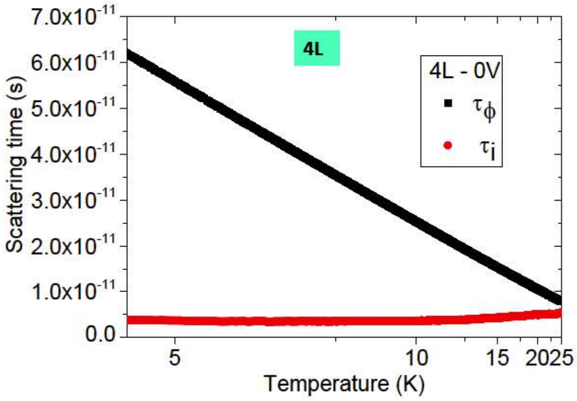

Figure 4.18. Characteristic scattering times $\tau_\phi(T)$ and τ_i plotted as a variation of temperature in a reciprocal scale at zero gate voltage for a four layer graphene device

P and τ_{tr}^{-1} have been already determined from ab-initio DFT calculations. Thus we are able to fit the pre-localization region ($\sim$ 20-50 K) of the resistance curves with a second-order polynomial fit in T, in order to determine the coefficients A and B. This calculation always resulted in a condition where $B << A$, strongly implying that Nyquist scattering term dominates at very low temperature, as expected. This enables us to determine the value of τ_ϕ as a function of temperature as shown in Figure 4.18.

As soon as $\tau_\phi(T)$ is known, τ_i can be obtained by inverting the already shown equation 4.6 for the $\tau_\phi(T)/\tau_i$ ratio. In the temperature range described purely by WL, τ_i convincingly turns out to be nearly constant as shown in Figure 4.18. This nearly constant behavior of τ_i is an important check of our original hyphothesis.

A linear fit has been made to extrapolate the value of $\tau_\phi(4K)$ for all the curves to allow us for an easier comparison. Theoretically computed electron-electron scattering rate at 4 K is shown as red dashed line and orange hatched region in Figure 4.19 for reference. In Figure 4.19 the order of magnitude of τ_ϕ is correct but its n_{2D} dependence turns out to be decreasing at higher doping. A possible explanation for this unexpected behavior could be: as we know x is n_{2D} dependent and from equation 4.7 as x increases we expect the scattering rate τ_ϕ^{-1} to decrease. But this is opposite to the observed trend of the scattering rate τ_ϕ^{-1} and hence the discrepancy arises. However, if we limit the range of x corresponding to the induced values of n_{2D} here at $1 < x < 2.71$ then we can convincingly explain the increasing behavior of the scattering rate τ_ϕ^{-1} with respect to x.

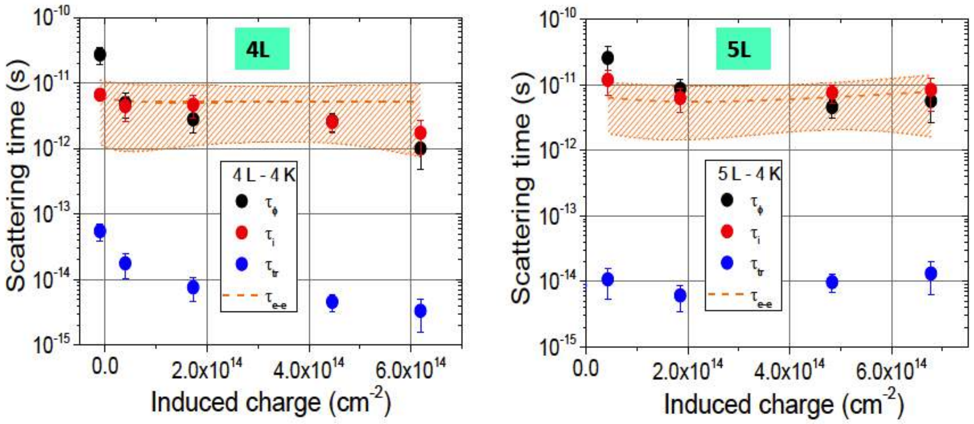

Figure 4.19. All related characteristic scattering times $\tau_\phi(T)$, τ_i, τ_{tr} and τ_{e-e} plotted as function of induced charge density at 4 K in four and five layer graphene devices; the orange highlighted region shows the theoretically expected values for τ_{e-e}

After estimating all these scattering times we made a consistency check of the values obtained so far. As mentioned earlier magnetic field has been applied to discriminate whether the logarithmic increase of the resistance at low temperature is due to WL or EEI. Since the upturn of resistance gets suppressed only when it is due to WL, under magnetic field application, we conclude that WL is the dominant cause of this upturn.

Equation 4.3 yields the zero field WL correction to the resistivity while the WL magnetoresistance is described by equation 4.14 that gives a complete description of the crossover between two characteristic regimes mentioned at the beginning (Figure 4.13).

$$\Delta\rho(B) = -\frac{e^2\rho^2}{\pi h}[F(\frac{B}{B_\phi}) - F(\frac{B}{B_\phi + 2B_i})] + \delta(B) \tag{4.14}$$

The equations 4.3 and 4.14 also include small contributions from the strongly suppressed intravalley Cooperons for SLG,

$$\delta_0(\tau_*) = [2e^2/(\pi h)]ln(\tau_\phi \tau_*/[\tau_{tr}(\tau_* + \tau_\phi)]) \tag{4.15}$$

and

$$\delta(B) = -[2e^2\rho^2/(\pi h)]F[B/(B_\phi + B_*)] \tag{4.16}$$

where, $B_* = \hbar c/(4De\tau_*)$ and funtion F is defined in the following.

However, in odd-number layered graphenes, WL is suppressed and eventually replaced by WAL upon the application of a magnetic field according to the formulas in equations 4.14 and 4.16. After combining these two equations we can write:

$$\delta\sigma(B) = \frac{e^2}{\pi h}[F(\frac{B}{B_\phi}) - F(\frac{B}{B_\phi + 2B_i}) - 2F(\frac{B}{B_\phi + B_*})]. \tag{4.17}$$

Here

$$F(z) = ln(z) + \psi(\frac{1}{2} + \frac{1}{z}) \tag{4.18}$$

$$B_{\phi,i,*} = \frac{\hbar}{4De}\tau_{\phi,i,*}^{-1} \tag{4.19}$$

and

$$D = \frac{1}{2}v_F^2\tau_{tr} \tag{4.20}$$

The measured curve for ABC-stacked three layer graphene is consistent with the typical situation $\tau_{tr} < \tau_* << \tau_\phi \approx \tau_i$ as reported in Ref. [14] where initial WL is replaced by WAL only at high fields. In this case the magnetoresistance fit of the curves at different temperatures is the typical approach followed in the literature but unfortunately we cannot benefit very much from it since we have the data only for one ungated sample at a single temperature.

Figure 4.20 shows $\delta\sigma$ as measured (black dots) and a fit (red line) as a function of magnetic field.

The parameters obtained from the usual temperature dependent analysis, where the curves are extrapolated at 4 K are $\tau_\phi = 3.97 \times 10^{-11}$ s, $\tau_i = 4.97 \times 10^{-11}$ s and $\tau_{tr} = 5.79 \times 10^{-14}$ s while parameters used in the reported fit to the magnetoconductance data at 4 K are $\tau_\phi = 3.2 \times 10^{-11}$ s, $\tau_i = 3.32 \times 10^{-11}$ s and $\tau_* = 2.9 \times 10^{-13}$ s.

The difference in τ_ϕ is small ($\sim 20\%$) and possibly due to the significant noise in the low-temperature transport measurement, which in turn renders a reliable extrapolation of the $\tau_\phi(T)/\tau_i$ ratio to 4 K difficult. As we have only one measured curve for the set of data under magnetic field hence only a single consistency check can be performed. However, with the data in hand WL suppression can be demonstrated anyway.

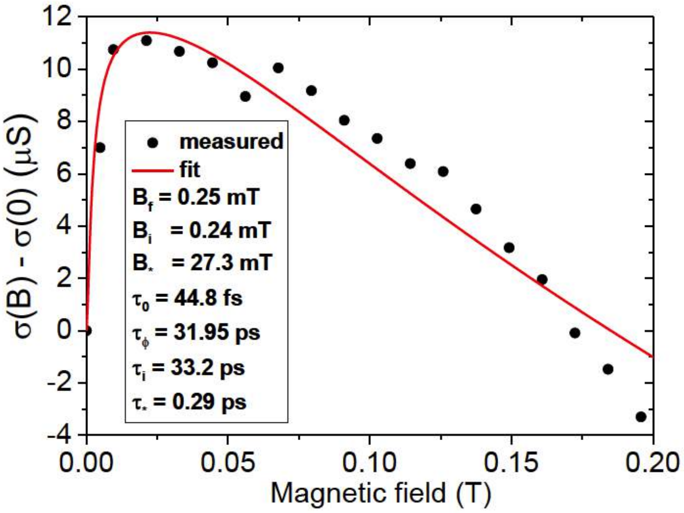

Figure 4.20. $\delta\sigma$ as measured (black dots) and as fitted (red line) as a function of magnetic field

4.4.2 Theoretical analysis of weak localization within the framework of 2DEG systems

In the analysis presented in previous section, we described our experimentally obtained results within the framework of specific models developed for graphene (as reported in the literature). However, we also tried to fit these results within the standard quantum diffusive transport regime in a 2D system with two valleys. Within the framework of WL, the sample's sheet conductance is determined by the temperature dependent behavior of the phase coherence characteristic time through the following formula:

$$\Delta\sigma(T) = -\frac{\Delta R}{R^2} = -(\frac{e^2}{\pi^2\hbar})log(1 + \frac{\tau_\phi(T)}{\tau_e}) \tag{4.21}$$

where the two characteristic scattering times are the elastic scattering lifetime, τ_e and the phase coherence lifetime, τ_ϕ. This relationship has the following significance: in order that the WL appears, electrons must be able to make a full loop thanks to elastic scatterings before incurring in an inelastic scattering event which destroys their phase coherence. Thus, WL gets suppressed as soon as the elastic scattering and phase coherence characteristic times become comparable. The inversion of the aforementioned formula in equation 4.21 allows us to obtain the temperature behavior of the ratio between the two characteristic times. Their ratio is computed in exactly the same way as described in the previous section

4.4.1 for $\tau_\phi(T)/\tau_i$. Although, here we have multiplied the ratio $\tau_\phi(T)/\tau_e$ by a factor of 2 due to the difference in relationships of equation 4.6 and 4.21 as is shown in Figure 4.21.

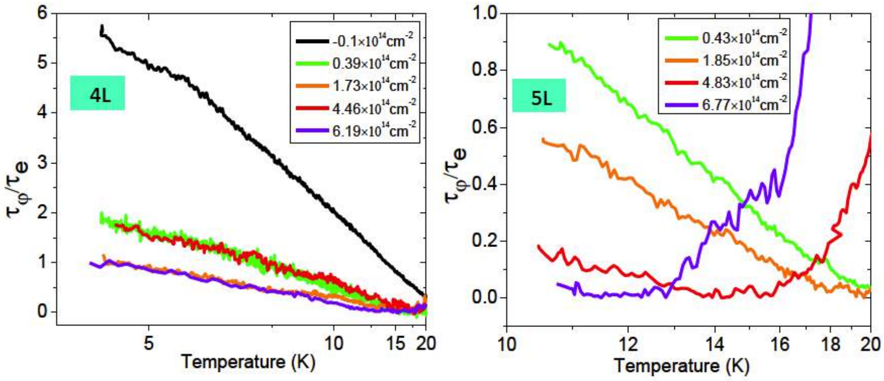

Figure 4.21. The ratio τ_ϕ/τ_e for four (left) and five (right) layered graphene devices, respectively

As explained in the previous section our experimental data are compatible with either the standard ($x >> 1$) or the crossover condition. Here we find (after correctly normalizing) that the ratio $\tau_\phi(T)/\tau_e$ is sharply decreasing with the induced carrier density n_{2D} at 2 K as shown in Figure 4.22, similar to our model in the previous calculations of section 4.4.1 in Figure 4.14 for four- and five-layer graphene.

Similar to the previous case, the aim to determine the individual values of both the scattering times requires another independent measurement to place a constraint on the equation 4.21. The most straightforward approach to this problem involves the estimation of the elastic scattering time through the following simplified model [8] (corresponding to equation 4.8) and/or by DFT calculations:

$$\tau_e^{-1} = \frac{N_k N_S}{4\sigma_{Boltzmann}} e^2 \sum_i N_i(E_F) v_{F_i}^2 \tag{4.22}$$

where in this scenario, τ_e can be approximated to τ_{tr} as described in the previous section and it is determined by ab-initio DFT calculations in exactly the same way described previously. All the parameters involved in equation 4.22 have been already discussed in the previous section that allowed us to determine the elastic scattering times τ_e as a function of the charge density in both four- and five-layer devices (Figure 4.23 (left)).

In the results of Figure 4.23, however, the elastic scattering rate follows a behavior similar to τ_{tr} of the previous section, i.e. decreasing at the increase

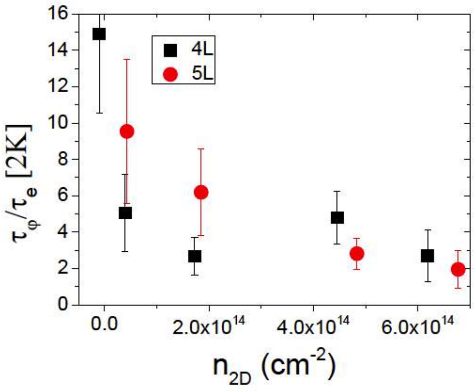

Figure 4.22. Ratio τ_ϕ/τ_e as function of induced charge density at 2 K for four (black squares) and five (red dots) layered graphene devices, respectively

of n_{2D} and thus, suggesting, as in the previous section, a significant increase of elastic scatterers with the increase of the applied gate voltage. To interpret its physical significance as we already said in the previous section, we imagine a system where the progressive introduction of charged scattering centers at the increase of gate voltage (due to accumulation of ions) at the surface of graphene tends to a decreasing behavior of τ_e. Since we earlier made independent calculations in the framework of ab-initio DFT calculations, our results captured the features of the problem at least in a semi-quantitative way. This was demonstrated when few of the calculations for computing τ_e were later performed in the tight-binding approach for validation. The latter approach yield very similar results for the elastic scattering lifetime, but is not able to account for one important effect: the doping induced filling of a massive parabolic interlayer band at the Γ point.

Further, we follow the standard approach on fitting the magnetoresistance measurements to obtain τ_ϕ. In absence of significant (pseudo)spin-orbit coupling, the theoretical predictions stated in equations 4.17 to 4.20 holds. Here we can safely neglect (pseudo)spin-orbit coupling because we have already ruled out low-temperature positive magnetoresistance contributions (Figure 4.12 (left)). Thus, the only two relevant fields are the applied magnetic field and the effective phase coherence field. By introducing the constraint on the value of $\tau_\phi/\tau_e(2\ K)$ in the fitting function, we are able to determine the value of both the elastic (left) and phase coherence (right) scattering times for three-(only one data point due to limited data availability), four- and five- layer graphene, whose curves are shown in Figure 4.23.

Thus, after performing calculations the order of magnitude for τ_ϕ here turns out to be 10^{-13} s instead of what we obtained in the previous section as 10^{-11} s. Also it can be seen from Figure 4.23 (right) that τ_ϕ initially decreases and

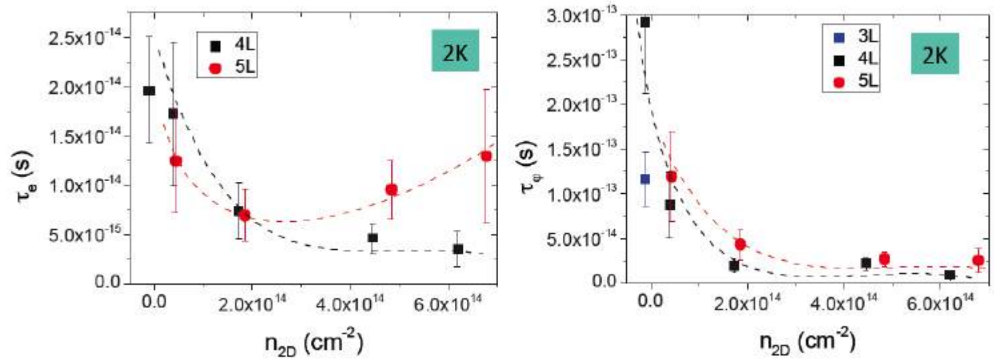

Figure 4.23. Determined values of τ_ϕ and τ_e at 2 K for FLG samples as a variation of n_{2D}

is probably wrong (due to the "classic" model description). This behavior of τ_ϕ is unacceptable since its order of magnitude is incorrect and it shows a contrary trend to the expected. Hence, the obtained behavior of characteristic scattering lifetimes within the standard 2DEG model is rather inadequate with respect to the expected results (as reported in the literature). Also we support the last statement having performed calculations in the framework of models specifically dedicated to graphene discussed in details in section 4.4.1. Therefore, we conclude that the "classic" 2DEG model fails to appropriately describe the scattering mechanisms in our FLG system.

Note that all these procedures described in previous two sections allowed us to determine the relevant scattering rates. However, due to experimental limitations (i.e., the device fault rate) we were able to perform magnetoresistive measurements only on the aforementioned three-layer device; the scattering parameters for the four- and five-layer gated devices on which we focused on in the earlier section remain unaccessible through the experimentally measured technique.

Bibliography

[1] K.S. Novoselov, A.K. Geim, S.V. Morozov, D. Jiang, Y. Zhang, S.V. Dubonos, *Science*, 306, 666, 2004.

[2] K.S. Novoselov, D. Jiang, T. Booth, V.V. Khotkevich, S.M. Morozov, A.K. Geim, *Proc. Natl. Acad. Sci.*, 102, 10451, 2005.

[3] Jianting Ye, Monica F. Craciun, Mikito Koshino, Saverio Russo, Seiji Inoue, Hongtao Yuan, Hidekazu Shimotani, Alberto F. Morpurgo, and Yoshihiro Iwasa, *PNAS*, 108, 32, 13002-13006, 2011.

[4] J. H. Chen, L. Li, W. G. Cullen, E. D. Williams and M. S. Fuhrer, Tunable Kondo effect in graphene with defects, *Nature physics*, 535-538, 7, 2011.

[5] V. I. Fal'ko, K. Kechedzhi, E. McCann, B. L. Altshuler, H. Suzuura, and T. Ando, Weak localization in graphene, *Solid state communications*, 143, 33-38, 2007.

[6] L. Piraux, V. Bayot, J. -P. Michenaud, J. -P. Issi, J. F. Marêché and E. McRae, The effect of disorder on weak localization and electron-electron interaction in low stage graphite intercalation compounds, *Solid state communications*, 59, 11, 711-715, 1986.

[7] Fabrizio Dolcini (private communication)

[8] F.V. Tikhonenko, D.W. Horsell, R.V. Gorbachev, and A. K. Savchenko, Weak localization in graphene flakes, *Phys. Rev. Lett.*, 100, 056802-1-4, 2008.

[9] Emmanuelle Cappelluti and Valentina Brosco (private communication)

[10] E. Uesugi, H. Goto, R. Eguchi, A. Fujiwara and Y. Kubozono. Electric double-layer capacitance between an ionic liquid and few-layer graphene. *Scientific Reports*, 3:1595, DOI:10.1038/srep01595, 2013.

[11] F.V. Tikhonenko, A. A. Kozikov, A. K. Savchenko, and R.V. Gorbachev, Transition between electron localization and antilocalization in graphene, *Phys. Rev. Lett.*, 103, 226801, 2009.

[12] E. H. Hwang and S. Das Sarma, *Phys. Rev. B*, 77, 115449, 2008.

[13] D. K. Efetov and P. Kim, *Phys. Rev. Lett.*, 105, 256805, 2010.

[14] E. McCann, K. Kechedzhi, Vladimir I. Fal'ko, H. Suzuura, T. Ando, and B. L. Altshuler, Weak-Localization Magnetoresistance and Valley Symmetry in Graphene, *Phys. Rev. Lett.*, 97, 146805, 2006.

[15] http://elk.sourceforge.net/

[16] J.P. Perdew and A. Zunger, *Phys. Rev. B* 23, 5048, 1981.

[17] Y. Ge and A. Liu, *Phys Rev B*, 87, 241408(R), 2013.

[18] L. Piraux, J. -P. Issi, J. -P. Michenaud, E. McRae and J. F. Marêché, Evidence for hole localization in a low stage acceptor graphite intercalation compound, *Solid state communications*, 56, 7, 567-569, 1985.

[19] L. Piraux, V. Bayot, X. Gonze, J. -P. Michenaud and J. -P. Issi, Effect of a magnetic field on weak localization and Coulomb interactions in acceptor graphite intercalation compounds, *Phys. Rev. B*, 36,17, 9045-9051, 1987.

[20] L. Piraux, V. Bayot, J. -P. Michenaud and J. -P. Issi, Weak localization and coulomb interaction in graphite acceptor intercalation compounds, *Physica Scripta*, 37, 942-947, 1988.

[21] E. R. Margine and F. Giustino, Two-gap superconductivity in heavily n-doped graphene: Ab initio Migdal-Eliashberg theory, *Phys. Rev. B*, 90, 014518, 2014.

[22] Sohier T. et al., Phonon-limited resistivity of graphene by first-principles calculations: Electron-phonon interactions, strain-induced gauge field, and Boltzmann equation, *Phys. Rev. B* 90, 125414, 2014.

[23] Temperature dependence of electric transport in few-layer graphene under large charge doping induced by electrochemical gating, *submitted* to Scientific Reports, 2014.

Chapter 5

Electrochemical gating of CVD-grown single layer graphene, graphite and CaC_6

In the previous chapters we described the electrochemical gating technique [1] and its application mainly on metals and FLG. However, we studied the field effect due to electrochemical gating technique on SLG, highly oriented pyrolytic graphite (HOPG) and CaC_6 as well. In this chapter we present our results on these materials in order to confirm the results reported in literature and describe our progress in relation to them.

5.1 Field effect in CVD-grown SLG

The powerful technique of electrochemical gating is very well know to even drive the phase transition of different materials [2]. In the literature there are several claims that it may be possible to induce superconductivity in SLG. The authors of Ref. [3] have predicted the possibility to induce superconductivity in SLG sheet by doping its surface with alkaline metal adatoms. Mainly Lithium, in a manner analogous to which superconductivity is induced in graphite intercalated compounds (GICs). They report that in order to induce superconductivity in graphene, it is beneficial to bring the interlayer state to the Fermi energy and to localize it as close as possible to the graphene plane. In this way, they claim that it is possible to access the superconducting state with T_c = 8.1 K or 17-18 K by decorating with Li^+ ions on top or on both sides of the surface of SLG, respectively, as shown in Figure 5.1.

Another classic way to induce superconductivity in graphene appears to be a large increase of the carrier density, to be able to shift the Fermi level far from the

Dirac point and close to a Van Hove singularity (VHS).

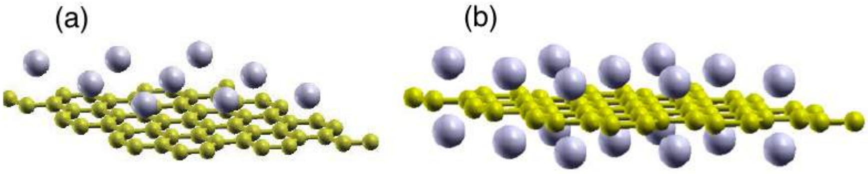

Figure 5.1. SLG decorated by Li^+ ions (a) only on top and (b) on both sides [4]

In addition, as we have described in section 2.4 of Chapter 2, SLG has always been an interesting topic of research due to several motivations. There are extensive reports in the literature that focus on SLG gated with different configurations of PES, ionic liquids and solid dielectrics. Hence, the target of our work is to check the possibility to induce superconductivity in SLG through electrochemical gating experiments and repeat the earlier experiments with our innovative PES, since this technique allows the observation of a large effect thanks to a higher charge induction. In this section we describe the results of different experiments we have been able to perform mainly at room temperature and few others with temperature variation. Besides the obvious measurement of induced charge these experiments include results of Dirac curves, Raman measurements and behavior of resistance versus temperature for CVD-grown SLG.

5.1.1 Measurement of induced charge: Hall effect

Motivated by the prediction of accessing superconductivity and the record of induced charge in FLG, we performed the electrochemical gating in SLG devices made from CVD-grown graphene. We measured approximately twelve CVD-grown SLG devices. Their fabrication and patterning is already described in Chapter 3 and Figure 5.2 shows a schematic of the device geometry and its electrical configuration.

The first step has always been to measure the intrinsic charge carrier density by standard Hall effect measurement even before drop casting and UV curing the PES. This measured value is found to be in the range $10^{12} - 10^{13}$ cm^{-2} and slightly p-doped due to adsorbed water molecules from the atmosphere. Later, after drop casting the PES, this value changed slightly and we performed the Hall effect again to measure the value of intrinsic charge without any applied gate voltage. The Hall effect was performed in the same way as described in details in Chapter 3 in section 3.2.2. A variable gap magnet with magnetic fields of magnitude 0.4 T, 0.5 T and 0.6 T was used and source drain current was less than 1 μA. In the same way, Hall effect was performed for all the applied gate voltages in steps

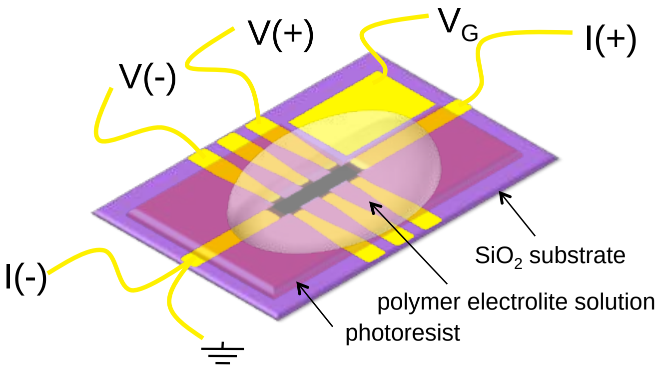

Figure 5.2. Schematic of the FED used to perform transport measurements [5]

of $|V_G| = \pm$ 0.5 V within the electrochemical stability window. The results of the Hall effect measurements are shown in Figure 5.3 for three different devices labelled as UG2C-11 etc. Figure 5.3 shows that the data points are gathered around a common trend. For $|V_G| < \pm$ 1.5 V, n_{2D} depends almost linearly on V_G and then it grows more than linear for higher V_G. The induced charge densities for positive and negative gate voltages are rather symmetric for $|V_G| < 2.5$ V while for $|V_G| > 2.5$ V the positive values increase much more steeply.

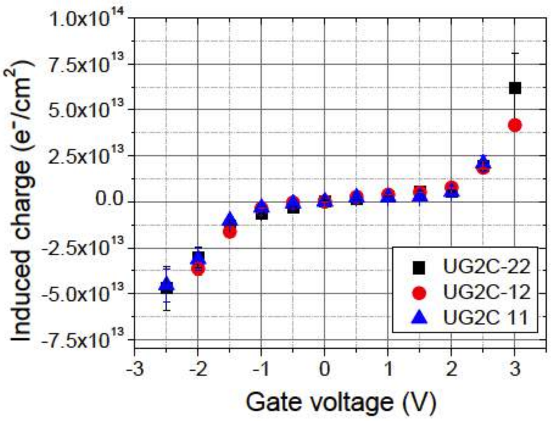

Figure 5.3. Induced charge as a function of both positive and negative applied gate voltage for three different CVD-grown SLG devices

In this case our specialized PES gating technique has been used for the simultaneous chemical doping with Li^+ ions and field effect gating of SLG devices. By applying a sufficiently high gate voltage we are able to accumulate the ions on the surface of SLG for a relatively short time. This was done in order to immediately cool down the system in the configuration of SLG decorated by Li^+ ions.

In this way an additional very high surface charge and the expected modification of the electronic bands and of the phonon density of states produced by the overlaid Li^+ atoms are, in principle, achieved that should be sufficient to induce superconductivity in SLG. Following this procedure it becomes possible to induce a permanent modification of the electronic structure of SLG. By permanent modification we mean that we intend to accumulate the Li^+ ions on the surface of SLG in a way that it becomes impossible to change this configuration, at least during the time of low-temperature transport measurements. In other words the properties of Li-doped SLG are modified simultaneously by the electric field effect and by the electrochemical doping due to the PES. Then, may be, it could be possible to reach the predicted superconducting state with T_c = 8.1 K or 17-18 K simply by controlling the properties of SLG by applied gate voltage. Figure 5.1 (a) shows the configuration in which Li^+ ions have to be accumulated on top of SLG in order to achieve 8.1 K of possible superconducting critical temperature while Figure 5.1 (b) shows the requested configuration if Li^+ is decorated on both sides of SLG leading to a predicted T_c of 17-18 K.

A slight hint of this possibility of accumulation of Li^+ ions can be seen in Figure 5.4 where the resistance of the SLG device slowly saturates in a long time after the application of gate voltage. This happens if we exceed the limits of electrochemical window (2.5-3 V) and perform the so called over-gating experiments. This is described in details in Chapter 3 in section 3.2.5. As it can be seen in the Figure 5.4 the application of the gate voltage modifies the electronic properties of SLG in a quasi-permanent way and, thus, we can guess that temporary Li^+ ion deposition may be its cause.

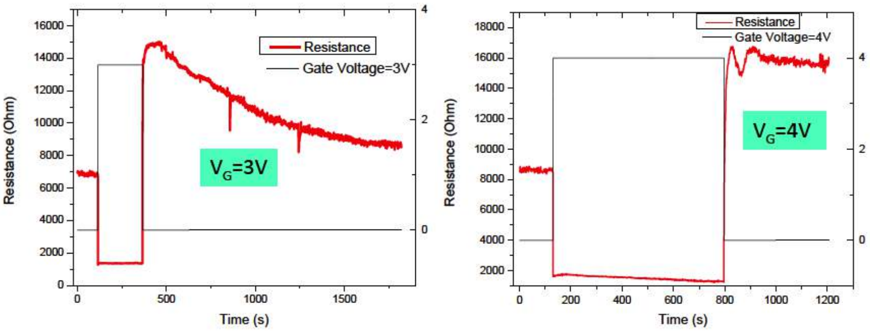

Figure 5.4. (a) Resistance saturates to its original value in a very long time after the removal of gate voltage V_G = 3 V and (b) permanent modification of the resistance value at V_G = 4 V

However up to now we have been able to induce a maximum of 6×10^{13} cm^{-2} measurable surface charge carrier density in SLG. Then after inducing this charge with the same configuration of PES, we immediately went down in temperature to the cryo-cooler's base temperature in order to observe superconducting transition. Unfortunately the devices broke peeling off the PES along with the device due to mechanical stress and hence we were not able to observe any superconducting transition up to now.

5.1.2 Dirac curves

We have already shown the sheet resistance (or conductance) behavior with respect to a continuously applied bias for a three- and four-layer graphene in the previous chapter in section 4.2.

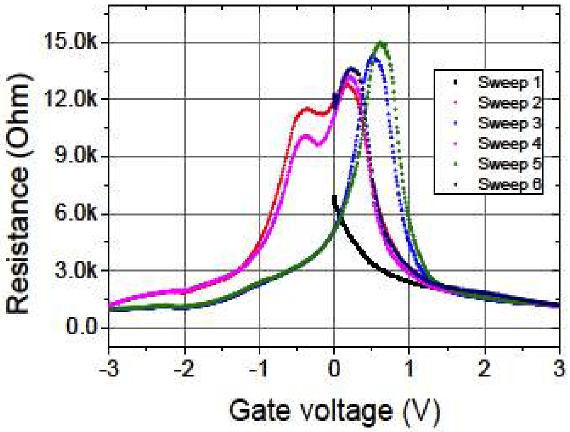

Figure 5.5. Hysteretic Dirac curves for CVD-grown SLG

Here we show the Dirac curves for a CVD-grown SLG device in Figure 5.5. We continuously applied the gate voltage to track the behavior of resistance and made six sweeps ranging from V_G = +3V to -3V. Up to $V_G \sim \pm$ 1 V (with respect to the charge neutrality point (CNP)) the curve is symmetric. This linear increase of the sheet resistance is due to accumulation of either electrons or holes, within the voltage range $V_G = \pm$ 1 V. Then we see a peak corresponding to the resistance maximum which, in principle, should coincide with the CNP as we further span the gate voltage. However this peak does not correspond to the standard CNP and is shifted towards the right because of spontaneous doping due to presence of adsorbates (e.g., moisture). As we make different sweeps this peak shifts backwards with respect to the original resistance maximum and its behavior is hysteretic i.e., the peak position in the next sweep does not correspond to the previous original peak. This hysteretic behavior of Dirac curves in Figure 5.5 means that there is a pronounced effect on the properties of SLG due to the electrochemical gating with PES. Also we suspect that during this process Li^+ ions are accumulated or trapped over the SLG surface, hence producing the observed hysteresis. These strongly hysteretic Dirac curves are thus another hint for the presence of Li decoration over the SLG in our overgating experiments.

5.1.3 Raman measurements

Raman spectroscopy is one of the most used characterization techniques in carbon science and technology. It provides a huge wealth of knowledge about the number and orientation of layers, electric or magnetic fields influence, strain, doping, disorder, quality and types of edges, and functional groups. The measurement of the Raman spectrum of graphene [6] triggered a huge effort to understand phonons, electron-phonon (e-ph), magnetophonon and EEIs in this material.

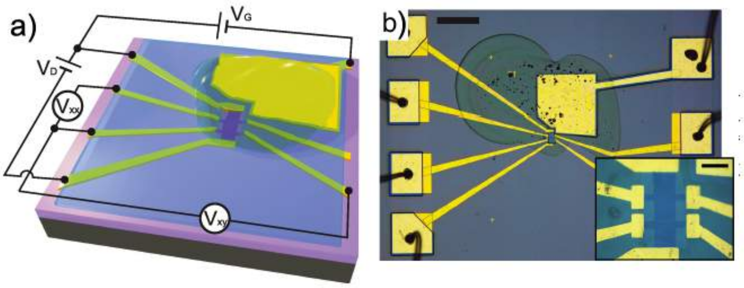

Figure 5.6. (a) Schematic of the PES gated SLG device and electrical configuration used for the measurements (b) Optical micrograph of the device used in the experiments, the scale bar is 300 μm and inset shows the graphene channel with a scale bar of 30 μm. [7]

The details of the Raman spectra are described in section 3.1 of Chapter 3. Here we present Raman spectra similar to the one of Figure 3.3 for a three layered graphene device after drop casting the PES. In addition to the conventional spectra, we were able to measure the Raman spectrum simultaneous to the application of gate voltage for CVD-grown SLG. Also authors of Ref. [7] studied the dependence of the Raman spectrum of defected SLG on the level of electrostatic doping, in samples with a fixed amount of defects. They combined the PES gating with in situ Hall effect measurements and Raman spectroscopy at different excitation wavelengths. Their set up and optical micrograph of the device is shown in Figure 5.6. As [7] reports, doping has major effects on the Raman spectra. It evolves as follows: (a) the D peak changes intensity, (b) the G peak position increases while the G peak itself stiffens due to the non-adiabatic removal of the Kohn anomaly at the Brillouin Zone (BZ) center, Γ.

Now, we focus on the gate voltage dependence of the Raman signatures as we measured for our CVD-grown SLG sample. Figure 5.7 shows the Raman spectra of sample UG2C 42 as a function of applied gate voltage.

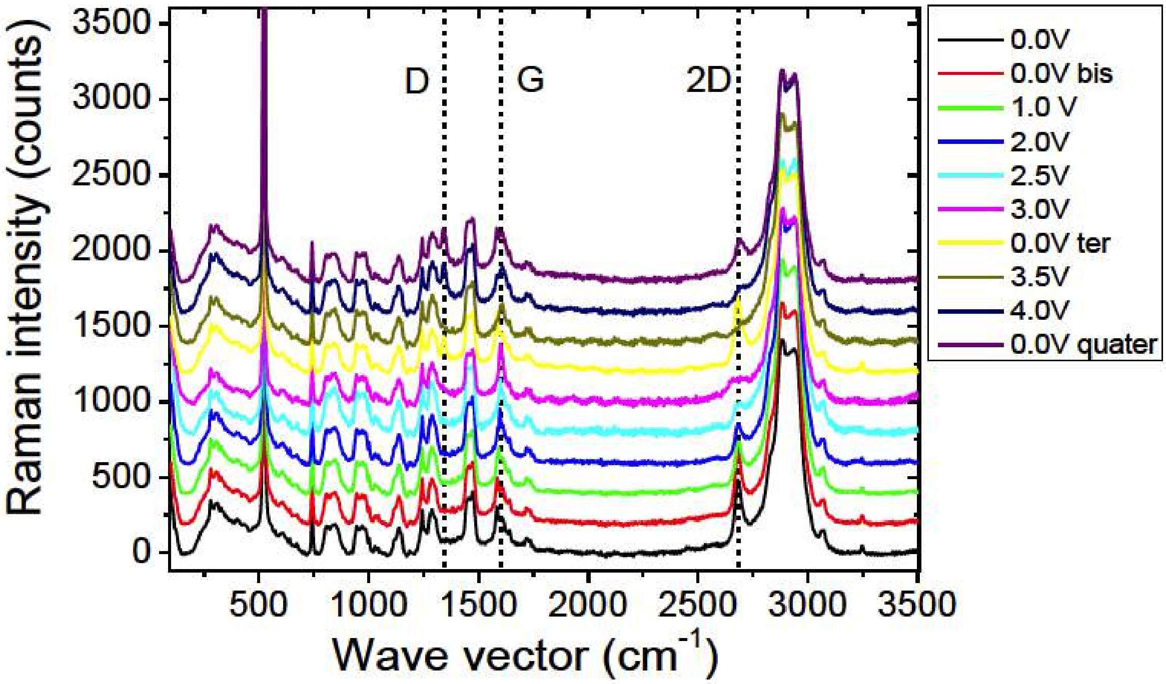

Figure 5.7. Raman spectrum of CVD-grown SLG, measured at 532 *nm*, for different applied gate bias through PES electrochemical gating

Raman measurements were performed at INRIM, Torino and we used a 20X objective with a laser of 532 nm wavelength. The slit aperture was 25 μm and the laser power was 5 mW. The main features we observed in our measurements are as described in the following:

1. At the beginning, we did not observe any D peak but later a strong D peak appeared at $V_G = 4$ V that is visible also after the removal of gate voltage as seen in the two top most spectra of Figure 5.7. This appearance of the D peak suggests that as we exceed the electrochemical stability window for graphene and apply the gate voltage beyond its limits, some sort of permanent defects develop at the surface of SLG that give rise to this D peak. However, at the present moment, we cannot be sure that this D peak is due to the deposition of the Li^+ ions or there are some vacancies permanently formed at the surface of SLG.

2. The G peak instead stiffens as the effect of gate voltage is increased. At lower voltages it is somewhat suppressed but as we increase the gate voltage it sharpens and steepens. Again at $V_G = 4$ V there is an abnormality seen for the

G peak. Also there is a slight change in the G peak position compatible with the results of [7] and [16].

3. For the 2D peak it is seen that it is pronounced only when there is no or low applied gate voltage while it suppresses progressively as we increase the effect of applied gate voltage. At $V_G = 3$ V there is essentially no 2D peak (magenta curve) but then at $V_G = 0$ V (yellow curve) the 2D peak reappears strongly. Here again at $V_G = 4$ V partial suppression of the 2D peak can be seen. This is in accordance with the hysteretic behavior of the resistance as seen in the Dirac curves of Figure 5.5 where the resistance peak shifts backwards probably due to the heavy doping of the accumulating Li^+ ions.

5.1.4 Resistance behavior as a variation of temperature

Few of the CVD-grown SLG devices were measured in temperature in order to observe the behavior of resistance, study the effect of electrochemical gating and see the possibility of induced superconductivity. The observed behavior of the resistance vs. temperature (from 340 K down to 100 K) in one of these devices is shown in Figure 5.8.

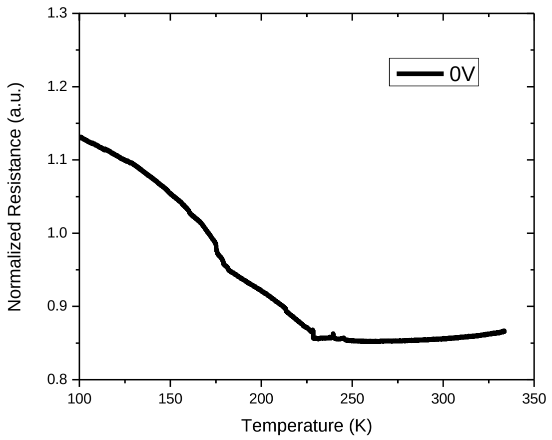

Figure 5.8. Resistance vs. temperature for a CVD-grown SLG

The devices were heated up above the room temperature in order to remove adsorbed moisture and then cooled down. The resistance shows semiconducting like features as we could measure up to 100 K and is in accordance with the results reported in the literature. The high rate of breakage of devices due to mechanical stress produced by the PES posed a serious limitation to this kind of measurement at cryogenic temperatures. This issue has been addressed in section

3.2.5 of Chapter 3 and it must be emphasized that more than 80 % of the devices do not survive the first cooling. As a consequence, even if we had some evidence (Dirac curves, room temperature resistivity under gating, Raman spectra) of the (partial) accumulation of Li^+ ions on the SLG surface, we were not able up to now to measure the transport properties down to 2.7 K.

5.2 Field effect in highly oriented pyrolytic graphite

Graphite is the parent compound for single- and few-layer graphene, fullerenes, carbon nanotubes and other carbon based materials and for this reason it has been at the center of vast research activity. Several efforts have been reported in the literature about the possibility to gate and observe the field effect on graphite.

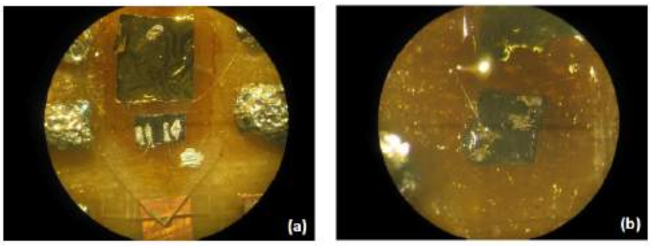

Figure 5.9. Real pictures of FEDs prepared by HOPG; (a) The configuration when the current and voltage contacts are over the surface; (b) configuration when the current is injected through the bulk HOPG and voltage is measured on the surface

However, in our particular interest we have performed experiments on highly oriented pyrolytic graphite (HOPG) by electrochemical gating with our new and improved formulation of PES. There are no reports in the literature on this topic, i.e. on gating graphite by electrolyte solutions. We could still relate our results to those described by standard gating.

Figure 5.9 shows real pictures of our FEDs in both the configurations where the current contacts are on the top and along the sides of the HOPG flake respectively. The devices were prepared in the following way: HOPG was mechanically exfoliated and all the contacts were painted by hand on its surface by connecting it with very thin gold wires. A gold flake was used as a gate pad which connected the PES with the exposed graphite surface. A small gate window was formed by using liquid Kapton (polyimide) that was UV cured. Then PES was drop casted in order to perform gating experiments. In Figure 5.10 we show the schematic for both the configurations we have used to perform the measurements.

After the device preparation we measured the induced charge by double step

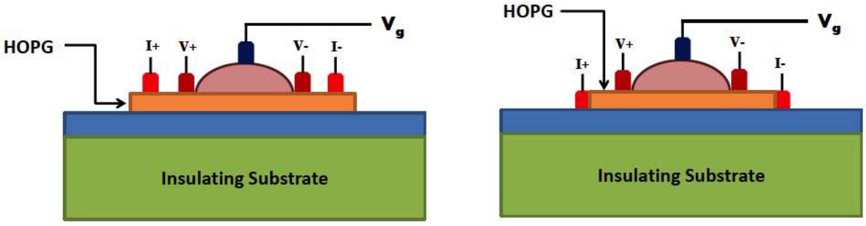

Figure 5.10. Schematic showing both the device configurations and the respective electrical connections for (a) current and voltage contacts over the surface and (b) current contacts along the bulk HOPG crystal and voltage measured on the top of it

chronocoulometry and the results are shown in Figure 5.11. The order of magnitude of the induced charge we obtained was approximately equal to 3×10^{14} cm^{-2} at +3 V. The trend of the induced charge variation as a function of gate voltage is more or less similar to that we have obtained for SLG and FLG samples as described already. However the extremely high-induced charge values similar to the ones obtained in metals, sometimes observed in these experiments, cannot be assumed to be correct here. Due to the partial contact of the PES with the gold wires used for the contacts here we probably have a partial gating of the wires too, which leads to an overestimation of the charge on HOPG.

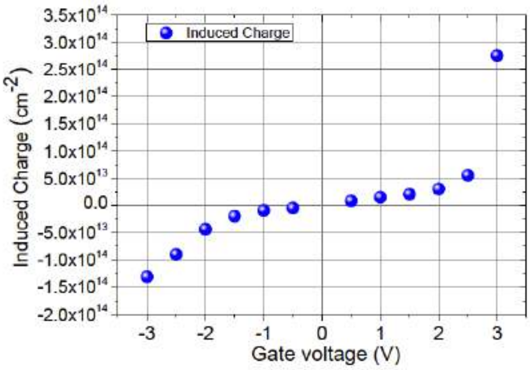

Figure 5.11. Induced charge carrier density as a function of gate voltage

In addition to temperature and magnetic field dependence of the electrical resistance, the authors of Ref. [8] have studied the behavior of tens of nanometers thick multigraphene samples as a function of bias voltage applied perpendicular to the graphene planes. They found that the resistance of different samples changes asymmetrically with the bias voltage sign.

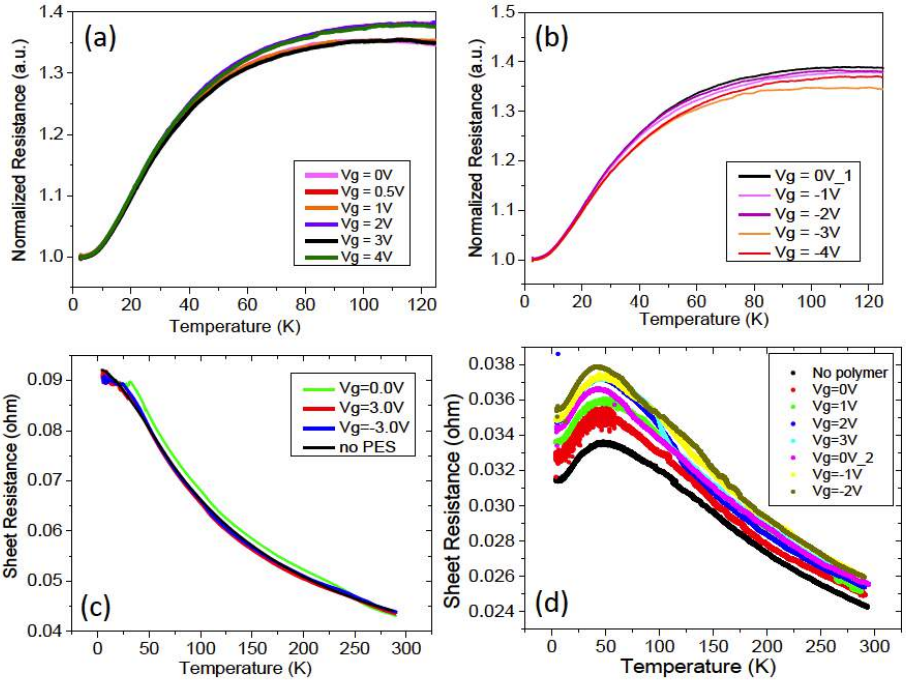

Figure 5.12. Resistance behavior as a function of temperature (a) normalized R vs. T showing pronounced metallic-like features and eventually saturating for positive V_G (b) the same as in (a) but for negative V_G (c) semiconducting-like behavior due to all-contacts-on-top configuration (d) an intermediate behavior of resistance when the current contacts are able to access first few layers of HOPG's surface

The authors experimented and reported that out of all the measured samples the thickest multigraphene flakes behaved in a metallic-like way initially and then their resistivity eventually saturates, while the thinner ones behaved in a way that appear totally semiconducting (Figure 2.28 (a)). The flakes with intermediate thickness initially show a less pronounced but well visible metallic-like behavior in the temperature range ∼ 10-50 K, then showing semiconducting features at higher temperature. In analogy with their results we studied different configurations for our FEDs. We found that when we injected the source-drain current (I_{SD}) through the bulk HOPG by fabricating current contacts along the total thickness or vertical sides of the sample, our results correspond to the sample that Ref. [8] referred to as thickest. This means that when the current flow is across all the graphene planes, the material behaves in a metallic way and the resistance saturates later at low temperature. If the current contacts stay over the top, at the surface of HOPG, then we obtain a semiconducting-like behavior of the material. For other intermediate thicknesses the observed behavior of the resistance is a mixture of the above two: semiconducting-like and then metallic-like. One important difference is that the authors of Ref. [8] gated their devices with the standard dielectric while we always gated by PES reaching very high values of the induced charge.

Figure 5.12 shows the different behaviors of resistances for our different configurations of FEDs. We have characterized approximately twenty samples and have consistently observed such behavior of the resistance. At a first sight, the results shown in Figure 5.12 allow us to already draw some preliminary conclusions: i) depending on where the current contacts are placed, in our electrochemical gating experiments we can be more sensitive to the bulk of the sample or to the topmost layers of HOPG. This conclusion has also consequences in the experiments on CaC_6 described in the next section; ii) the strong charge induction (both positive and negative) obtained by our electrochemical gating produces some effects on the resistance particularly in the samples that show a metallic-like behavior.

Using the model presented in Ref. [16] we have fitted our experimentally obtained results just described above. They suggest that the measured resistance can be explained by the parallel contribution of the resistance of semiconducting graphene layers with low carrier density $< 10^9$ cm^{-2} and the one from metallic-like internal interfaces. The results indicate that ideal graphite with Bernal stacking structure is a semiconductor with a narrow band gap $E_g \sim 40$ meV. They propose a simple model to explain the experimental longitudinal resistance data obtained in different oriented graphite samples of different thickness and area. The rather complicated behavior of the longitudinal resistivity can be explained assuming the parallel contribution of regions with semiconducting graphene layers and ones from the interfaces between them, as transmission electron microscopy (TEM) studies revealed. The internal structure of the used samples is shown in the TEM picture in Figure 5.13. As shown in [17], this picture reveals single crystalline regions of graphene layers, of thickness between 30 nm and 100 nm.

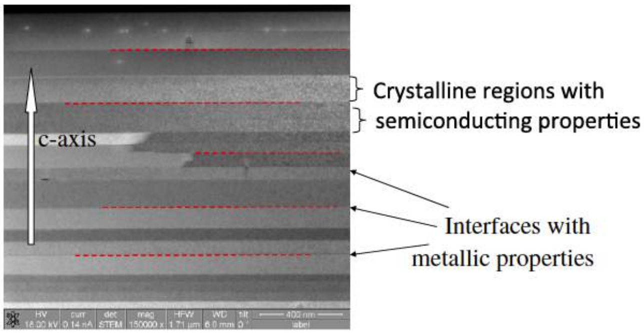

Figure 5.13. TEM picture of the internal microstructure of a highly oriented pyrolytic graphite sample. The dashed red lines indicate some of the interface regions between the single crystalline graphite parts. Regions with different gray colors indicate a slightly different orientation of the graphite structure.[16]

They describe the measured behavior of the resistance of graphite samples as due to the existence of well-defined interfaces between the single-crystalline regions. The interfaces between crystalline regions in semiconductors with different orientations, lead to confined quasi-2D carrier systems with a much larger carrier density than the bulk matrix. They assume therefore that these interfaces running parallel to the graphene layers of the graphite structure are the origin of metallic-like resistivity as well as of the apparent large carrier density measured in bulk samples, i.e. $n_0 \gtrsim 10^{10}$ cm^{-2}, an assumption that is supported by the change in absolute resistivity with thickness [17]. Taking into account the internal microstructure of the graphite samples, it becomes clear that it is necessary to measure the resistance of samples of small enough thickness in order to get the intrinsic transport of the graphite structure with its weak-coupled graphene layers.

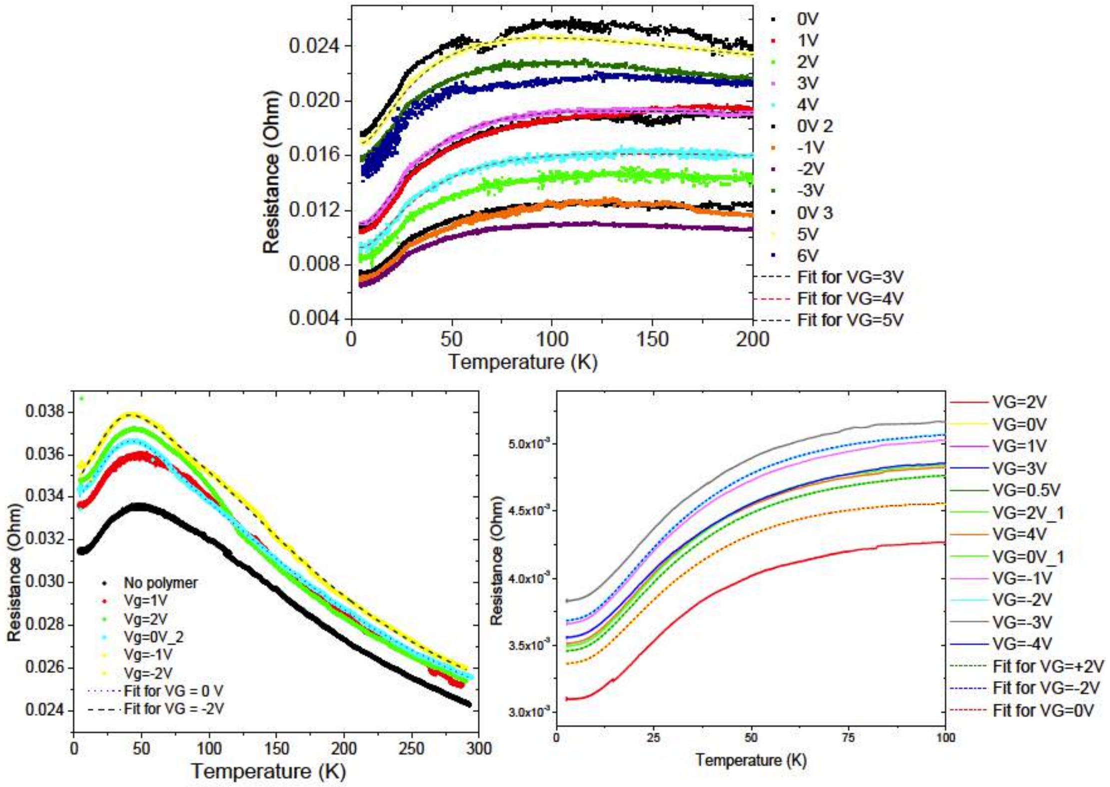

Figure 5.14. Topmost and bottom right curve shows the experimental data obtained for sheet resistance vs. temperature corresponding to the configuration in which the current is injected through the bulk and voltage contacts are on top and this data is fitted with the model presented in Ref. [16]. The lower left curve is the experimental data fitted with the same model corresponding to the configuration when the all the contacts are on top but voltage contacts are sensitive to first few layers of HOPG's surface

Following the results from Ref. [17] as well as the semiconducting behavior of resistance described in Ref. [16], obtained for a thin graphite sample, it has been assumed that the graphene layers inside each graphite sample are semiconducting and their signal between the voltage electrodes is given by an effective resistance of the type:

$$R_s(T) = a(T)\ exp(+E_g/2k_BT) \tag{5.1}$$

The prefactor $a(T)$ depends basically on the mobility, i.e. the mean free path, and on details of the carriers band structure (e.g. effective mass).

For samples with thickness larger than 50 nm and of several micrometers length, there is a larger probability of having interfaces, whose signals will be picked up by the voltage contact electrodes (usually several micrometers apart). Therefore, in parallel with $R_s(T)$ they simulate the contribution from the interfaces through the resistance:

$$R_i(T) = R_0 + R_1T + R_2\ exp(-E_a/k_BT) \tag{5.2}$$

where the coefficients R_1, R_2 as well as the activation energy E_a are free parameters. The temperature-independent term in the above equation represents the residual resistance measurable at low enough temperatures. The second temperature dependent term is a weak contribution from the metallic regions within the interfaces and the third term is speculated to be related to superconducting like behavior of graphite.

The total resistance $R_T(T)$ is given by the parallel contributions of R_s and R_i as

$$R_T(T) = [R_s(T)^{-1} + R_i(T)^{-1}]^{-1} \tag{5.3}$$

Clearly, by changing the parameters one can obtain all types of behavior for R(T). We have obtained a consistent description of the data and the main free parameter E_g is similar for all samples approximately to be equivalent to 40± 15 meV. These fits are shown for some of the experimental curves at different gating in Figure 5.14. It is worthwhile to notice that the interfaces as well as the single-crystalline regions are restricted to regions in the ab plane parallel to the graphene layers. This fact supports the use of the simple parallel resistance model.

5.3 Field effect in CaC$_6$

Similar to the great deal of fundamental and practical interest in the possibility of inducing superconductivity in a SLG, the superconducting mechanism for CaC$_6$ has also attracted much attention for the respective roles of the π^* and interlayer

(IL) bands. Ref. [10] marked the discovery of CaC_6, then Ref. [11] described the novel method of its synthesis, and [12] suggested the exact preparation of samples.

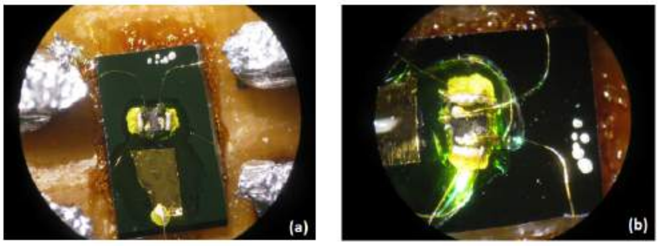

Figure 5.15. Device pictures for CaC_6 (a) before putting the PES (b) after drop casting the PES; the gold flake can be seen placed besides the CaC_6 crystal with contacts painted for a four wire measurement

Our groups's expertise in point-contact spectroscopy reported in [13] describes in details the gap determination in CaC_6, where a complex glove bag technique for the preparation of the samples (that are extremely air-sensitive) was used. Some theoretical studies [9, 14] proposed that strong phonon-mediated interactions between the two aforementioned bands are required to explain superconductivity and would lead to both bands being superconducting and have superconducting gaps slightly different in magnitude as observed in [13]. The analysis of Ref. [9] reports that the superconducting gaps and electron-phonon coupling on both bands yield a compelling evidence for the picture in which the π^*-IL interband interaction contributes less than 50% to the total electron-phonon strength to enable superconductivity.

We made an attempt to modulate the superconducting critical temperature of exfoliated CaC_6 crystals by electric field effect. These crystals are extremely sensitive to air and require a special procedure and environment for the device preparation. This technique consists in mounting the sample and fabricating the contacts in a completely inert atmosphere and hence we carried out the cleavage of the crystal and the patterning of contacts, as well as the drop casting and UV curing of the PES in a dry glove box.

An inert atmosphere of argon was created inside the glove box by repeated pumping and filling. Since the size of CaC_6 crystals is very small, approximately 1 mm × 0.5 mm and we are forced to stay in an inert atmosphere, we had absolutely no possibility to fabricate the contacts by standard lithographic techniques. For this reason it has been a challenging task to paint the current and voltage contacts with diluted silver glue by hand with high precision to make four wire measurements. After this operation the contacts and the edges of the crystal were sealed by liquid Kapton in order to give stability to the structure in the low temperature measurements. Most importantly, this is done to open the gating window

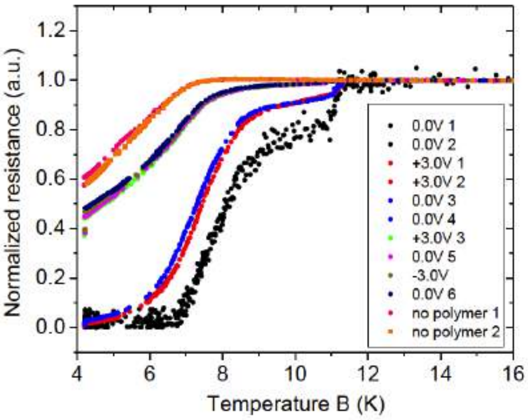

Figure 5.16. Normalized resistance vs. temperature for CaC_6 as measured under electrochemical gating

in the region between voltage contacts and prevent the contact of the PES with other regions of the sample and with the wires while measuring. Then PES was drop casted and UV cured under a lamp inside the glove box. The device was mounted on the sample holder of a cryogenic probe necessary, in order to perform transport measurements in a liquid helium dewar (Figure 5.15). The results of the measurements are shown in Figure 5.16 for normalized resistance as a function of temperature at several applied gate voltages. As it can be seen in the Figure 5.16 the superconducting transition was biphasic with the highest T_c (about 11.5 K) in agreement with the critical temperature of the bulk CaC_6. At the first application of a gate voltage of +3 V there was a clear shift of the lower T_c of about 0.5 K (red dots) that suggested a huge effect of the electrochemical gating. But, unfortunately the successive 0 V curve has shown the same features of the previous one (blue dots) suggesting that an effect of the gating is present but it is irreversible. After one day, with the sample always covered by the PES and the device kept in helium gas and so with no contact with air, the transition became broad and shifted to lower temperatures (green, magenta and dark blue dots). In this conditions the application of the gate doesn't change T_c anymore. Clearly the sample is progressively degraded and this is suspected to be partly due to the electric field effect through a permanent modification of the sample and partly to some degradation of the sample not related to applied voltage. It is remarkable that the degradation occurred while the sample was inside the helium dewar and, therefore, not in contact with atmospheric oxygen. A degradation produced by the small amount of oxygen accumulated into the PES during the short time it remained exposed to air seems rather unlikely. Thus the only reasonable explanation can be a degradation effect directly produced by the components of the PES and, in particular, lithium. Maybe a reaction of exchange between *Li* and *Ca* can remove *Ca* from the intercalation sites with a progressive degradation of the T_c of the sample.

The experiments are presently continuing and thus we have looked for a solution of these problems in the following two ways: first, in future, the device preparation will be carried out inside a glove bag of lower volume with continuous flush of argon or helium gas and second the composition of the PES with a *Li* salt will be changed to one with a *Ca* salt. The latter modification will allow us to verify if the use of an electrolyte that does not contain *Li* can overcome, at least partially, the big problem of the fast degradation of CaC_6 when covered by the PES.

Bibliography

[1] J. T. Ye, Y. J. Zhang, R. Akashi, M. S. Bahramy, R. Arita, and Y. Iwasa, *Science*, 338, 1193-6, 2012.

[2] J. T. Ye, Y. J. Zhang, R. Akashi, M. S. Bahramy, R. Arita, Y. Iwasa. Superconducting dome in a gate-Tuned band insulator. *Science*, 338, 1193-1196, 2012.

[3] G. Profeta, M. Calandra and F. Mauri, *Nature physics*, 8, 131, 2012.

[4] G. Profeta, M. Calandra and F. Mauri. Invited talk presentation at the conference Graphita.

[5] Article currently under preparation.

[6] A. C. Ferrari, J. C. Meyer, V. Scardaci, C. Casiraghi, M. Lazzeri, F. Mauri, S. Piscanec, D. Jiang, K. S. Novoselov, S. Roth. Raman Spectrum of Graphene and Graphene Layers. *Phys. Rev. Lett.*, 97, 187401, 2006.

[7] M. Bruna, A. K. Ott, Mari Ijäs, D. Yoon, U. Sassi and A. C. Ferrari. Doping dependence of the Raman spectrum of defected graphene. *ACS Nano*, 8, 7, 7432-7441, 2014.

[8] A. Ballestar, J. Barzola-Quiquia, S. Dusari, P. Esquinazi, R. R. da Silva and Y. Kopelevich. Electric Field induced Superconductivity in Multigraphene, arXiv:1202.3327v1 [cond-mat.supr-con], 2012.

[9] S.-L. Yang, J.A. Sobota, C.A. Howard, C.J. Pickard, M. Hashimoto, D.H. Lu, S.-K. Mo, P.S. Kirchmann and Z.-X. Shen. Superconducting graphene sheets in CaC_6 enabled by phonon-mediated interband interactions. *Nat. Commun*, 5:3493, doi: 10.1038/ncomms4493, 2014.

[10] Thomas E. Weller, Mark Ellerby, Siddharth S. Saxena, Robert P. Smith and Neal T. Skipper, Superconductivity in the intercalated graphite compounds C_6Yb and C_6Ca, *Nature Physics* 1, 39 - 41, 2005.

[11] N. Emery, C. Hérold, M. d'Astuto, V. Garcia, Ch. Bellin, J. F. Marêché, P. Lagrange, and G. Loupias, Superconductivity of Bulk CaC_6, *Phys. Rev. Lett.*, 95, 087003, 2005.

[12] J. S. Kim, L. Boeri, J. R. O'Brien, F. S. Razavi, and R. K. Kremer, Superconductivity in Heavy Alkaline-Earth Intercalated Graphites, *Phys. Rev. Lett.*, 99, 027001, 2007.

[13] R. S. Gonnelli, D. Daghero, D. Delaude, M. Tortello, G. A. Ummarino, V. A. Stepanov, J. S. Kim, R. K. Kremer, A. Sanna, G. Profeta, and S. Massidda, Evidence for Gap Anisotropy in CaC_6 from Directional Point-Contact Spectroscopy, *Phys. Rev. Lett.*, 100, 207004, 2008.

[14] Matteo Calandra and Francesco Mauri, Theoretical Explanation of Superconductivity in C_6Ca, *Phys. Rev. Lett.*, 95, 237002, 2005.

[15] A. Pachoud, M. Jaiswal, P.K. Ang, K. P. Loh and B. Ozyilmaz, *Europhysics Lett.*, 92, 27001, 2010.

[16] N. Garcia, P. Esquinazi, J. Barzola-Quiquia and S. Dusari, Evidence for semiconducting behavior with a narrow band gap of Bernal graphite, *New Journal of Physics*, 14, 053015, 2012.

[17] Barzola-Quiquia J., Yao J-L., Rodiger P., Schindler K and Esquinazi P., Sample size effects on the transport properties of mesoscopic graphite samples, *Phys. Status Solidi A*, 205, 2924-33, 2008.

Chapter 6

Conclusions and Future Perspectives

Growing interest in solid-liquid interfaces is justified due to their fascinating applications. For example, recently, the approach is to enhance charge transport in materials by applying very large electric fields using polymer electrolyte solutions (PES) or ionic liquids (ILs) as the gate dielectric. PES or ILs, an exciting new class of materials, occupy the frontier of several fields such as high electric field gated electronics, energy storage, and electrochemistry. In some device applications, PES and ILs supply extraordinarily high electric fields, which can engender entirely new materials transformations. We explored the basic interactions that occurred at PES-solid interfaces and determine the static and dynamic response of solids and polymers under an applied voltage. We developed an understanding to design PES-solid material combinations, applied these to generate high E-fields that enable the discovery of novel phenomena, and explored new device concepts for a range of applications. In the recent years this versatile technique has been applied to many materials to deepen understanding of fundamental properties. Exemplary materials where superconducting phase transition has been successfully accessed by this technique are molybdenum-di-sulfide (MoS_2) and strontium titanate ($SrTiO_3$). With this thesis we conclude our studies of electrochemical gating technique and its consequences on a variety of low dimensional materials like few and single layers of graphene, highly oriented pyrolytic graphite and CaC_6. Strong modification of transport properties of these low dimensional materials was carried out by tuning their surface charge carrier densities (up to values of induced charge exceeding 6×10^{14} carriers cm^{-2}). The induced surface charge was measured by a suitable modification of a classic method of electrochemistry called the double-step chronocoulometry. Since the application of this technique is quite new for this purpose, we made a validation check by comparing it with the standard Hall effect measurements. Along with the successful comparison we were able to deeply study the complexity involved in the procedure of this technique. We analyzed the advantages and drawbacks of this technique in details by application on various mentioned materials. We performed the cyclic voltammetry tests and electrochemical impedance spectroscopy analysis in order to understand and distinguish between the effects of electric field influence and chemical doping. This led us to broaden our knowledge on the amount of electrochemical stability window and limits of operation. The main results of the mentioned work led to the conclusion that electrochemical gating is a much more efficient way as compared to the standard dielectric gating. In all the field effect devices we were able to perform standard four-wire transport measurements down to 3.5 K. However, even at the highest induced charge density no trace of superconducting transition have been observed, but the temperature dependence of the resistance showed a crossover from a low-T regime dominated by electron-electron scattering and a regime at higher T ($\geq$ 100 K) where only the standard high temperature electron-phonon scattering exists. The crossover temperature can be associated to the Bloch-Grüneisen temperature of the material, but it does not show any dependence on the Fermi energy, pointing to important differences in the electric transport properties of FLGs and SLG at the large charge densities induced by PES gating. Further, a continuous enhancement (or progressive induction) of the metallic behavior and a low-temperature logarithmic upturn of the resistance, strongly dependent on the induced charge has been observed. Since Kondo-effect and electron-electron interaction contributions have been ruled out on the basis of Raman measurements and of the magnetic-field dependence of the resistance, this peculiar low-temperature behavior has been analyzed and explained in terms of weak localization (WL) due to localized defects at the sample surface. In this respect ab-initio theoretical calculations of the electron and phonon properties of these materials in presence of a huge induced charge density have been performed that provide direct information on these properties. Along with these we tried to accumulate Li^+ over the surface of SLG with an attempt to freeze the system and observe superconductivity by application of the electric field effect and doping method simultaneously. On the other hand, HOPG was monitored under electrochemical gating for the first time and checked for its diverse properties on high charge induction. And also an attempt was made to modulate the superconducting critical temperature of CaC_6 by the electrochemical gating technique.

Future perspectives comprises of mainly to carry out previously aimed experiments with CVD-grown SLG in temperature to observe the possibility to induce superconductivity in the presence of accumulated Li^+ at the highest amount of charge density. As we have reported these experiments have not been successful up to now due to the bulkiness of the device system. An intelligent improvement designed for the future is to use a different composition of the polymer electrolyte solution and/or instead use ionic liquids. Also, we could study the electric field effect on highly oriented pyrolytic graphite by a better control of number of layers. As we have seen, HOPG with different thickness leads to different behavior in resistance, hence, it is very important to carefully check the exact thickness to characterize its properties. Also finish ongoing experiments on CaC_6 to study the effect of electrochemical gating in order to modulate its superconducting critical temperature and apply polymer gating technique on novel materials like black phosphorous and transition metal dichalcogenides like $MoSe_2$, MoS_2 and $NbSe_2$.